Novel photo-detector architectures for high-energy radiation imaging applications

by

Sahar Adnani

A thesis
presented to the University of Waterloo
in fulfillment of the
thesis requirement for the degree of
Doctor of Philosophy
in
Electrical and Computer Engineering

Waterloo, Ontario, Canada, 2023

© Sahar Adnani 2023

Examining Committee Membership

The following served on the Examining Committee for this thesis. The decision of the Examining Committee is by majority vote.

External Examiner:	Safa Kasap Distinguished Professor, Dept. of Electrical and Computer Engineering, University of Saskatchewan
Supervisor(s):	Karim S. Karim Professor, Dept. of Electrical and Computer Engineering, University of Waterloo
Internal Member:	Hany Aziz Professor, Dept. of Electrical and Computer Engineering, University of Waterloo
Internal Member:	Mahla Poudineh Assistant Professor , Dept. of Electrical and Computer Engineering, University of Waterloo
Internal-External Member:	Vassili Karanassios Professor, Dept. of Chemistry, University of Waterloo

Author's Declaration

I hereby declare that I am the sole author of this thesis. This is a true copy of the thesis, including any required final revisions, as accepted by my examiners.

I understand that my thesis may be made electronically available to the public.

Abstract

This work is an investigation of amorphous Selenium (a-Se) based semiconductor detectors for high-energy radiation imaging applications. The work focuses on enhancing the detection efficiency of a-Se while maintaining spatial resolution and linearity. Additionally, various detector configurations are explored along with materials for reduced dark current and the implementation of novel readout methods.

Simulation results demonstrate that stacking a-Se based detectors with a pixel size of 1 mm can significantly enhance detection efficiency without substantial degradation of spatial resolution for detection of single photon emission computing tomography (SPECT) gamma radiation. A careful balance between energy thresholds and the number of layers reveals that 52% detection efficiency is achievable for a 110 keV energy threshold using 10 detector layers. This approach effectively reduces noise counts arising from interlayer scattering. In addition, a $50\mu m$ pixel pitch detector exhibited lower detection efficiency for high energy thresholds, hence requiring more detector layers to be comparable to the 1 mm pixel detector. The findings indicate that proper design of a-Se stacked detectors can offer a cost-effective solution for large-area radiation imaging applications with the potential to achieve sub-millimeter resolution.

A resistive microstrip detector design coupled with charge division readout is introduced to overcome the complexity of stacking multiple a-Se detector layers in practice. The experimental results verified 1 mm spatial resolution with high linearity over the microstrip length. The proposed bottom microstrip design, along with demonstration of this design on a flexible substrate not only simplifies readout circuit complexity but also facilitates the realization of curved multi-layer detectors for high-energy radiation imaging applications.

To address dark current issues associated with the novel detector design, this work explores the utilization of low-temperature SU-8 as a hole-blocking layer for a-Se detectors. Results showcase the viability of achieving dark currents below 1 pA/mm^2 even at increased electric fields of 40 $V/\mu m$. The adoption of the bilayer configuration, incorporating both SU-8 and Cs-doped a-Se, further enhances sensitivity and minimizes lag. This advancement holds promise for the development of high-performance selenium radiation detectors suitable for dynamic medical imaging.

The new detector design with resistive microstrips and the new hole-blocking bilayer was employed in a photon counting setup. Challenges related to noise are addressed through the incorporation of the commercially available CUBE charge preamplifier and the design of a custom PCB board. The successful capture of photons and the generation of Pulse Height Spectra (PHS) validate the effectiveness of the novel approach, opening the door for further work on charge division and multi-channel PHS results.

Overall, this work contributes to the utilization of a-Se semiconductor material for new radiation imaging applications and especially, for realizing high-energy radiation imaging applications that have not been traditionally associated with lower atomic number (Z=34) a-Se photoconductor. The proposed advancements include a comprehensive range of innovations, including higher detection efficiency, reduction in dark current at high voltages, noise mitigation, and a simplified large-area image readout scheme that can expedite the commercial development of a-Se detectors for new higher radiation energy medical, industrial and scientific imaging applications.

Acknowledgements

I am deeply grateful to Dr. Karim S. Karim for his unwavering guidance, encouragement, and trust that have facilitated the exploration of ideas throughout my academic journey. Dr. Karim's invaluable role as a supervisor has played a crucial part in my achievements during my Ph.D., and I am honored to have had the privilege of learning and growing under his guidance.

I extend my gratitude to Dr. Vassili Karanassios for his support and for granting me the opportunity to carry out experiments in his laboratory.

I would like to express appreciation to my committee members, Dr. Hany Aziz, Dr. Vassili Karanassios, and Dr. Mahla Poudineh, for accepting to review my work.

I would like to express my gratitude to my colleagues. First, I am thankful to Abdollah Pil-Ali for his invaluable support and contribution in both fabrication and idea generation. Additionally, I appreciate Celal Con for his contributions to fabrication and insightful suggestions, Zain Warsi and Reza Mohammadi for their help on the circuit side, and I extend my thanks to Steve Germann for accepting to proofread my thesis.

I would also like to express my thanks to all the members of the Silicon Thin-Film Applied Research (STAR) group, past and present, for their friendship and guidance. In particular, I would like to acknowledge Chris Scott and Ahmet Camlica for their friendship and advice.

I am especially thankful to Richard Barber for his exceptional support, including providing access to facilities after hours and aiding in instrument maintenance. I am also thankful to Dr. Czang-Ho Lee for training me in the G2N lab.

I express my appreciation to my friends and dear ones for the cherished memories we created throughout my journey and the wonderful moments we shared.

Lastly, and of utmost significance, I extend my gratitude to my parents for their unwavering love, support, and patience during these years.

Dedication

This is dedicated to my family and friends.

Table of Contents

List of Figures xii

List of Tables xvii

List of Abbreviations xviii

1 Introduction 1

1.1 Motivation . . . 1

1.2 Objectives . . . 2

1.3 Thesis Organization . . . 3

2 Radiation detectors 4

2.1 Introduction . . . 4

2.2 Photon/Matter interaction . . . 5

2.2.1 Photoelectric effect . . . 5

2.2.2 Compton scattering . . . 6

2.2.3 Pair production . . . 6

2.3 Detection mechanism . . . 7

2.3.1 Scintillation . . . 7

2.3.2 PMT tube . . . 8

2.3.3 Semiconductors . . . 9

2.4 Frisch grid . . . 10
2.5 a-Se large-area photoconductor . . . 13
2.5.1 Band structure . . . 15
2.5.2 DOS of a-Se . . . 17
2.6 Readout modes . . . 19
2.6.1 Energy integrating mode . . . 19
2.6.2 Photon counting mode . . . 20
2.7 Characteristics of the detector . . . 21
2.7.1 Sensitivity . . . 21
2.7.2 Dark current . . . 23
2.7.3 Temporal response . . . 23

3 Multilayer Detectors for High-Energy Imaging 25
3.1 Introduction . . . 25
3.2 Proposed design . . . 27
3.3 Monte Carlo simulation . . . 29
3.4 Simulation results . . . 32
3.5 Conclusion . . . 39

4 Charge division readout for large area radiation imaging 40
4.1 Introduction . . . 40
4.2 Experimental method . . . 43
4.3 Microstrip fabrication . . . 45
4.4 Top microstrip design . . . 46
4.4.1 Results . . . 49
4.5 Bottom microstrip design . . . 50
4.5.1 Results . . . 53
4.6 Conclusion . . . 54

5 Optimization of Hole Blocking Layer **55**
5.1 Introduction . . . 55
5.2 Experimental Methods . . . 57
5.3 SU-8 hole-blocking layer . . . 59
5.3.1 Results . . . 59
5.4 Novel hole-blocking bilayer . . . 66
5.4.1 Results . . . 66
5.5 Time of flight measurement . . . 72
5.6 Application to dynamic imaging . . . 79
5.7 Conclusion . . . 83

6 Photon counting performance **84**
6.1 Introduction . . . 84
6.2 Single pixel design . . . 84
6.2.1 CoolFet experimental setup . . . 85
6.2.2 Results . . . 87
6.3 Microstrip design . . . 89
6.3.1 CUBE experimental setup . . . 89
6.3.2 Results . . . 92
6.4 Conclusion . . . 97

7 Potential methods for improving temporal resolution **98**
7.1 Crystalline selenium . . . 99
7.1.1 Setup . . . 100
7.1.2 Results . . . 101
7.2 Selenium-Based Drift Detector . . . 107
7.2.1 Materials and Methods . . . 108
7.2.2 Simulation results . . . 112
7.3 Conclusion . . . 118

8 Conclusion and Future Work **120**

8.1 Conclusion 120

8.2 Contributions 121

8.3 Future work 122

8.4 Publications 123

References **126**

List of Figures

2.1 Linear attenuation coefficient in different energies for water which resembles the body tissue [1]. 5

2.2 SiPM equivalent circuit 10

2.3 (a) Coplanar structure, (b) Frisch grid structure. 11

2.4 Weighting potential and induced current (a) Conventional, (b) Hypothetical single polarity sensing detector. 12

2.5 Weighting potential for a realistic single polarity sensing detector. 13

2.6 Evolution of band structure for amorphous semiconductors showing band structures for (a) the crystalline materials (b) the initial model for amorphous semiconductors proposed by Mott, (c) the CFO model, (d) and Marshall and Owen model [2]. 16

2.7 Replotted DOS of a-Se from Kasap [3], which combines data from different studies indicated by various line colors, styles, and shades [4, 5, 6, 7, 8, 9, 10]: (a) DOS near the valence band edge and mid-gap (related to hole traps), (b) DOS near the conduction band edge and mid-gap (related to electron traps) 18

2.8 Attenuation coefficient for different materials generated from [11]. 22

2.9 The appearance of lag and ghosting after an exposure over a mask. 24

3.1 3D design of the detector holder with three detectors stacked on top of each other. 28

3.2 Illustration of the structure of a single detector layer featuring sublayers. . 28

3.4 A photon undergoing Compton scattering. 32

3.3 PHS and PSF histograms. PSF is computed for energy bins shown in PHS and colors represent probability values $\in [0, 1]$ in logarithmic scale: (a) 1 mm pixel pitch, (b) 50 μm pixel pitch. 33

3.5 MTF for the number of layers from 1 to 10. (a) 1 mm pixel pitch. (b) 50 μm pixel pitch 34

3.6 MTF for different energy thresholds in 3 detector layers. (a) 1 mm pixel pitch, (b) 50μm pixel pitch. 35

3.7 Detection efficiency. (a). For the number of layers from 1 to 10. (b) For different threshold energies 36

3.8 MTF for three layers with the gap between layers from 1μm to 2 mm. (a) 1 mm pixel pitch. (b) 50 μm pixel pitch 37

3.9 Detection efficiency for three layers with the gap between layers from 1μm to 2 mm. 38

3.10 DQE(0), uncorrected DE, and corrected DE for the detector thickness of 0.1 mm and number of layers from 3 to 200. Uncorrected DE exceeds 100% due to the occurrence of multiple counts recorded for a single photon. For additional details, please refer to section 3.3. 38

4.1 fabricated device with wires attached to bonding pads using silver paste. . 42

4.2 Experiment setup (a) model (b) assembeled on motorized stages. 44

4.3 Shadow mask for top microstrip design. 46

4.4 Illustration of (a) side view of the detector structure, (b) top view of detector structure showing both ends of restive electrodes 48

4.5 fabricated device with wires attached to bonding pads using silver paste. . 48

4.6 (a) The photocurrents read from the two ends of a single electrode after dark current correction versus the position of the light source. (b) Detected position from the charge division equation along the electrode versus the actual position of the light source. 49

4.7 Illustration of the (a) side (b) top view of the detector structure. 50

4.8 Shadow mask for bottom microstrip design. 51

4.9 Fabricated device on (a) glass (b) PET substrate. 52

4.10 (a) The photocurrents read from the two ends of a single electrode after dark current correction versus the position of the light source. (b) Detected position from the charge division equation along the electrode versus the physical location of the light source. 53

5.1 Dark current density of the a-Se detectors including reference device and those integrating PI and SU-8 hole-blocking layers as a function of electric fields. The reported values are the mean of the plateau achieved after maintaining a constant electric field for 20 minutes. 60

5.2 Photoresponse of a-Se detectors with PI and SU-8 hole-blocking layers to a blue LED with intensity of 110 $\mu W/cm^2$. 61

5.3 a-Se sample with SU-8 hole-blocking layer at the top exposed to pulsed X-ray to measure sensitivity and lag. 62

5.4 X-ray response of a-Se detectors with PI and SU-8 hole-blocking layers to first and last exposure with measured values shown on the right. 63

5.5 (a) Sensitivity and (b) lag of a-Se detectors featuring PI and SU-8 hole-blocking layers biased at 20V/μm for 20 exposures, each with a dose of 8.76 mGy and intervals of 60 seconds. The positive electrode is indicated as "(+)". 65

5.6 Dark current density of the a-Se detectors including those incorporating hole-blocking bilayer and single-layer configurations as a function of electric fields. The reported values are the mean of the plateau achieved after maintaining a constant electric field for 20 minutes. 67

5.7 Photoresponse of a-Se detectors biased at $20V/\mu m$ to a blue LED with intensity of 110 $\mu W/cm^2$. 68

5.8 Photoresponse of a-Se detectors biased at $30V/\mu m$. 69

5.9 (a) Sensitivity and (b) lag of a-Se detectors including the hole-blocking bilayer, biased at 20V/μm for 20 exposures (8.76 mGy each) with 60-second intervals. The positive electrode indicated as "(+)". 71

5.10 Time of flight experimental setup. 72

5.11 Behaviour of the detector utilizing hole-blocking bilayer at the bottom of the detector which is biased at 150 V ($\approx 7V/\mu m$) when exposed to a short laser pulse, with fitted lines utilized to approximate the transit time. . . . 74

5.12 (a) Transit time divided by thickness plotted against the electric field, without accounting for the voltage drop across the hole-blocking layer. (b) Mobility is calculated based on the data derived from the graph in (a) 76
5.13 (a) Transit time divided by thickness plotted against the true electric field across selenium layer including the doped selenium (b) Mobility calculated based on the data derived from the graph in (a). 78
5.14 The response of the detector with hole-blocking bilayer configuration biased at $10V/\mu m$ in fluoroscopy mode operating at a frame rate of 30 frames per second. 80
5.15 The response of the detector with PI hole-blocking layer biased at $10V/\mu m$ in fluoroscopy mode operating at a frame rate of 30 frames per second. . . 81
5.16 a) The response of the detector with hole-blocking bilayer configuration biased at $20V/\mu m$ in fluoroscopy mode operating at a frame rate of 30 frames per second. b) Enlarged view of the detector's response. 82

6.1 (a) Pulse-height spectroscopy experimental setup, (b) detector box including the detector and the CoolFET preamplifier. 86
6.2 Pulse height spectra of a conventional a-Se detector in response to (a) ^{241}Am gamma source, (b) ^{57}Co gamma source. 88
6.3 PHS setup utilizing CUBE preamplifier along with its bias board, collimator, and motorized stage 90
6.4 CUBE carrier board inside the detector box with a close-up view of CUBE bonding 91
6.5 Signals from two ends of a single microstrip for the setup without any detector attached and showing the FFT of the signal, an indication of noise level. 92
6.6 (a) Signals from two ends of a single microstrip for the setup with detector biased at $10V/\mu m$ without any gamma source (b) zoomed-in on the reset section of the signal and showing the FFT of the signal. 94
6.7 Capture of single photon using ^{241}Am source and CUBE setup. The green signal shows the output of one of the CUBEs and the blue signal is the output of shaping-amplifier. 95
6.8 PHS results for (a) no ^{241}Am gamma source present to demonstrate the background noise (b) ^{241}Am gamma source is present and (C) the corrected data with the ^{241}Am gamma source present. 96

7.1 DSC curve of a-Se core [12]. 99
7.2 Crystallization setup used in thermal annealing 100
7.3 A. x250 zoom 102
7.4 Raman spectroscopy for a-Se film before and after annealing 103
7.5 SEM image of c-Se showing the islands of crystallization 104
7.6 a-Se samples with Te interlayer (a) before annealing and (b) after annealing. 105
7.7 12 μm c-Se samples on a flexible PET substrate 105
7.8 Dark current for two c-Se detectors one without hole blocking layer and one with 0.5μm Parylene c 106
7.9 Illustration of (a) side view of a conventional micro strip detector with planar top contact, (b) Electric field magnitude along the detector width in the middle of a-Se and perpendicular to the direction of strips. 109
7.10 3D view of the proposed structure for a-Se drift detector utilizing resistive collecting electrodes and dual end readout. 110
7.11 Side view of a-Se drift detector with high voltage planar top electrode . . . 111
7.12 Electric field and potential for a cross section of the drift detector with planar top contact. 113
7.13 Electric field and potential for a cross section of the drift detector with parallel microstrips on both sides. 114
7.14 Electric field magnitude and direction inside the detector with top contact voltage of 700V. 115
7.15 Electric field magnitude along the detector width in the middle of a-Se and perpendicular to the direction of strips for different values of top contacts . 116
7.16 Electric field streamline for (a) V_B = 400 V (b) V_B = 1200 V. 117
7.17 Illustration of weighting potential across the drift detector with collecting electrodes biased at 1V and other electrodes at zero. 118

List of Tables

3.1 Geant4 Geometry Parameters 29

7.1 COMSOL Model - Geometry Parameters 112

List of Abbreviations

a-Se amorphous selenium

Al aluminum

AO atomic orbitals

APD avalanche photodiode

APS active pixel sensor

As arsenic

ASDD a-Se drift detector

c-Se crystalline selenium

Cl chlorine

CMOS complementary metal-oxide-semiconductor

Cr chromium

CT computed tomography

CZT cadmium zinc telluride

DOS density of states

DSC differential scanning calorimetry

EHP electron hole pair

FWHM full-width at half-maximum

HBL hole-blocking layer

IFTOF Interrupted-Field Time-of-Flight

ITO indium tin oxide

LSF line spread function

MCA multichannel analyzer

MO molecular orbitals

MTF modulation transfer function

NSB normal structure bonding

PCB printed circuit board

PCD photon counting detector

PET polyethylene terephthalate

PHS pulse height spectra

PI polyimide

PMT photomultiplier tube

PPC persistent photoconductivity

PPS passive pixel sensor

PSD position-sensitive detector

PSF point spread function

SDD silicon drift detector

SiPM silicon photomultiplier

SNR signal-to-noise ratio

SPAD single-photon avalanche diode

SPECT single photon emission computed tomography

TOF time of flight

Chapter 1

Introduction

1.1 Motivation

Medical imaging technology has undergone a significant transformation with the advent of digital imaging. These advancements have played a crucial role in reshaping the healthcare sector, leading to early detection through improved diagnostics and consequently, enhanced patient care. Nuclear imaging depends on detecting and tracking emissions from radioactive substances, called radiotracers, inside the human body. This method, known as functional imaging, reveals how active cells are in specific body areas where radiotracers accumulate. Nuclear imaging can help with diagnosis and treatment planning and a notable example is single photon emission computed tomography (SPECT), which relies on radiotracers emitting specific gamma rays in the energy range of 140 keV-160 keV when they decay. Conventional SPECT detectors, utilize optical photons generated by scintillators such as NaI(Tl) crystals and convert them to electric signals using photomultiplier tube (PMT). This configuration has limited spatial resolution and is susceptible to magnetic field interference.

To overcome these limitations, a promising path involves the adoption of direct conversion materials, like cadmium zinc telluride (CZT), which converts gamma-ray photons directly into electron-hole pairs. This direct conversion process enhances spatial resolution and compactness, while simultaneously reducing vulnerability to magnetic field interference. Nonetheless, challenges tied to CZT fabrication, including cost and inconsistent yield, present substantial barriers to realizing large-area detectors with CZT. An alternative method utilizes amorphous selenium (a-Se), a mature and cost-effective direct conversion semiconductor already well-established in lower energy X-ray imaging, especially in

mammography. The prominence of a-Se in this context stems from its exceptional spatial resolution. Although a-Se is currently constrained by its low stopping power (Z=34), its capacity to address challenges hampering CZT and its demonstrated large-area manufacturing base are highly promising.

Moreover, the significance of medical imaging has grown substantially alongside the increasing prevalence of cancer. Early detection, a pivotal phase in the battle against cancer, heavily relies on accessible medical imaging tools. To create more cost-effective medical imaging devices, the components of detectors must be straightforward to manufacture. The primary characteristic that defines a detector's cost-effectiveness for practical usage is its capacity to be produced on a large area while retaining crucial traits such as high spatial and temporal resolution. In the domain of nuclear imaging, detectors constructed using a-Se (amorphous Selenium) hold immense potential for practical deployment. However, certain challenges remain, particularly concerning the limited energy absorption spanning over 140 keV to 160 keV energy spectrum, and the requirement for improved temporal resolution. This becomes especially important in the growing field of dynamic mammography tomosynthesis, an innovative quasi-3D technique that has been reported to surpass traditional 2D mammography in detecting breast cancer.

1.2 Objectives

Our objective is to develop a-Se technology to make it suitable for high-energy radiation imaging applications. There are two challenges associated with using a-Se: low stopping power (i.e. low detection efficiency) and low temporal resolution. The primary focus of this thesis is to thoroughly address the first challenge and assess the viability of our novel idea:

- Stacking the detectors to improve the detection efficiency and address its complications by
  - simplifying the readout using charge division readout
  - reducing dark current with a low-temperature hole-blocking bilayer

To address the second challenge and improve temporal performance, two potential methods are proposed albeit with preliminary results:

- Converting a-Se to crystalline selenium (c-Se) to increase the charge carrier mobility.

- Simulating an a-Se drift detector to shape the field, aiming to achieve unipolar charge sensing.

1.3 Thesis Organization

The primary focus of this thesis is the development of a-Se detector for high-energy applications with improved detection efficiency and temporal performance. The thesis chapters are organized as follows:

- Chapter 2 provides foundational knowledge on radiation detection, covering photon/matter interaction, charge collection, and the introduction of a-Se as the photoconductor explaining its properties. Essential figures of merit for radiation detectors, including sensitivity, dark current, and memory effects, are also introduced.
- Chapter 3 presents the innovative concept of multilayer a-Se detectors and employs Monte Carlo simulations to illustrate the impact of layer count on metrics such as modulation transfer function (MTF) and detection efficiency.
- Chapter 4 introduces a novel strategy involving charge division readout to simplify the complex readout process in multilayer detectors. A prototype a-Se detector is fabricated, incorporating resistive microstrips, demonstrating spatial resolution for charge division readout using an LED source.
- Chapter 5 investigates the incorporation of a low-temperature organic hole-blocking layer on the top surface of a-Se and introduces an innovative bilayer configuration designed to enhance sensitivity and reduce lag.
- Chapter 6, investigates a photon counting setup to obtain pulse height spectra (PHS). This includes both the conventional a-Se detector and the novel design, which combines resistive microstrip readout with the new hole-blocking bilayer configuration, demonstrating successful photon detection.
- Chapter 7 outlines two potential solutions for enhancing the temporal performance of a-Se. One method involves replacing the photoconductor with its crystalline phase (c-Se). The second method proposes a drift detector based on a-Se, combined with the resistive microstrip concept.
- Chapter 8 offers a comprehensive overview of the thesis, coupled with an exploration of prospective paths for further investigation and potential research domains.

Chapter 2

Radiation detectors

2.1 Introduction

Gamma and X-ray detectors play a vital role in ionizing radiation detection and measurement. They are specifically designed to interact with high-energy photons and effectively convert them into measurable electrical signals. These detectors are of utmost importance in medical imaging applications. In this chapter, we explore the fundamental aspects of gamma/X-ray detectors, including the interactions between photons and matter, and the mechanisms that allow these detectors to effectively convert radiation into electrical signals. Afterward, we focus on the utilization of amorphous selenium (a-Se) as a photoconductor, discussing its unique properties and advantages in gamma and X-ray detection. Understanding the role of a-Se in the detection process will shed light on the overall performance and capabilities of this photoconductor.

Additionally, we explore the functioning of pixel readout circuits, which are integral components of gamma and X-ray detectors. These pixel circuits are responsible for amplifying and/or processing the electrical signals generated by the detectors, enabling accurate measurement and analysis. Understanding the functionality of these circuits will provide insights into the overall performance and sensitivity of the detectors. Lastly, we examine the distinguishing characteristics of radiation detectors. Each detector possesses unique features that make it suitable for specific applications and environments. By exploring these characteristics, we can gain a deeper understanding of the advantages and limitations of different types of detectors.

2.2 Photon/Matter interaction

When photons encounter matter, they engage in three distinct interaction processes: photoelectric effect, Compton scattering, and pair production [1]. Each of these processes is characterized by an attenuation coefficient that quantifies the reduction in photon intensity. The total linear attenuation coefficient (μ_l) experienced by a photon passing through matter is the summation of these individual coefficients:

$$\mu_l \;=\; \tau + \sigma + \kappa \tag{2.1}$$

Here, τ is the photoelectric coefficient, σ is the Compton coefficient, and κ is the pair production coefficient. The dominance of these coefficients in different energy regions is shown in Fig. 2.1, which illustrates the relationship between the attenuation coefficients and photon energy in water.

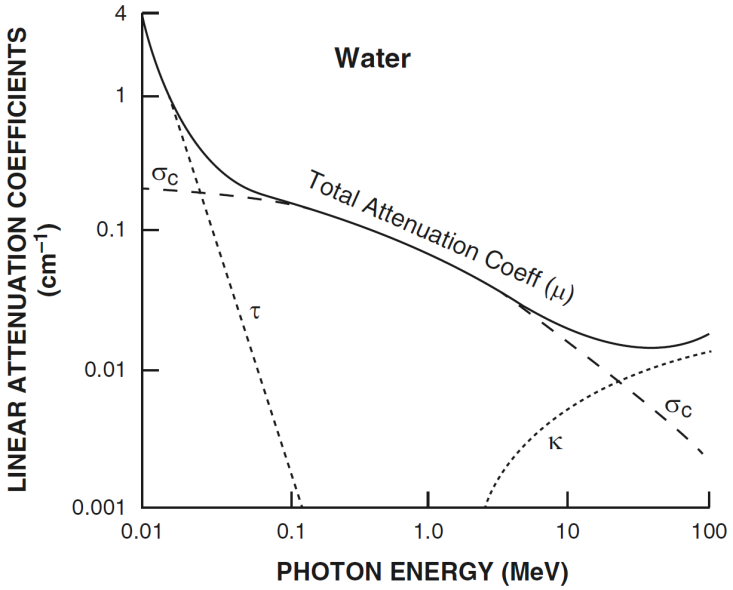


Figure 2.1: Linear attenuation coefficient in different energies for water which resembles the body tissue [1].

2.2.1 Photoelectric effect

When photons possess low energies or have undergone significant energy loss through scattering, yet their energy remains higher than the binding energy of an electron, they

transfer all their remaining energy to the electron, predominantly from an inner shell, resulting in electron ejection. The kinetic energy of the photoelectric electron is equal to the difference between the incident photon energy (E_γ) and the binding energy (E_b) of the electron. The vacancy left by the ejected electron in the inner shell is subsequently filled by an electron from an outer shell, accompanied by the emission of characteristic X-rays. Alternatively, the energy difference can be transferred to another electron, leading to its ejection, a phenomenon known as the Auger effect, with the ejected electron referred to as an Auger electron.

The photoelectric effect depends on the atomic number of the material and the energy of the incident photon. An increase in atomic number and a decrease in photon energy enhance the probability of the photoelectric effect. In the context of low-energy X-rays, the photoelectric effect represents the primary absorption mechanism.

2.2.2 Compton scattering

Photons with high energy levels interact with matter through scattering phenomena, manifesting as elastic and inelastic scattering processes. In the context of elastic scattering, also known as Rayleigh scattering, photons engage with tightly bound electrons, resulting in a negligible alteration of their trajectory without substantial energy exchange. Conversely, in the realm of inelastic scattering, photons interact with weakly bonded electrons, leading to electron ejection and the subsequent deflection of the scattered photon by angles up to 180 degrees. This particular scattering mechanism is referred to as Compton scattering, with the ejected electron being designated as a Compton electron.

During Compton scattering events, the scattered photon experiences energy depletion, potentially undergoing subsequent scatterings or triggering the photoelectric effect. Notably, the incidence of Compton scattering is independent of the atomic number of the material and exhibits an enhanced likelihood with increasing incident photon energy. However, it is important to note that although the probability of Compton scattering diminishes as photon energies exceed 1.022 MeV, for gamma-ray photons above 100 keV, Compton scattering remains the predominant mechanism.

2.2.3 Pair production

Photons with energy exceeding 1.022 MeV exhibit interactions with the nucleus of a material, causing a conversion of their energy into mass through the emission of an electron and a positron. The excess energy resulting from this interaction is divided as kinetic energy

between the two particles. The positron, in particular, can subsequently undergo a process known as annihilation. As the positron loses its kinetic energy, it becomes unable to resist the attractive force exerted by electrons due to their opposite charges. Consequently, the positron and an electron annihilate in accordance with Einstein's mass-energy equation, giving rise to the production of two gamma-ray photons.

2.3 Detection mechanism

The principle for detection of ionizing radiation is based on its interaction with matter. In this way charged particles generated in matter (either electrons or ions) are collected as current or count by applying voltage across the material. In low voltage regime, the collected current is proportional to the amount of energy that interacted with matter. However, in a very high voltage regime, the current is independent of the radiation energy, because the avalanche process multiplies the number of carriers and acts as a gain [13]. In conventional gamma detectors, first, the γ-ray photons are converted to optical photons in the scintillator layer, then photomultiplier tubes are used to get higher gain and convert the optical photons to electrons and collect them as an electric pulse. Another linear amplifier is used to amplify the signal even more and it goes through a pulse height analyzer and then is considered as a count.

2.3.1 Scintillation

Generally, scintillators can be liquid, gas, or solid. Detection efficiency is low in liquid and gas forms which are therefore unsuitable for medical applications, so solid detectors are the main focus here. To choose a good scintillator, there are several criteria that should be considered.

- Stopping power

  This is the mean distance that the photon travels in the scintillator to fully lose its energy. Materials with higher atomic number and density have greater power to stop the photon, hence the required thickness is much lower.

- Decay time

  When a γ-ray interacts with the scintillator, atoms get excited, and after a certain time decay back to a lower state along with the emission of optical photons. This

certain time is called the decay time. A shorter decay time is desirable, to allow higher count rates.

- Light output

  As mentioned before, during the decay of excited atoms, photons are emitted. The number of photons emitted per 1 keV absorbed energy is the specific light output. Depending on the material, it can be 2 to 60 photons per 1 keV [14]. Energy resolution increases with the increase of light output.

- Energy resolution

  When the detected energies of a monoenergetic photon stream are plotted in a distribution, the energy resolution is the ratio of the full-width at half-maximum (FWHM) to the energy value at the peak. The lower value is desirable to have a clean peak at the desired keV. The intrinsic energy resolution is related to the crystal structure of the scintillator and statistical variation of light output.

One of the most familiar scintillators for nuclear imaging is NaI, which has a good light output and energy resolution. It should be noted that scintillator detectors are subject to the light spreading within the scintillator. Due to the isotropic nature of the emitted light within the scintillator, an equal number of photons are emitted in all directions. However, this causes light generated above one pixel to spill over and impact adjacent pixels, leading to reduced spatial resolution. To address this issue, specialized needle-like structures, such as those used in CsI scintillators, are fabricated. These structures effectively confine the emitted light, limiting its lateral spread and thereby improving the spatial resolution of the scintillation light [15].

2.3.2 PMT tube

The photomultiplier tube (PMT) is a glass tube with a vacuum inside, comprising a photocathode at one end, several dynodes, and an anode at the other end. The voltage difference between the cathode and anode is approximately 1000 V, with incremental steps of 100 V at each dynode. Photons produced from the scintillator strike the photo-cathode, typically made of an alloy of cesium and antimony, causing electrons to be ejected and accelerated towards the first dynode. At each dynode, each electron generates multiple electrons, which then continue to the next dynode. Through this process, the electrons are multiplied and eventually pass through the anode for collection.

2.3.3 Semiconductors

Semiconductors are low-Z materials, resulting in weak stopping power for incident photons. When a photon interacts with a semiconductor, it generates electron-hole pairs. By applying a voltage across the semiconductor, these charges can be collected and measured as a current. The PN junction is a fundamental device used for photon detection. It consists of an n-type silicon joined with a p-type silicon, where excess electrons and holes combine at the middle of the device, forming a depletion area with an electric field across it. This electric field prevents further recombination of electrons and holes.

When a photon strikes the depletion area, creating an electron-hole pair, the electric field then causes each of these charges to drift toward the opposite electrode, generating a signal. Although PN diodes have a very narrow depletion region, PIN diodes offer improved performance. A PIN diode is a PN diode with an intrinsic material between the n-type and p-type semiconductors, resulting in a larger depletion region. Consequently, the PIN diode can capture more photons, leading to higher detection efficiency.

Unlike scintillators with PMTs, which have gains of approximately $10^6 - 10^7$, the gain in PIN diodes is only 1, resulting in a significantly smaller signal. To achieve a higher gain, a higher voltage (ranging from 200 V to 2000 V) must be applied across the diode. This high voltage accelerates the generated electron towards other atoms, causing it to eject additional electrons in a process that continues until they reach the electrode. This device is known as an avalanche photodiode (APD), and it can achieve gains as high as $10^2 - 10^3$, but it still does not match the gain of PM tubes. Another advancement in APDs is the single-photon avalanche diode (SPAD). The fundamental concept of detection in both APDs and SPADs remains the same, with the main difference being the bias voltage. In APDs, the voltage is lower than the breakdown voltage of the device, while in SPADs, the voltage is higher than V_{BD}, allowing them to detect signals as low as a single photon [16]. However, the gain in SPADs still does not rival that of PMTs.

An alternative to PMTs is the silicon photomultiplier (SiPM), used in conjunction with a scintillator. The SiPM consists of a parallel combination of numerous micro Single-Photon Avalanche Diodes (SPADs), with a quenching resistor for each of them [16, 17]. Fig. 2.2 illustrates the SPADs configuration, where the bias voltage is set higher than the breakdown voltage. When a photon passes through, the micro SPADs detect it, causing the voltage across them to drop below the breakdown voltage due to the quenching resistors. This drop in voltage stops the detecting process, and all charges are soon discharged through the resistor, causing the voltage to again go beyond the breakdown level and to be prepared for the next photon.

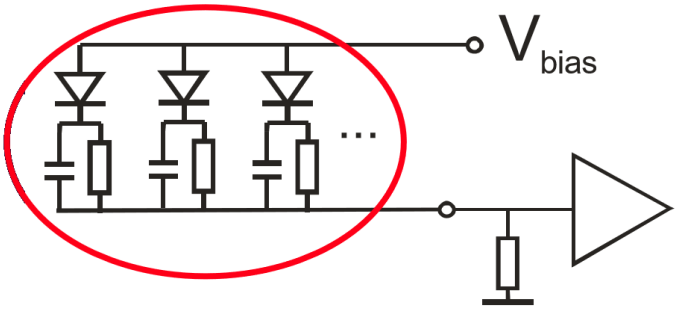


Figure 2.2: SiPM equivalent circuit

There are other types of semiconductors with higher atomic numbers that can be directly used to detect gamma-ray photons without the need for a scintillator. In recent times, cadmium zinc telluride (CZT) and cadmium telluride (CdTe) have demonstrated great potential for use in Single-Photon Emission Computed Tomography (SPECT) applications, where only one photon needs to be detected, and there is no timing requirement as there is in PET scanners. These detectors offer good resolution and sensitivity, making them promising candidates for certain imaging applications. However, their use in medical imaging applications is limited due to challenges in fabricating large-area detectors at a reasonable yield and cost. One of the challenges in implementing CZT and CdTe for high speed SPECT applications is the disparity between hole and electron transport where one charge carrier is much slower than the other. This issue was resolved by the introduction of a Frisch grid [18, 19]. The concept of Frisch grid is explained in the next section.

2.4 Frisch grid

In the pursuit of enhancing charge collection efficiency, the strategy of near-field preferential sensing of higher mobility carriers has demonstrated its effectiveness [20]. To achieve an artificial near-field effect in solid-state detectors, two primary techniques exist: the coplanar structure method and the incorporation of metal grid layers within the photoconductors [21, 22]. These methods are illustrated in Figure 2.3. Both methods are influenced by Frisch grid design in gas ion chambers. In a gas detector, positive carriers with lower mobility are not fully collected. To overcome this problem, one can add internal electrodes to make electrostatic shielding [23]. Then, the signal is only detected when positive ions have passed the internal grids, eliminating depth dependent signal variation. investigations have demonstrated the functionality of a Frisch grid a-Se detector with substantial temporal

resolution. However, a notable drawback arises from the noise levels observed, attributed to the utilization of low electric fields on both the grid and bias electrode. The theoretical basis will help to explain the problem of high amount of noise level in this design.

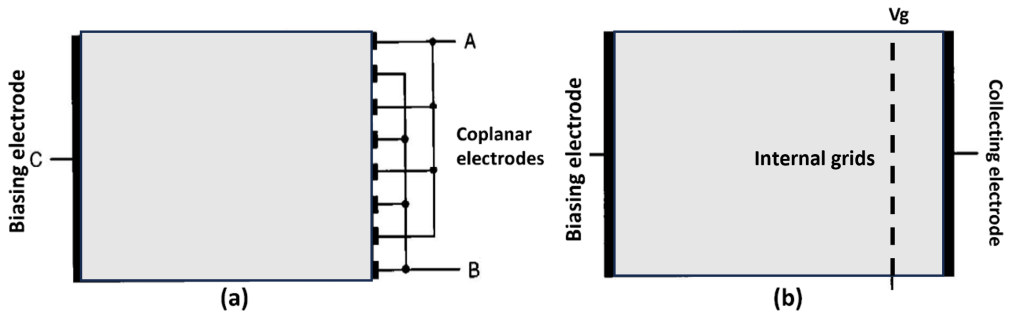


Figure 2.3: (a) Coplanar structure, (b) Frisch grid structure.

As discussed first by Shockley and Ramo, when the operation frequency becomes comparable to the transit time of collecting charges, a current is induced on the electrodes while charges move towards the electrodes [24, 25]. Shockely-Ramo theorem states that the induced current is directly proportional to the terminating electrostatic flux on the electrode as follows.

$$I_i = q\overrightarrow{v}.\overrightarrow{F}_w \tag{2.2}$$

Here, q is the charge of an electron, v is the instantaneous velocity of the charge and F_w is the weighting field factor under no space charge with grounding all other electrodes. Also, the induced charge on the related electrode is as follows.

$$Q_i = qV_w \tag{2.3}$$

Here, V_w is weighting potential under the aforementioned conditions. For a conventional planar electrode detector, as shown in Fig. 2.4(a), the weighting potential is simply a linear function calculated based on Shockely-Ramo theorem by assuming the potential of the anode is 1.

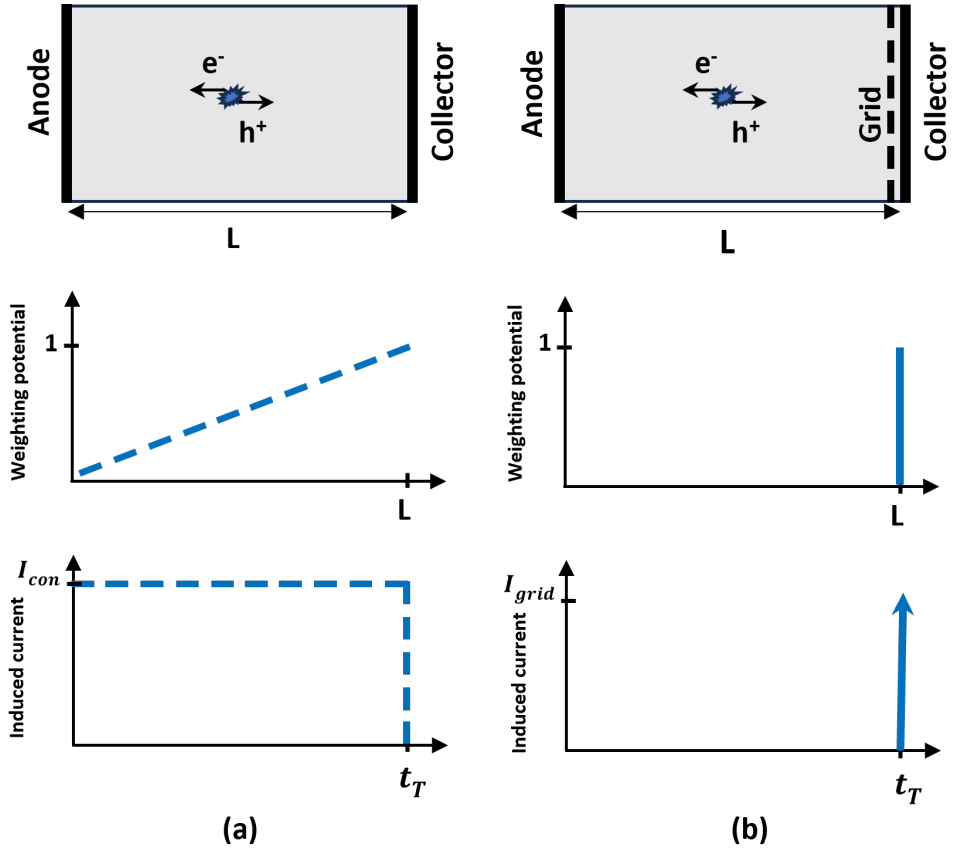


Figure 2.4: Weighting potential and induced current (a) Conventional, (b) Hypothetical single polarity sensing detector.

The current that is induced on the conventional electrode under certain conditions such as homogeneous medium and field distribution and coherent carrier drift is as follows [26].

$$I_{con}(t) = \frac{q}{t_T}(H(t) - H(t - t_T)) \tag{2.4}$$

Where H(t) is the Heaviside step function. Then, the induced photocurrent (I_i) in a single polarity sensing detector with a strong near-field effect within the close proximity of collecting electrode and no gap between grid and collector electrode is as follows.

$$I_i(t) = q\delta(t - t_T) \propto \frac{d}{dt} I_{con}(t) \tag{2.5}$$

One can see the induced photocurrent is not time transient and depth dependent and the only limitation is the overall rise time of the readout circuit. Fig. 2.4(b) presents the weighting potential and induced current for a single polarity sensing detector. A more practical weighting potential has been shown in Fig. 2.5.

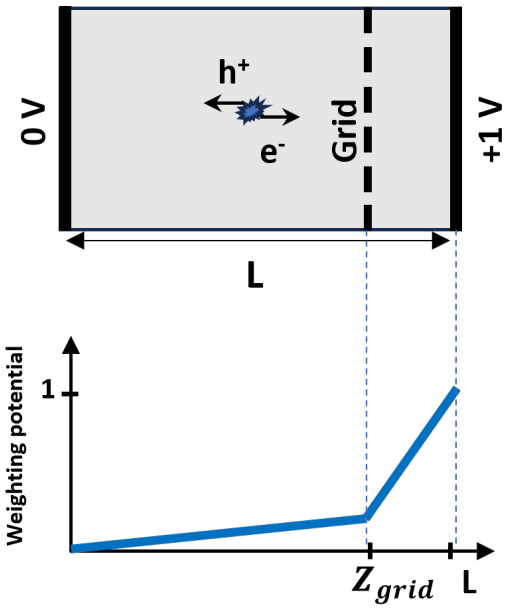


Figure 2.5: Weighting potential for a realistic single polarity sensing detector.

The near-field effect can be improved substantially by decreasing the grid-electrode gap. The rise time improvement is due to the insensitivity of the collector electrode to electron transport.

2.5 a-Se large-area photoconductor

Amorphous selenium, a widely recognized material historically employed in xerography during the 1960s and 1970s, has recently gained significant attention in the field of medical imaging engineering [27]. Moreover, a-Se boasts efficient absorption of hard x-rays and a low dark current attributed to its amorphous structure [28]. due to its comparatively modest X-ray sensitivity, efforts are underway to identify alternative X-ray photoconductors that could replace a-Se. Several polycrystalline semiconductors like CdZnTe [29], PbI2 [30],

and HgI2 [31, 32, 33] have the potential for large-area deposition. However, the majority of these photoconductors are currently challenged by excessively high dark current or inadequate charge collection efficiency. Additionally, some encounter difficulties in achieving uniform and homogeneous layers over large surfaces [34]. Therefore we investigate a-Se to address its limitations in the next chapters.

Positioned in Group VI of the periodic table with an atomic number of 34, selenium exists in two primary forms: amorphous and crystalline. While the crystalline structure offers enhanced stability, amorphous selenium demonstrates a tendency to gradually crystallize over time. In its crystalline state, selenium exhibits uniform bond lengths and bond angles over a considerable range, indicating a high degree of long-range order. Conversely, the amorphous phase displays slight deviations in bond lengths and bond angles, resulting in spatial disorder that extends beyond a few atomic radii, giving rise to short-range order. Despite its inherent predisposition for crystallization, the favorable optical and electrical properties of amorphous selenium have generated substantial interest in its application in medical imaging engineering.

In the context of medical imaging, amorphous selenium has emerged as a promising material due to its unique optical and electrical properties. Its efficient conversion of X-ray photons into electrical signals makes it well-suited for applications such as digital radiography and computed tomography (CT). Amorphous selenium-based detectors offer high spatial resolution, low noise levels, and a wide dynamic range, enabling improved image quality and diagnostic accuracy. Ongoing research and development efforts are focused on optimizing the performance of amorphous selenium detectors, enhancing their sensitivity and efficiency, improving response by means of incorporating Frisch grid structures within the semiconductor, and exploring new avenues for their integration into advanced medical imaging systems [35, 36, 37].

Current a-Se based direct conversion flat panel detectors suffer from low dose efficiency due to poor noise rejection, incorrect energy weighting, and the existence of temporal artifacts. To address these issues, a photon counting mode of operation has been suggested, which provides higher dose efficiency through effective noise rejection and optimal energy weighting without appearance of any temporal artifacts [38]. However, this method demands complex pixel circuitry. Moreover, some other parameters including resistivity, leakage, conversion gain, room temperature operation, and last but not least, operation at a high count rate should be carefully considered. a-Se provides high sensitivity, room temperature operation, and cost-effective large-area fabrication processes. However, despite much effort devoted to improving a-Se electrical properties, the low temporal resolution of the a-Se material still remains an issue, especially for thick layers of a-Se. It is due to insufficient electron mobility, the existence of high concentration trapping defects, and drifting

electrons having to traverse the variable range to the collecting electrode. Conversely, the collection efficiency of the holes is high. Altogether, all of these issues result in variable signal rise time and create depth-dependent noise.

2.5.1 Band structure

When atoms form covalent bonds, their atomic orbitals (AO) become conjugated and belong to all the atoms. These conjugated orbitals are called molecular orbitals (MO), with half of them being bonding states and the other half being antibonding states. There is a significant gap between these two groups, which is called the band gap. Antibonding states have higher energy than bonding states, so the electrons fill the bonding states and leave the antibonding states empty. In solid materials, the number of AOs is large enough that the MOs form a continuum, and the electrons can move between these states at room temperature. Thus, these states together are called a band, with the empty one at higher energy being the conduction band and the filled one at lower energy being the valence band.

When the band theory was developed from quantum mechanics, it was assumed that the structures are periodic, and only the interaction of wave functions with periodic wells was considered. This assumption results in two simplifications:

- Each electron is described by extended Bloch wave function with periodicity in phase and amplitude.
- The conduction and valence bands are separated by a sharp well-defined energy gap.

The first attempt to generalize the band theory to amorphous materials was based on the assumption that the Bloch wave functions keep the periodicity in amplitude, but their phases just have short range orders [39]. Thus, the sharp band edges were replaced by tails of localized states. These localized states are in the band gap area, which results in capturing the carriers and dropping the effective mobility. In the extended states, carriers have band transport mobility while in localized states, the mobility is limited by thermally activated tunneling. This change in mobility creates a gap in energy, called the mobility gap as illustrated in Fig. 2.6(b)[2].

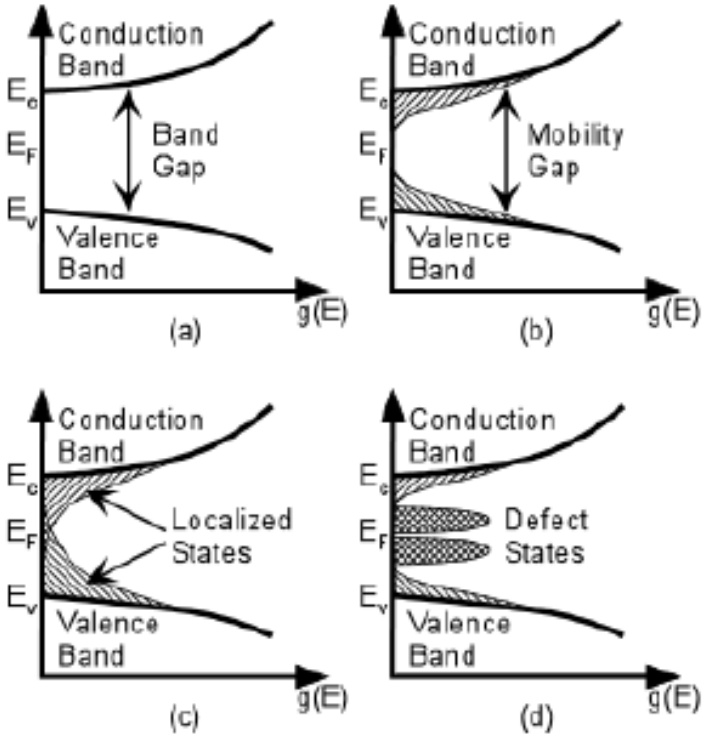


Figure 2.6: Evolution of band structure for amorphous semiconductors showing band structures for (a) the crystalline materials (b) the initial model for amorphous semiconductors proposed by Mott, (c) the CFO model, (d) and Marshall and Owen model [2].

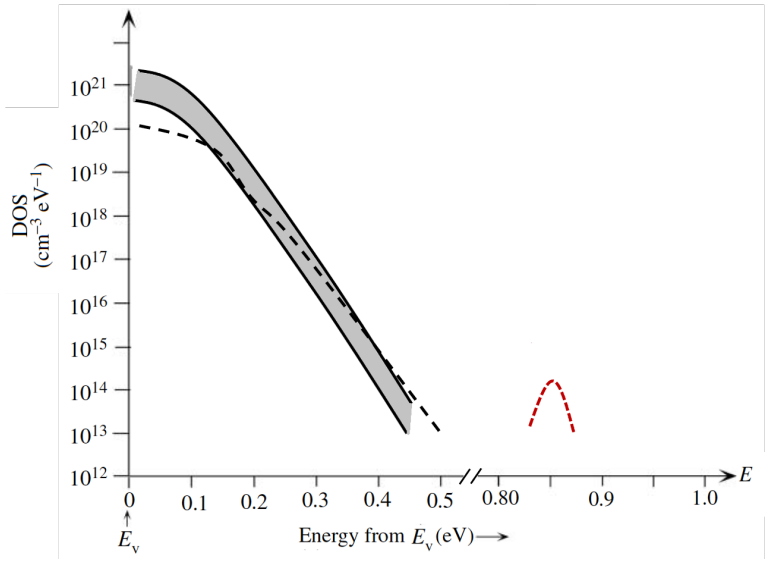
This model got more support by Cohen, Fritzsche and Ovshinski and is known as CFO model as shown in Fig. 2.6(c) [40]. The CFO model considers more disorder in amorphous materials, which results in more deep localized states through the mobility gap and even overlapping near Fermi level. One can say that the CFO model suggests the metallic behavior in the material because of the overlap, but these states are highly localized in space. This model has never been verified as a general model for amorphous materials, since they have more degree of short range order.

In solid materials, there are atoms in the network that are located differently from the normal structure bonding (NSB). Connectivity of amorphous materials highly depends on a local basis, which results in well-defined defect states. Defect states include dangling bonds, chain ends, vacancies, interstitials, and substitutional impurities. These states are highly localized and are located in the mobility gap beside the disorder induced states.

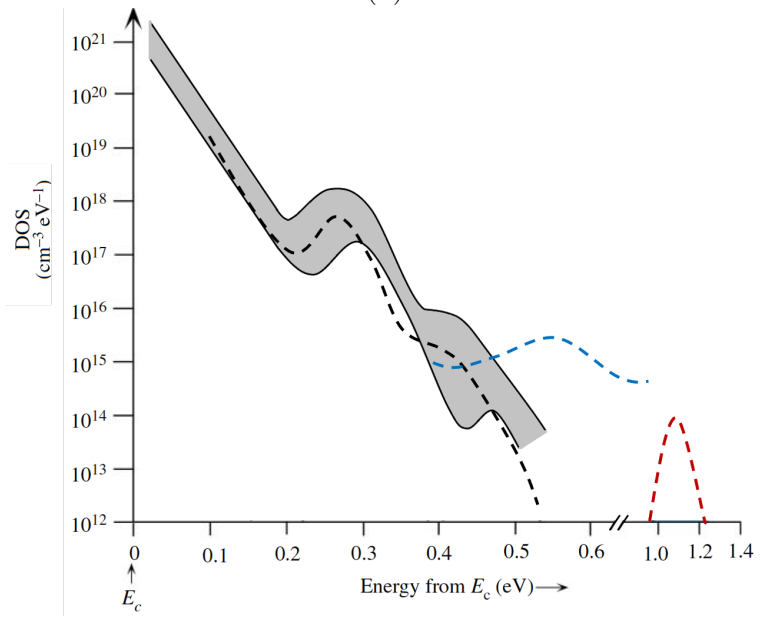
Previously, it was assumed that the density of tail states, which are from disorder in the network, was dominant enough to obscure the effect of defect states. Later, it was argued that the defect states play a significant role in the density of states in mid-gap (Fig. 2.6(d)) [41]. The band structure of a material is important to determine electrical and optical properties of that material, so knowing the origin of the states would help to modify these properties.

2.5.2 DOS of a-Se

Although much research has been done to figure out the exact density of states (DOS) of a-Se, but there are still some uncertainties around the proposed models. Each model contains different number of peaks with different locations and values. The model described here is based on from Kasap [3], which is a combination of different studies derived from time of flight (TOF), Interrupted-Field Time-of-Flight (IFTOF), and electographic measurements of cycled-up residual and dark discharge [42]. According to Fig. 2.7, there are localized states near the edge of the conduction band called shallow traps. The electron drift mobility is affected by these shallow traps at $\sim$ 0.27-0.31 eV below E_c. There is another peak near these states at $\sim$ 0.44-0.5 eV below E_c. There are deep electron traps, deep inside mobility gap around the Fermi level. The mobility gap in a-Se is around 2.1 eV. Hole mobility also is affected by shallow traps above the valance band. A deep hole trap is located near the Fermi level.



(a)



(b)

Figure 2.7: Replotted DOS of a-Se from Kasap [3], which combines data from different studies indicated by various line colors, styles, and shades [4, 5, 6, 7, 8, 9, 10]: (a) DOS near the valence band edge and mid-gap (related to hole traps), (b) DOS near the conduction band edge and mid-gap (related to electron traps)

2.6 Readout modes

The readout mode in this context refers to the methodology employed for quantifying the output signal from the detector. There are two main approaches: one involves the integration of the signal over a specific time interval to record its intensity, while the other adopts a photon counting strategy, where individual photons are detected. Both of these methodologies present distinct advantages and limitations, which will be explored in this section.

2.6.1 Energy integrating mode

The energy integrating mode has been a prominent approach in imaging for decades. This method involves accumulating the signal over a specific time interval, resulting in a measurement where the contribution of each photon to image formation is proportional to its energy. Due to its simplicity, compatibility with conventional technologies, and ability to achieve high signal-to-noise ratios, this approach has found widespread application in various medical and industrial imaging applications.

The passive pixel sensor (PPS) and the active pixel sensor (APS) are commonly employed architectures for energy integrating readout circuits. In a PPS, the charge generated by X-ray interactions is directed toward a collecting electrode under an applied electric field. Subsequently, the charge is stored on a storage capacitor during the integration time [43]. On the other hand, the APS, leveraging complementary metal-oxide-semiconductor (CMOS) technology, utilizes three transistors (3T) for charge conversion and storage [44]. The integration time in these systems can be adjusted to optimize image quality and exposure dose.

One of the primary advantages of energy integration is its ability to offer high signal-to-noise ratios, especially in scenarios where the generated signal is substantial. This makes it suitable for general X-ray imaging applications, such as radiography and computed tomography (CT). Energy integrating systems have been extensively deployed in these applications, delivering reliable and consistent imaging results.

Despite its widespread use, the energy integrating mode does have certain limitations. In mammography, for instance, where the primary objective is to visualize soft tissue variations and detect subtle abnormalities, lower energy photons carry crucial contrast information. However, the energy integration mode tends to emphasize higher energy photons, leading to a counterproductive weighting that can potentially compromise the quality of the resulting images. To tackle this challenge, researchers have suggested alternative

weighting schemes, such as inversely proportional to the cube of the photon energy which cannot be realized with energy integrating systems [45].

Another limitation of energy integrating systems is the inherent problem of noise, originating from both the detector and the readout circuit. The poor noise rejection in energy integrating mode restricts the signal-to-noise ratio (SNR) of the system, leading to compromises in image quality and necessitating higher patient doses, particularly in high frame rate applications. This amplifier noise limitation becomes more pronounced in scenarios where short acquisition times are required, as the X-ray generated signal becomes lower, and the integrated noise becomes more prominent.

2.6.2 Photon counting mode

Photon counting readout circuits offer an alternative and promising approach to overcome the limitations of energy integration in X-ray imaging. Instead of measuring the total intensity of incident photons, photon counting systems directly count individual photons above a specific threshold. This allows for precise energy weighting, making it useful in applications where contrast enhancement and dose reduction are important.

The operation of a photon counting system involves charge amplification to generate voltage output, low-level discrimination, threshold adjustment, and event counting. By adjusting the threshold, an optimal threshold can be achieved, leading to accurate energy weighting and improved soft tissue imaging. Photon counting readout circuits offer several advantages over energy integrating mode, particularly in applications like mammography and low-dose X-ray imaging. By counting only the photons that exceed the threshold, photon counting systems can significantly reduce the patient dose compared to energy integration. This reduction in patient dose is of utmost importance in medical imaging, where minimizing radiation exposure while maintaining image quality is critical.

Moreover, photon counting systems can operate in a quantum noise-limited regime when appropriately designed, offering superior noise performance compared to energy integrating mode. This improved noise performance contributes to higher image quality and better visualization of subtle details in the acquired images. However, photon counting systems also present certain challenges and limitations, including the potential reduction in dynamic range, particularly in high-intensity scenarios. Since photon counting relies on individual photon detection, systems may face saturation issues when a large number of photons are simultaneously detected, potentially limiting the dynamic range of the imaging system. One solution could be combination of both methods to use integration mode at higher rates and use photon counting mode at lower rates [46].

2.7 Characteristics of the detector

There are multiple characteristics for an effective large-area detection system that need optimization to achieve better performance. This section examines a few of these characteristics.

2.7.1 Sensitivity

The sensitivity of a detector is the overall conversion efficiency of the radiation to the collected charge. This efficiency itself consists of three parts.

Absorption of photon

An incoming photon interacts with the material and attenuates until it finally gets completely absorbed in the best case scenario. The expression that defines the absorption efficiency is given below.

$$\eta(E) = 1 - e^{-\alpha(E)L} \tag{2.6}$$

L is the thickness of the material and α is attenuation coefficient. For having high quantum efficiency, L should be much larger than attenuation depth (α^{-1}). α itself depends on three factors: energy of the incident photon, atomic number, and density of the material. α decreases with photon energy and gets larger with atomic number and density. Fig. 2.8 shows α for several materials. Higher Z photoconductors such as CdTe have higher absorption efficiency compared to a-Se at higher energies.

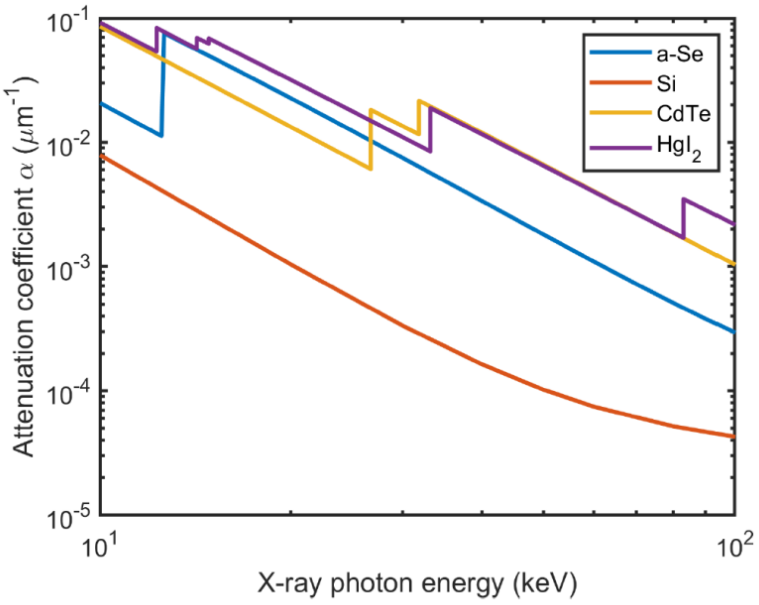


Figure 2.8: Attenuation coefficient for different materials generated from [11].

EHP creation

This term is actually photogeneration efficiency. W is the required energy to generate a single electron-hole pair. Due to Klein's rule [47], W for crystalline materials is proportional to the value of E_g by a factor of 3 ($W \approx 3E_g$) although low mobility materials are exceptions. For amorphous materials such as selenium, the expression indicates dependency of W on the electric field. W can be measured by two methods for a-Se, first by using PHS (pulse height spectroscopy) and the second by photo-induced discharge. The measurements show that W is dependent on three factors including photon energy, electric field, and temperature, as can be seen from the following expression.

$$W_{\pm} \approx W_{\pm}^{\circ} + \frac{B}{F} \tag{2.7}$$

Constant $B = 4.410^2$ eV is weakly dependent on energy and W° is intrinsic W which is around 6eV for selenium. Lower W is more desirable to generate as many electron hole pair (EHP) as possible, so increasing the electric field helps to decrease W. However, working at a high electric field causes dark current to become more significant.

Charge collection

Charge collection efficiency is the ratio of collected EHPs to the total EHPs generated by radiation. Some of the generated EHPs become stuck in localized carrier traps, which eventually can go through recombination. Carrier migration distance, before it is trapped or recombined, is called the carrier schubweg. In order to minimize loss of EHPs, the whole path from EHP generation to the collecting electrode should be less than the carrier schubweg ($L \ll \mu\tau E$). However, for maximum absorption of photons, L should be larger than the attenuation length, so $\frac{1}{\alpha} < L < \mu\tau E$. To satisfy this condition, the carrier schubweg should be large enough, and increasing the electric field would help but increasing the electric field can also increase dark current.

2.7.2 Dark current

Dark current is the current recorded in absence of radiation. There are two main sources for dark current: thermal carrier generation and carrier injection from electrodes. High dark current reduces the SNR and increases the rate of crystallization in a-Se, because of Joule heating. Also, it reduces dynamic range by charge accumulation on the storage capacitor.

Dark current in a-Se detectors is mainly caused by hole injection from the positive electrode. To reduce hole injection, a hole-blocking layer (HBL) is used between the positive electrode and a-Se. This HBL should have very low hole mobility and high hole trap density. Even without HBL, a-Se has the lowest dark current among other photoconductors because of its amorphous structure. a-Se detectors can have dark current as low as 1 pA/mm^2 for an applied electric field of 20 $V/\mu m$ [48]. Polyimide has shown great potential as an HBL and even with electric fields as high as $80V/\mu m$, the dark current density can be kept under $1nA/mm^2$ [49].

2.7.3 Temporal response

When assessing the performance of direct conversion photoconductors in X-ray imaging, two crucial factors come into play: lag and ghosting. Lag refers to the phenomenon where image charge spills over into the subsequent image frame due to the thermal release of trapped charge. This results in an increased dark conductivity after the X-ray pulse has ceased. The injection of charge from biased electrodes during X-ray exposure contributes to the occurrence of lag [50]. On the other hand, ghosting refers to a reduced detector

sensitivity caused by the recombination of trapped charge with photogenerated charge during subsequent X-ray exposures. Therefore, charge trapping and the release of trapped charge can be considered the main sources of ghosting and lag [51].

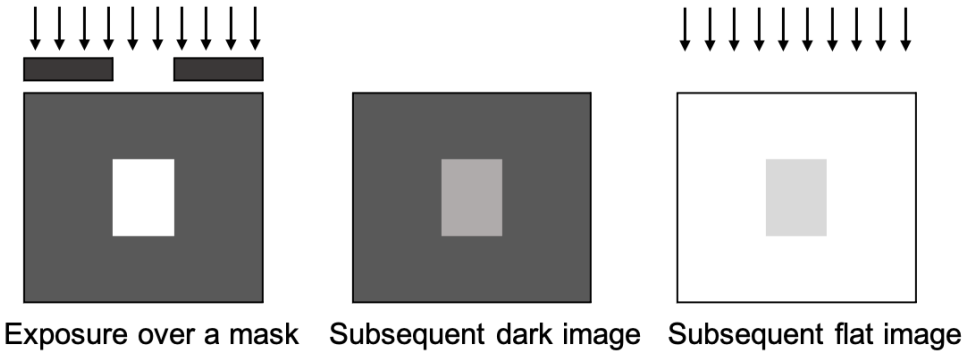


Figure 2.9: The appearance of lag and ghosting after an exposure over a mask.

As depicted in Fig. 2.9, lag manifests as higher pixel values in the previously exposed area, while ghosting is characterized by reduced pixel values. Ghosting can only be observed in the subsequent X-ray images. The temporal response of a detector becomes especially critical in high frame rate imaging applications like fluoroscopy.

Image lag poses a pervasive challenge for most direct conversion photoconductors, including materials like HgI2 and PbO, which limits their suitability for commercial FPDs. However, it has been demonstrated that ghosting is not a significant issue within the clinical dose range. Its impact becomes more pronounced at higher doses, where it poses a considerable problem.

Chapter 3

Multilayer Detectors for High-Energy Imaging

3.1 Introduction

High-energy radiation imaging applications in medical imaging primarily involve nuclear imaging. Nuclear imaging relies on the detection and tracking of emissions originating from a radioactive substance known as a radiotracer within the body. A radiotracer is administered to the patient through injection and is designed to target a specific organ or disease. This type of imaging is referred to as functional imaging because it demonstrates the level of activity within cells, which correlates with the accumulation of radiotracers in a specific region enabling the diagnosis and treatment planning. These functional images are captured by specialized cameras revealing insights like identifying epilepsy regions or determining cancer stages.

Single Photon Emission Computed Tomography (SPECT) is a widely used nuclear imaging system that relies on radiotracers emitting a single gamma photon per decay event. Common radiotracers in SPECT, such as ^{99m}Tc, ^{111}In, and ^{123}I, emit gamma rays within the energy range of 140keV-160keV. However, as photons are emitted in all directions, collimation becomes necessary to accurately determine the direction of impinged photons. The collimator, along with the detector and readout electronics, constitutes the main components of a SPECT camera. The collimator plays a crucial role in the performance of SPECT systems, as it decreases the system's total detection efficiency, also known as photon sensitivity, to lower than 0.01% for conventional SPECT cameras [52]. The

sensitivity of the system is highly dependent on the design of the collimator, and different types of collimators can improve the sensitivity to some extent.

In conventional SPECT detectors, gamma-ray photons are converted to optical photons using scintillators, often NaI(Tl) crystals. These optical photons then pass through photomultiplier tubes (PMT) to generate electrons, which are collected at the end of the PMT. However, the optical photons produced by scintillators are emitted isotropically, resulting in poor spatial resolution (around 3.7 mm) [53]. Additionally, PMTs are bulky, expensive, and susceptible to magnetic field interference. To address these challenges, a promising solution is to transition to the direct conversion process, where gamma-ray photons are directly converted to electron-hole pairs. Direct conversion materials have better spatial resolution since there is no optical conversion step that adds blurring, rather, a large electric field is used to separate electron-hole pairs generated due to photon absorption in a semiconductor. Direct conversion materials are also compact, mostly immune to magnetic field interference (a problem in MRI rooms), and can have better stopping power that yields higher sensitivities. Semiconductors with high atomic numbers and wide energy band gaps, such as cadmium zinc telluride (CZT), have the potential to be excellent candidates for direct conversion.

In a recent publication, the sensitivity of a SPECT camera based on CZT was reported to be around 0.1% using a novel collimator configuration [54], a factor of 10X higher compared to commercial NaI(Tl) cameras. To maintain comparable detection efficiency to NaI(Tl) crystals (typically 10mm thick), the authors used 5mm thick CZT detectors. Thus, the enhanced sensitivity of the SPECT system arose primarily from the new collimator configuration and not the direct conversion CZT material although the benefits of compactness and immunity to magnetic fields are still present. Due to fabrication limitations, 36 CZT detectors were required to cover a large area, which also impacted the affordability of the system. Also, although CZT has a higher density and stopping power compared to NaI(Tl), its fabrication process is expensive due to long crystal growth times and inconsistent yield.

To address the challenges of affordable large-area manufacturing, an alternate solution is to utilize a cost-effective, mature, direct conversion semiconductor, such as amorphous selenium (a-Se) that could be used with different collimators based on specific application needs. a-Se has gained significant attention in X-ray imaging applications and has been available commercially for many years for X-ray mammography, distinguishing it from other candidates. This popularity can be attributed to the high spatial resolution of a-Se direct conversion material that is very beneficial in finding micro-calcifications in the breast. In addition, a-Se's mature fabrication process for large-area direct conversion imaging, as well as its direct coupling capability to readout circuits, reduces system complexity. Although

they are not currently used for higher radiation energies due to the low stopping power of a-Se material, a-Se-based detectors hold the potential to overcome existing limitations with CZT-like direct conversion materials relating to cost, growth yield, and bonding issues. Moreover, a-Se has a well-established reputation for high spatial resolution, providing a notable advantage over alternative materials used in SPECT detectors.

While a-Se based detectors hold significant potential for practical applications, certain challenges still need to be addressed for their widespread deployment. Specifically, the low energy absorption of a typical a-Se thickness (up to 1 mm) within the energy range of 140keV to 160keV, as well as the low temporal resolution, remain unresolved. To tackle the first limitation, this chapter[1] focuses on the utilization of multiple layers of a-Se detectors, stacked to increase detection efficiency, and investigates the resulting effects on spatial resolution using established metrics such as point spread function (PSF) and modulation transfer function (MTF).

3.2 Proposed design

The proposed design for the multilayer detector configuration incorporates a holder structure that serves the purpose of stacking and organizing all detectors on top of each other. This holder plays a critical role in ensuring proper alignment and stability of the detectors within the system, as illustrated in Fig. 3.1. The holder's base is designed with multiple grooves, allowing for flexibility in accommodating detectors of different sizes. Furthermore, the brackets themselves feature grooves that enable the stacking of additional brackets, thereby increasing the number of detectors in the stack. Each bracket has an edge specifically designed to tightly secure the detector in place, assisted by four clips positioned at the corners. The assembly of this design is straightforward, extendable, and reminiscent of Lego pieces, making it user-friendly and adaptable. The spacing between detectors or brackets has been set to 2 mm. However, the spacing between the detectors will be thoroughly examined in the subsequent section through simulations to evaluate its impact on the detector's performance. The holder design can accommodate both edge-on and face-on illumination structures, making it suitable for various experimental setups.

One layer of a-Se detector has different sublayers starting with a thin layer of polyethylene terephthalate (PET) as the substrate. The selection of a thin PET layer allows for a compact design, minimizing the distance between detectors, while also providing the option for printed circuit readout. Following the substrate is the positive electrode and

[1]Parts of this chapter have been published in [55]

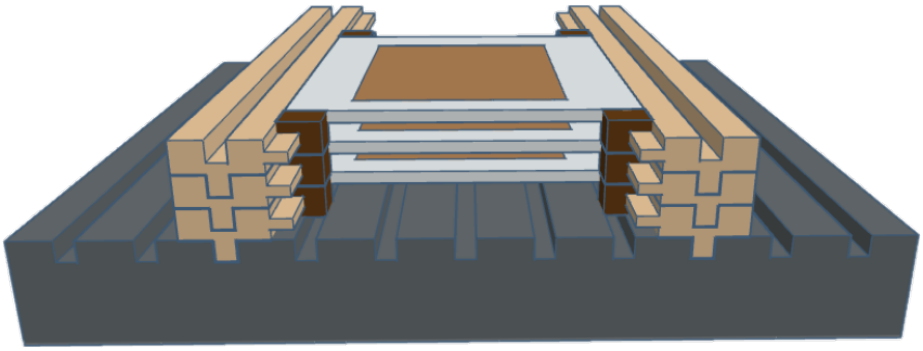


Figure 3.1: 3D design of the detector holder with three detectors stacked on top of each other.

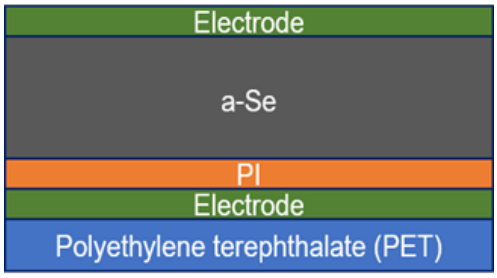


Figure 3.2: Illustration of the structure of a single detector layer featuring sublayers.

since the dark current in a-Se detectors is mainly caused by hole injection from the positive electrode, using a hole-blocking layer is necessary. In this case, polyimide (PI) is used because it can lower dark current significantly[56]. Not only does PI lower the dark current, but it also contributes to preventing a-Se from crystallization which improves the stability. After PI layer, a-Se photoconductor is used. Finally, the negative electrode, which in this case is the same material as the other electrode, is at the top. To maintain a compact design while minimizing the distance between detectors, a thin PET (polyethylene terephthalate) layer is chosen as the substrate. The PET layer can also be utilized for the printed circuit readout. On top of the substrate, a-Se (amorphous selenium) photoconductor is sandwiched between metal electrodes. Additionally, a hole-blocking layer was positioned between the positive electrode and the a-Se layer, ensuring proper functioning by reducing the dark current. In the subsequent section, Monte Carlo simulation studies will be presented, considering detailed geometry designs in the simulation framework.

3.3 Monte Carlo simulation

In order to simulate multilayers of a-Se detector, the Geant4 toolkit is used here. Geant4 is a Monte Carlo simulation tool that simulates particle interactions with matter. The structure shown in Fig. 3.2 was used for each detector layer to define the geometry in Geant4 with geometry properties listed in Table 7.1. The inclusion of electrodes, specifically made of aluminum (Al), serves the purpose of accurately simulating the interactions between photons and matter. It should be noted that a-Se with the practical maximum thickness available in the industry (1mm) is used in this simulation.

Table 3.1: Geant4 Geometry Parameters

Parameter	**Value**
Detector size	$45mm \times 45mm$
Pixel size	$1mm \times 1mm, 50\mu m \times 50\mu m$
Gap between detectors	$1\mu m$ to 2mm
a-Se thickness	1mm
Electrodes (Al) thickness	$100nm$
PI thickness	$1\mu m$
PET thickness	$50\mu m$
a-Se density	4.26 $g.cm^{-3}$
Electrodes (Al) density	2.77 $g.cm^{-3}$
PI density	1.42 $g.cm^{-3}$
PET density	1.38 $g.cm^{-3}$

For simulating the radiation, a particle gun is used to emit 140 keV gamma photons to the center of the detector stack. 10^6 photons are simulated and interactions with more than 10 keV energy depositions were recorded. Photoelectric events, scatterings, X-ray fluorescence, and Auger electron emissions are included in physics of Geant4 in order to record the location of energy depositions accurately. These recorded events are used in post processing to compute PSF and MTF. PSF is used to investigate the effect of Compton scatter events on spatial resolution. PSF shows how much a point source degrades and broadens by a detection system. In these simulations, the only sources of broadening are

scattering and reabsorption. For integrating detectors, the PSF is based on the amount of signal integrated at different locations relative to the impinged pixel. However, in a photon counting detector (PCD), PSF is based on the probability of counting a photon with an energy above the threshold at different locations relative to the impinged pixel. Stierstorfer et al.[57] showed how frequency-dependent metrics of a PCD can be computed with a Monte Carlo method. They used the Geant4 hit list and calculated PSF using the following equation

$$\mathrm{PSF}(v = \boldsymbol{u} + \Delta m) = \overline{a_m^{(0)}}(\boldsymbol{u}), \tag{3.1}$$

where $\boldsymbol{u}$ is the grid shift relative to the impact location which can be inferred as the offset of impact location from the center of the pixel, Δ is the pixel pitch, and m is the pixel number. Moreover, $a_m^{(0)}(\boldsymbol{u})$ is a random variable representing the output of pixel m if the photon hits pixel 0 with offset $\boldsymbol{u}$. They estimated this value by averaging over the simulated photons using

$$\overline{a_m^{(0)}}(\boldsymbol{u}) \approx \frac{1}{P}\sum_{p=1}^{P}\gamma_{p,m}(\boldsymbol{u}), \tag{3.2}$$

where P is the number of simulated photons and $\gamma_{p,m}(\boldsymbol{u})$ is 1 if a count is registered at pixel m for the photon p; otherwise, it is 0. We used the same approach with an assumption that the initial photon hits the center of the pixel, so $\boldsymbol{u}$ is 0. They used only the close neighbors of the impinged pixel since the charge sharing was a major concern. Here, the main issue is scattered photons and they travel further away, so we are not limited to the nearest neighbors. Moreover, we used multiple detector layers and counts were added up over different layers for pixels with the same row and column coordinates. Therefore, the PSF should display the probability for a larger neighborhood of the pixel. Having more layers increases the chance of having multiple counts for a single photon, which can be reduced by increasing the threshold energy as discussed in the next section. After plotting PSF in the 2D plane, the next step is to generate the MTF curves.

The MTF is the Fourier transform of line spread function (LSF) and LSF is the 1D integral of PSF. Thus, by integrating the PSF over rows, the LSF along the column is obtained which is similar to the LSF along rows since the PSF is symmetrical. Then, applying the Fourier transform and appropriate scaling result in the MTF of the detector[58, 59, 60]. The MTF was corrected for the finite extent of a pixel aperture a, using the Nyquist frequency $f_N = \frac{1}{2a}$

$$\mathrm{MTF}(f)_{\mathrm{System}} = \mathrm{MTF}_{\mathrm{detector}} \times \mathrm{MTF}_{\mathrm{Pixel}} = \mathrm{MTF}_{\mathrm{detector}} \times \mathrm{sinc}((\frac{\pi f}{2f_N})). \tag{3.3}$$

Moreover, the detection efficiency was calculated based on the number of registered counts divided by the number of photons.

It is important to acknowledge that the scattering of photons can lead to multiple hits, potentially resulting in a calculated detection efficiency that surpasses 100%. In order to address this issue, our study explored two different approaches. The first approach involved increasing the energy threshold, considering only events where the deposited energy by the photon exceeded the threshold value. By raising the threshold, we focused on interactions that led to immediate absorption, thereby reducing the likelihood of multiple hits for a single photon. Additionally, we investigated a straightforward correction method proposed by Thilo et al. [61] that provided an alternative means to calculate the corrected detection efficiency, $DE_{corrected}$ and the Detection Quantum Efficiency at zero frequency, $DQE(0)$,

$$\mathrm{DE}_{\mathrm{corrected}} = \frac{N_{\mathrm{true}}}{N_{\mathrm{in}}}, \tag{3.4}$$

$$\mathrm{DQE}(0) = \frac{N_{\mathrm{meas}}^2}{N_{\mathrm{in}} \sum_{i=1}^{\infty} i^2 N_i}, \tag{3.5}$$

where N_{in} is total number of input photons and N_{meas} is number of recorded counts which includes N_1 single counts, N_2 double counts and so on

$$N_{\mathrm{meas}} = N_1 + 2N_2 + 3N_3 + ... = \sum_{i=1}^{\infty} iN_i, \tag{3.6}$$

While N_{true} only considers the number of photons counted without considering multi-counts.

$$N_{\mathrm{true}} = N_1 + N_2 + N_3 + ... = \sum_{i=1}^{\infty} N_i. \tag{3.7}$$

We conducted simulations for different numbers of layers to investigate the effect of scattering on the MTF and detection efficiency. Then, we set the number of layers for our default structure to 3 for ease of fabrication and simulation, as well as investigating all relevant metrics. For this structure, the energy threshold ranged from 10 keV to 130 keV, and the gap between layers ranged from 1 μm to 2 mm to investigate their impacts on the spatial resolution and efficiency of the detector. After choosing the design with 3 layers with each layer having a thickness of 1 mm, resulting in a total thickness of 3 mm, We explored various combinations of the number of layers and their individual thicknesses, while maintaining the same total thickness as the chosen design. Additionally, we conducted supplementary simulations for a specific thickness of 0.1 mm, which closely matched the experimental thickness readily available.

3.4 Simulation results

In order to examine the variations in energy thresholds, Pulse Height Spectra (PHS) was generated for ten detector layers using two different pixel sizes. Fig. 3.3 presents the results on a logarithmic scale, allowing for the detection of lower counts associated with Compton scattering. Furthermore, a Point Spread Function (PSF) was plotted for an energy threshold of 110 keV, indicated by a rectangle in the PHS graph. The color scale is logarithmic, providing clear visibility of the distinctions between pixels. The PSF reveals a distinct peak at the center for the 1mm pixel size in comparison to the $50\mu m$ pixel size.

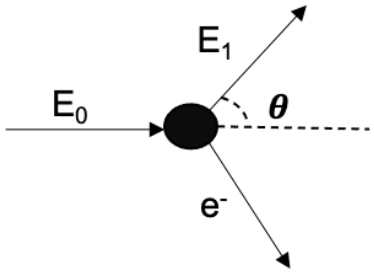


Figure 3.4: A photon undergoing Compton scattering.

In Fig. 3.3a, the PHS displays a noticeable reduction in counts within the energy range of 50 keV to 90 keV, emphasizing the impact of Compton scattering kinematics (Truong et al., 2007). When a photon with an energy of E_0 undergoes scattering as depicted in Fig. 3.4, the energy of the scattered photon, denoted as E_1, can be determined using the following equation:

$$E_1 = \frac{E_0}{1 + \frac{E_0}{m_0 C^2}(1 - \cos\theta)}, \tag{3.8}$$

Here, $\cos\theta$ defines the upper limit for the energy absorbed by the excited electron or the lower limit for the energy of the scattered photon.

$$0 < E_{e^-} < E_0 \frac{\frac{2E_0}{m_0 C^2}}{1 + \frac{2E_0}{m_0 C^2}}. \tag{3.9}$$

Based on equation 3.9, during the initial Compton event, a 140 keV photon can deposit a maximum of 49.6 keV of energy when scattered at a 180-degree angle. The energy of the scattered photon would fall within the range of 90.4 keV to 140 keV, which can be

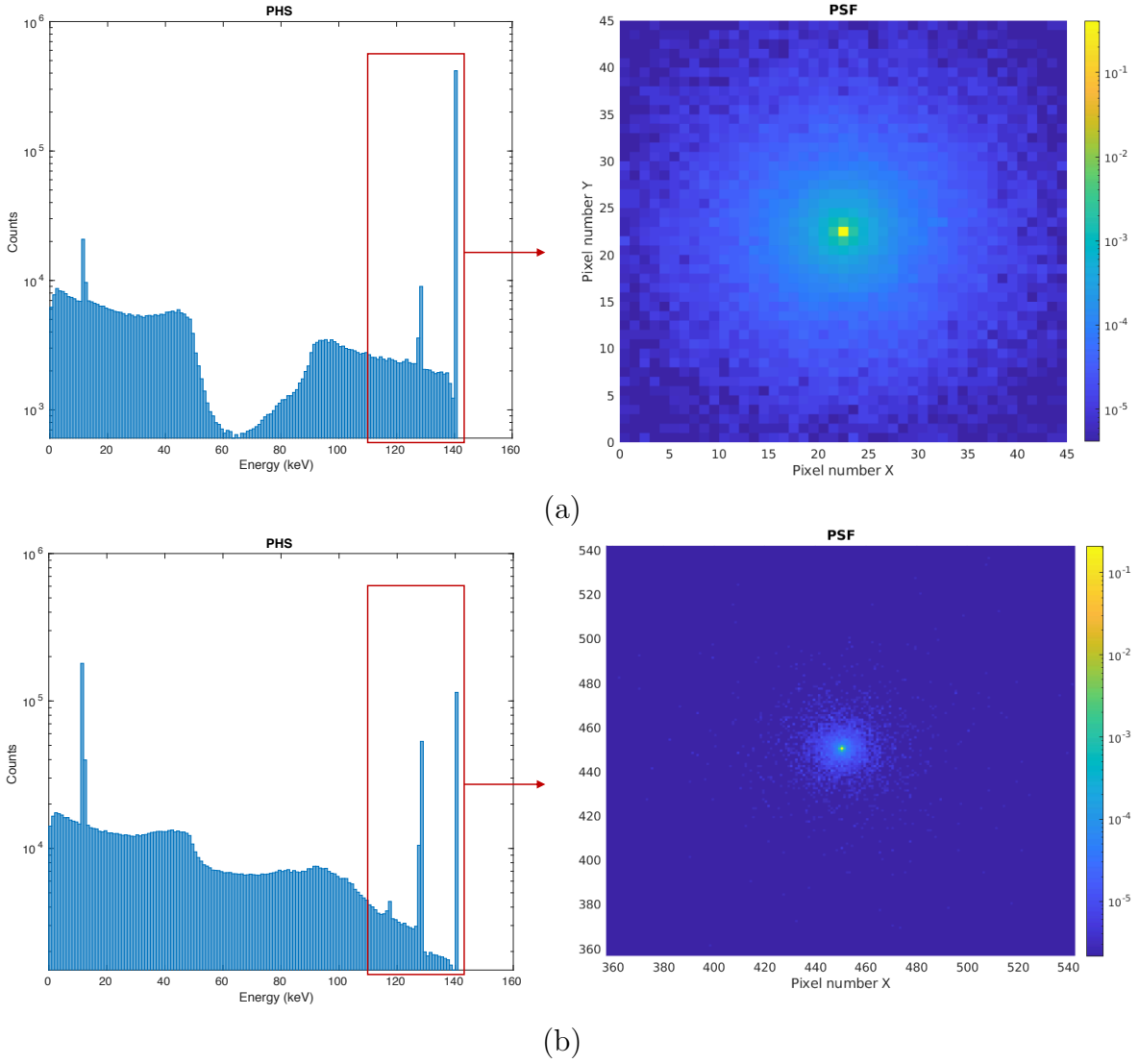
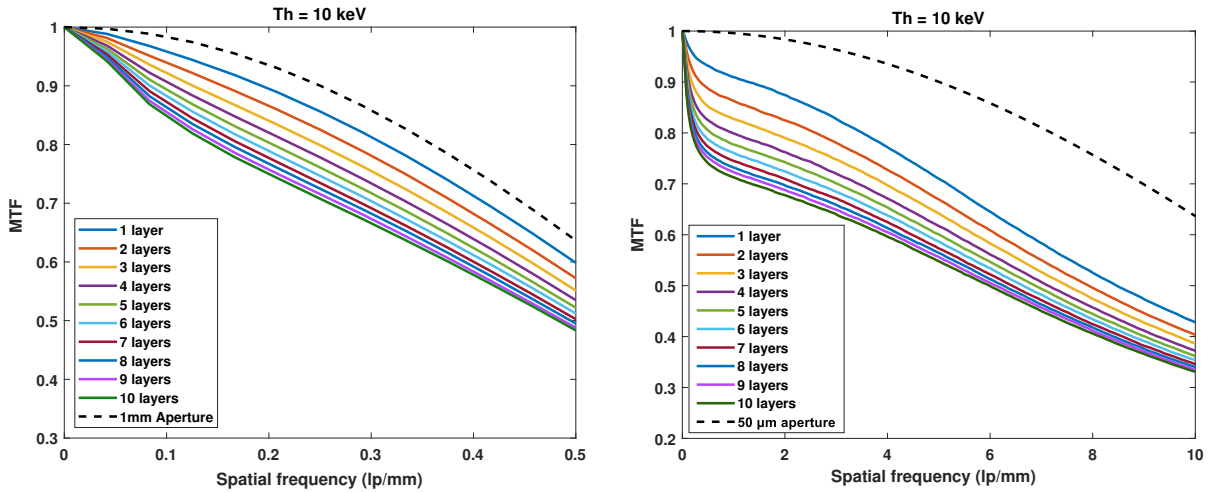


Figure 3.3: PHS and PSF histograms. PSF is computed for energy bins shown in PHS and colors represent probability values $\in [0, 1]$ in logarithmic scale: (a) 1 mm pixel pitch, (b) 50 μm pixel pitch.

absorbed by other pixels or layers. The scattered photon has two possibilities: it can either undergo the photoelectric effect and deposit all its energy into the material, or it can undergo another Compton scattering event, potentially depositing only a portion of

its energy. The lower limit for E_1 at the end of the second scattering event is 66.8 keV, corresponding to a 180-degree scattering event for a 90.4 keV photon. This scattered photon may undergo another interaction with the material to deposit all its energy or go through another scattering event. It is worth noting that the likelihood of having three scattering events is considerably lower compared to single scattering events, especially in the case of a 1mm pixel size. This is primarily due to the larger area of the pixel, where scatterings can occur within the pixel boundaries and be registered as a single event. On the other hand, smaller pixel sizes allow for the occurrence of fluorescence and reabsorption in adjacent pixels. This leads to a more prominent K-edge peak and an increased count in the energy range between 49.6 keV and 90.4 keV when compared to the counts observed with a 1mm pixel size.



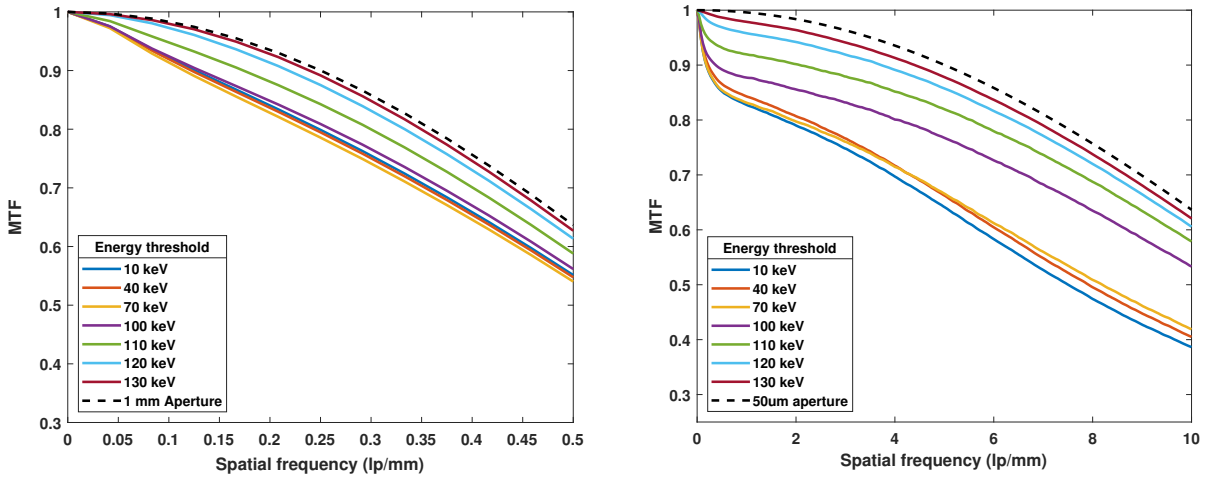
(a) (b)

Figure 3.5: MTF for the number of layers from 1 to 10. (a) 1 mm pixel pitch. (b) 50 μm pixel pitch

An essential component in evaluating spatial resolution is the MTF. To explore the influence of energy threshold and the number of detector layers on spatial resolution, only the Modulation Transfer Function (MTF) of the system is calculated moving forward.

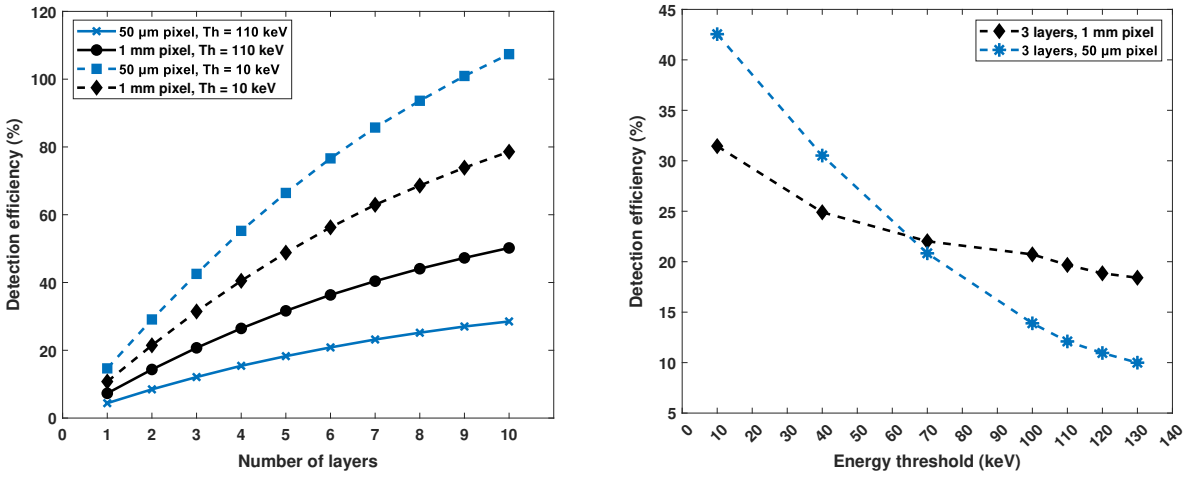
The MTF in Fig. 3.5 is plotted up to the Nyquist frequency since there are no sub-pixels in this structure. Thus, a line pair requires at least two pixels to be captured. Fig. 3.5a shows that for the 1mm pixel size, the total MTF is much closer to the pixel

MTF (dashed line) for a lower number of layers. The spatial frequency at which MTF reaches 0.5 (MTF50) is a common standard for the spatial resolution of the detector. Observing MTF50 shows that increasing the detector layers to 10 has a minimal effect on the resolution of the detector for the 1mm pixel size. However, if we use $50\mu m$ pixel size, the MTF is more detector dependent such that increasing the number of layers reduces the MTF to less than 0.5 within the Nyquist range which results in a degraded spatial resolution ($70\mu m$ to $125\mu m$) compared to the pixel size (Figure Fig. 3.5b). This resolution is still considered a high spatial resolution for SPECT applications. Thus, we conclude that a high-resolution SPECT detector is achievable by increasing the number of direct conversion layers.



(a) (b)

Figure 3.6: MTF for different energy thresholds in 3 detector layers. (a) 1 mm pixel pitch, (b) $50\mu m$ pixel pitch.



(a) (b)

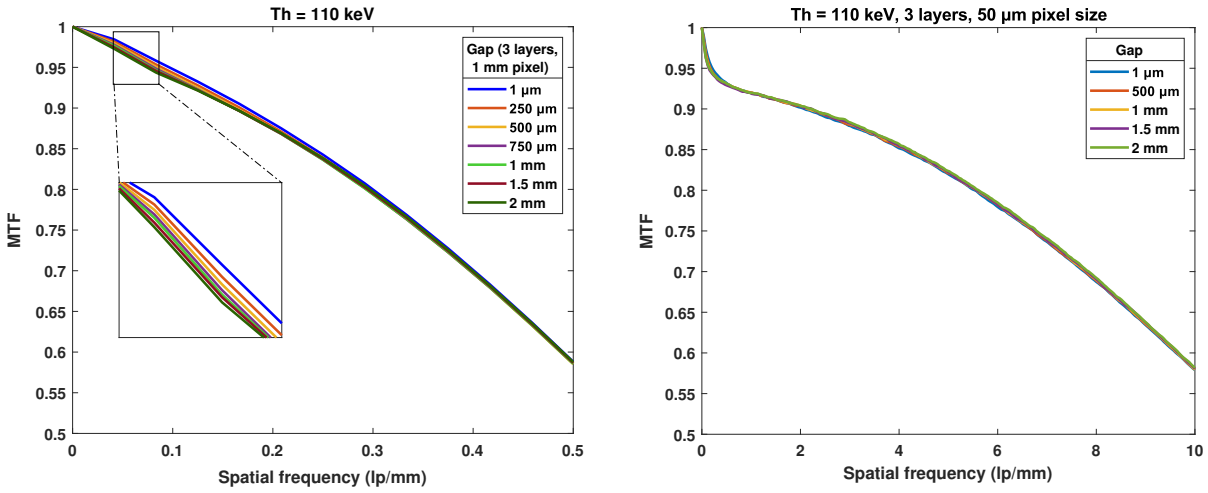
Figure 3.7: Detection efficiency. (a). For the number of layers from 1 to 10. (b) For different threshold energies

On the other hand, using more detector layers increases the detection efficiency, which is expected because of the higher energy absorption by a larger stack of a-Se detectors. It should be noted that, as shown in Fig. 3.7a, detection efficiency goes beyond 100% due to the increase in multiple counts per photon mentioned in the previous section, specifically if the threshold is very low (10 keV here). To lower the probability of having multiple counts, here we increased the energy threshold, which improves the MTF, but it decreases the efficiency significantly (Fig. 3.7b). As we see in Fig. 3.6, by increasing the threshold, the MTF eventually reaches the aperture limit.

Fig. 3.7b shows that for the 50 μm pixel and thresholds below 70 keV, which is half of the maximum of energy, the efficiency is higher than that of the 1 mm pixel. This happens because the scattering between layers introduces noise counts. However, after 70 keV most of such noises are filtered out and the efficiency becomes less than that of the 1 mm pixel. This is expected because having all that energy absorbed in a small pixel size of 50 μm is more unlikely when compared to the pixel size of 1 mm.

All the above simulations were conducted under the assumption of a 1 μm gap between the layers. We have simulated gap sizes ranging from 1 μm to 2 mm. We observed that increasing the gap for a 3-layer detector with 1 mm and 50 μm pixel sizes caused a small decrease in MTF, but only at very low spatial frequencies as shown in Fig. 3.8.

Moreover, detection efficiency in Fig. 3.9 for both pixel sizes shows a negligible decrease in the efficiency of the detectors.



(a) (b)

Figure 3.8: MTF for three layers with the gap between layers from $1\mu m$ to 2 mm. (a) 1 mm pixel pitch. (b) 50 μm pixel pitch

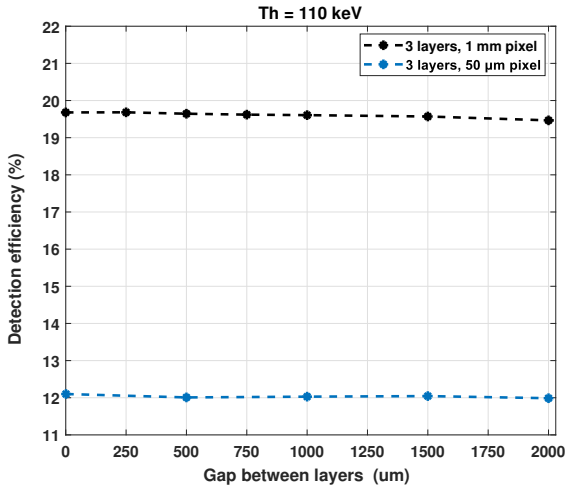


Figure 3.9: Detection efficiency for three layers with the gap between layers from $1\mu m$ to 2 mm.

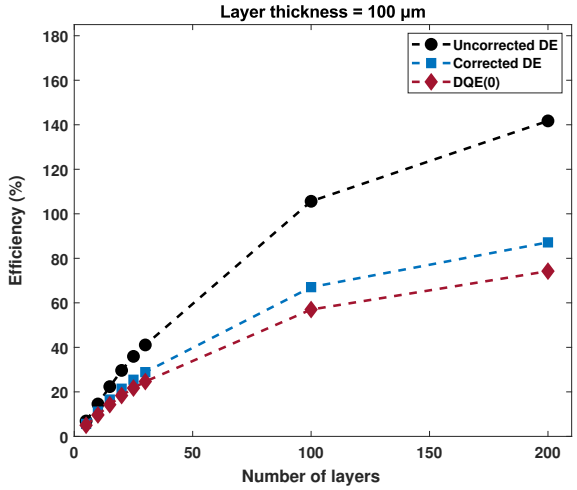


Figure 3.10: DQE(0), uncorrected DE, and corrected DE for the detector thickness of 0.1 mm and number of layers from 3 to 200. Uncorrected DE exceeds 100% due to the occurrence of multiple counts recorded for a single photon. For additional details, please refer to section 3.3.

To have a sense of DE and DQE(0) for the samples fabricated in the G2N lab, we

simulated the 1 mm pixel size with a-Se thickness of 0.1 mm. For this simulation, we used Thilo et al. method to correct DE and calculate DQE(0). As shown in Fig. 3.10, 30 detector layers have almost the same DE as 3 layers with 1 mm in Fig. 3.7. With this simple method, we were able to show DQE(0) for different numbers of layers indicating less than 10% for 3 layers of 0.1 mm thick detectors.

3.5 Conclusion

These results demonstrate that for a pixel size of 1mm, stacking a-Se based detectors to increase detection efficiency will not significantly degrade the spatial resolution of the system. The detection efficiency can be increased up to 80% for an energy threshold of 10 keV at the cost of spatial resolution and 52% for an energy threshold of 110 keV by using 10 layers. The latter reduces the noise counts caused by interlayer scattering. In addition, the $50\mu m$ pixel detector has lower detection efficiency for high energy thresholds, hence it needs more detector layers to be comparable with the 1mm pixel detector. In conclusion, the proposed a-Se detector can be a cost-effective solution for large area higher energy radiation imaging applications that can provide 1mm resolution with the potential to be used for sub-millimeter resolution. However, having more number of layers increases the readout complexity if we use conventional pixel architectures. The next chapter explores a novel readout method to incorporate with an a-Se detector that can reduce readout complexity for large-area radiation imaging applications.

Chapter 4

Charge division readout for large area radiation imaging

4.1 Introduction

Single Photon Emission Computed Tomography (SPECT), a crucial nuclear imaging technique for diagnostics and therapy decisions, utilizes radiotracers that emit gamma rays within the 140keV to 160keV energy range. The detection of these gamma rays occurs through a camera system composed of a collimator, scintillator, photomultiplier tube (PMT), and readout circuitry. However, the challenge stems from the radiotracer's emission of gamma rays in all directions, necessitating collimation to filter and accurately locate the photons. The subsequent conversion process transforms gamma photons into optical photons within the scintillator, which are then converted into electrons by the PMT and amplified within a high electric field. This electrical signal is subsequently processed through readout circuits to generate data. Notably, SPECT encounters limitations in spatial resolution due to the scattering of optical photons within the scintillator material, while the use of PMTs introduces cost, size, and susceptibility concerns to magnetic fields. To address both spatial resolution, compactness, and magnetic field sensitivity, researchers have been investigating the implementation of direct conversion semiconductor based detectors as an alternative approach. A specific material of interest in this regard is Cadmium Zinc Telluride (CZT) [62, 63, 64]. However, CZT comes with its own set of limitations, stemming from restricted production capacity and resource-intensive manufacturing processes, making it less suitable for larger-scale imaging applications. An alternative solution is the utilization of amorphous selenium (a-Se), a semiconductor material with promising

potential to alleviate these issues and enhance the overall performance of SPECT imaging.

Amorphous selenium (a-Se) is widely used in large flat panel detectors for X-ray imaging due to its ability to create clear images and its cost-effective manufacturing process suitable for large areas. However, a-Se has a limitation in terms of its ability to stop high-energy radiation effectively, primarily because it has a low atomic number (Z=34). This makes it less practical for tasks involving high-energy radiation, like Single Photon Emission Computed Tomography (SPECT). To overcome this limitation, in the previous chapter, our design approach involved stacking multiple detectors to increase the stopping power in radiation detection. Each detector layer consisted of sublayers such as the photoconductor, hole blocking layer, top and bottom electrodes, and readout circuit. This design allowed for improved detection efficiency, bringing the detector on par with commercially available SPECT detectors. However, it introduced higher complexity in the readout circuit design from both a yield and cost perspective, posing a challenge to overcome.

To address the readout issue, we explore a simpler array readout architecture based on a position-sensitive detector (PSD). PSDs operate based on the principle of converting the position of the incident radiation or particles into an electrical signal. PSDs offer two main types of readout: continuous or segmented.

In the continuous readout, a resistive sheet is deposited on top of the photoconductor. A light spot present on the active area generates a photocurrent, which flows from the point of incidence through a resistive layer to the contacts at the corners or sides to determine the precise location of impinging photons. Therefore, continuous readout PSDs provide a direct readout of a light spot displacement across the entire active area. On the other hand, segmented readout consists of common substrate photodiodes divided into either two or four segments (for one or two-dimensional measurements, respectively), separated by a gap or dead region. The relative position is obtained by simply measuring the output current of each segment.

Microstrips and pixels can be integrated into PSDs to enhance their functionality and performance. Microstrips can be used as the segmented readout elements in PSDs, dividing the detector surface into multiple microstrips, each providing position information based on the output current it generates. Pixels, on the other hand, create pixelated detectors, where each pixel detects the interaction of radiation or particles in a specific location, providing high spatial resolution and detailed imaging capabilities. Hybrid methods have also been explored, having both a resistive layer and metal microstrips at the top. This hybrid approach enhances the resolution of position sensitivity when photons impinge between the microstrips [65]. Another hybrid method involves an array of resistive microstrips, providing segmented lateral position outputs and continuous longitudinal position estimation

through charge division [66, 67].

Resistive electrodes have long been employed for precise position sensing in nuclear particle and radiation detectors, and two distinct methods have emerged for implementing this technology, charge division and rise time, each with unique practical aspects. In the

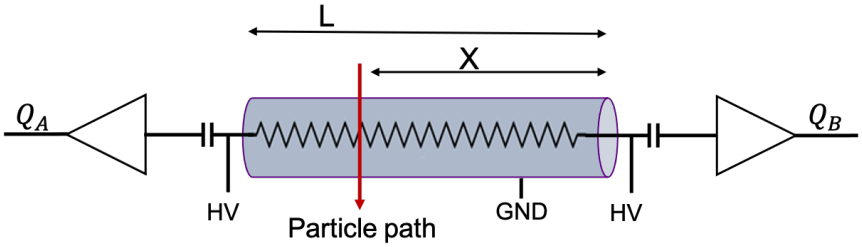


Figure 4.1: fabricated device with wires attached to bonding pads using silver paste.

charge division method as shown in Fig. 4.1, the position is determined by comparing the charge flowing out of one end of the resistive electrode to the total charge as follows,

$$X = \frac{Q_A}{Q_A + Q_B} L \tag{4.1}$$

On the other hand, the rise time method utilizes the diffusion time of the signal from the point of charge injection to the time the charge reaches the end of the resistive electrode, treating it as part of an infinite diffusive line when terminated into its characteristic impedance.

The resistive charge division method has historically been employed in gaseous detectors and has been gradually adopted in semiconductor detectors as well. The characteristics of charge division in resistive microstrips were first reported by Radeka in 1974, and the key finding was that the resolution of position measurements does not depend on the resistance for relevant shaping time [68]. The best resolution achieved by only considering resistor noise is

$$\frac{\Delta l}{l} = 2.54 \frac{(kTC_D)^{1/2}}{Q_S}, \tag{4.2}$$

where l is the electrode length, C_D is the total detector capacitance, Q_S is the total signal charge, k is Boltzmann constant, and T is the temperature. This equation suggests that the spatial resolution depends on detector capacitance and input signal, so resistor value shouldn't have any effect on the resolution. However, the resistor value plays a crucial role in ensuring that the readout time constant is less than the detector charge collection time.

Moreover, other studies, such as the research carried out by Bassignana et al., demonstrated the potential of resistive silicon microstrip detectors in collider applications [69]. Building upon these foundations, our research explores the utilization of resistive microstrips on amorphous semiconductors, with a specific focus on a-Se. This marks the first instance of applying resistive microstrips in this context, representing an innovative approach to radiation detection technology.

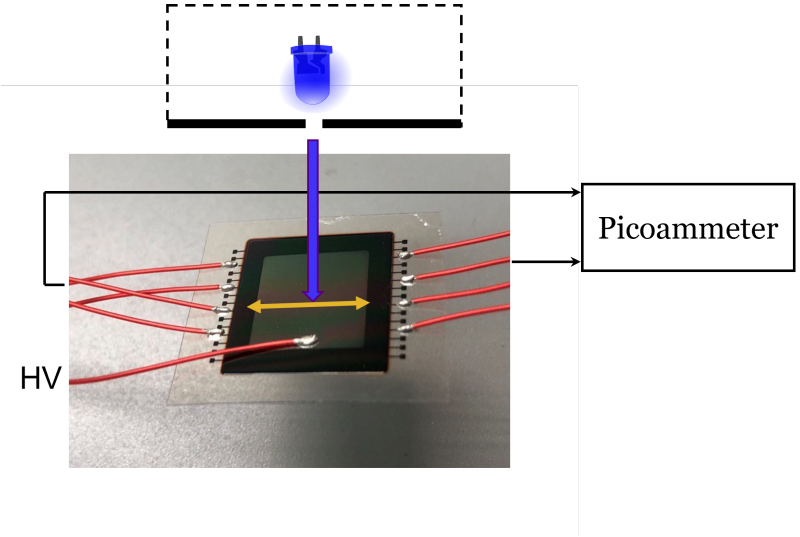
In this chapter[1] , we present a comprehensive investigation into the implementation of resistive microstrips on a-Se. Our research introduces a proof-of-concept device and outlines the carefully designed layout of the microstrips. The arrangement is strategically optimized to facilitate efficient charge division and precise localization of incoming photons. Additionally, we have conducted measurements on one of the electrodes to evaluate the performance of the resistive microstrip readout. By leveraging the charge division through the resistive electrode, we accurately locate the incoming photons. Furthermore, we investigate the linearity of longitudinal position for a radiation detector based on an amorphous semiconductor, a-Se. This analysis enables us to assess the reliability and linearity characteristics of our resistive microstrip readout approach in the context of amorphous semiconductors.

4.2 Experimental method

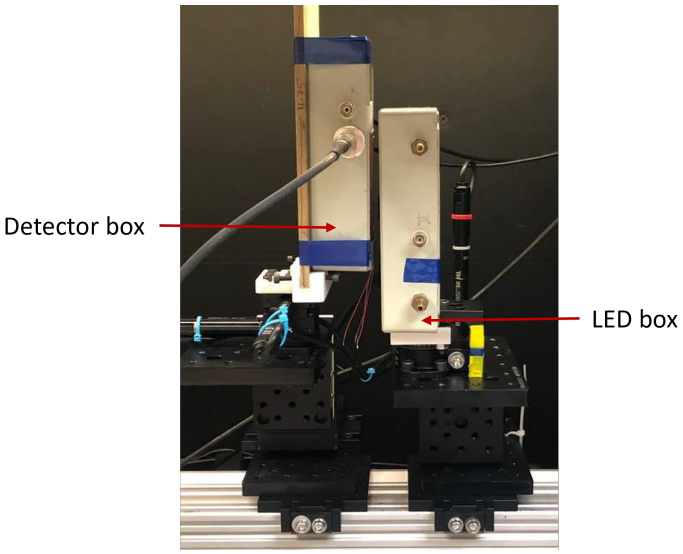
To investigate the position detection accuracy, the setup shown in Fig. 4.2 was used. A blue LED with a wavelength of 470 nm followed by a metal collimator with an aperture of 400 μm was used to create a beam with a focal spot of approximately 1 mm on the detector. Both the LED and detector boxes were mounted on motorized stages to control the lateral and vertical positions. However, due to the susceptibility of the detector readouts to motion, only the light source stage was used to sweep across the detector. Three connections were established with the detector box. The first connection involved applying /gls*hv across the a-Se photoconductor using SRS PS365 to create an electric field, effectively separating electron-hole pairs. The remaining two connections were dedicated to signal reading and current measurement at both ends of the indium tin oxide (ITO) electrodes, accomplished through the utilization of a Keithley 6482 dual-channel picoammeter.

Due to a slight mismatch between both channels, a fixed current was passed through the resistive microstrip from one channel to the other. This was then used to correct the current to obtain the photo response of the detector. Additionally, the dark current was

[1]Parts of this chapter have been published in [70, 71]



(a)



(b)

Figure 4.2: Experiment setup (a) model (b) assembeled on motorized stages.

divided between the two channels. As a result, the total read current for each channel is

$$I_{\mathrm{Ch1}} = I_{\mathrm{Ph1}} + I_{\mathrm{Dark}}/2 + I_{\mathrm{R}}, \tag{4.3}$$

$$I_{\mathrm{Ch2}} = I_{\mathrm{Ph2}} + I_{\mathrm{Dark}}/2 - I_{\mathrm{R}}, \tag{4.4}$$

where I_{Ph1} and I_{Ph2} are the photo current read by channel 1 and channel 2, respectively. I_{R} is the constant current due to the mismatch between the channels, and I_{Dark} is the total dark current read by only having one end of the electrode connected to the picoammeter. From the equation 4.3 and 4.4, dark current and mismatch current can be obtained in dark condition, i.e., $I_{\mathrm{Ph1}} = I_{\mathrm{Ph2}} = 0$, as follow

$$I_{\mathrm{Dark}} = I_{\mathrm{Ch1}} + I_{Ch2}, \tag{4.5}$$

$$I_{\mathrm{R}} = (I_{\mathrm{Ch1}} - I_{\mathrm{Ch2}})/2. \tag{4.6}$$

Using the measurements done in the dark and in the presence of LED illumination, photocurrent can be calculated and one can show via the charge division method that the location of incident photon relative to channel 2 is

$$X = \frac{I_{\mathrm{Ph1}}}{I_{\mathrm{Ph1}} + I_{\mathrm{Ph2}}} L, \tag{4.7}$$

where L is the length of the microstrip.

4.3 Microstrip fabrication

In order to implement the resistive microstrips for a-Se photoconductors, certain considerations need to be taken into account. Firstly, these microstrips should be biased at zero (i.e. virtual zero) and connected to the amplifiers, serving as the negative electrode. As mentioned earlier, the primary reason for dark current in a-Se is the injection of holes from the positive electrode, making it essential to incorporate a hole-blocking layer. Extensive investigations have revealed that PI (polyimide) is one of the most effective hole-blocking layers. However, it requires a high curing temperature and should be applied prior to the deposition of a-Se to prevent crystallization in a-Se structure.

This implies that the positive electrode should be positioned at the bottom, while the microstrips should be situated on the top surface of the a-Se photoconductor. To ensure a minimum spatial resolution of 1 mm, the microstrips should be spaced 1 mm apart from each other. Consequently, the width of the electrodes should fall within the micron range, such as 100 μm. Achieving such dimensions necessitates the use of lithography on a-Se. However, it is important to note that a-Se is highly sensitive to wet processes, and therefore, wet lithography should be avoided.

To overcome this challenge and fabricate a device without lithography, a shadow mask was used for depositing the microstrips. However, conventional methods of constructing

metal shadow masks are not suitable due to the small openings, which limit the mask's thickness. Consequently, we employed a shadow mask provided by Shimifrez Inc., which was fabricated using 20 μm thick nickel and enabled us to achieve a minimum feature size of 35 microns. As shown in Fig. 4.3 it was important to handle the fragile mask with care to prevent it from buckling or sustaining damage during the fabrication process. The top microstrip design was the first fabricated device using this mask and eventually, we tested the bottom electrode design which will be explained in the next sections.

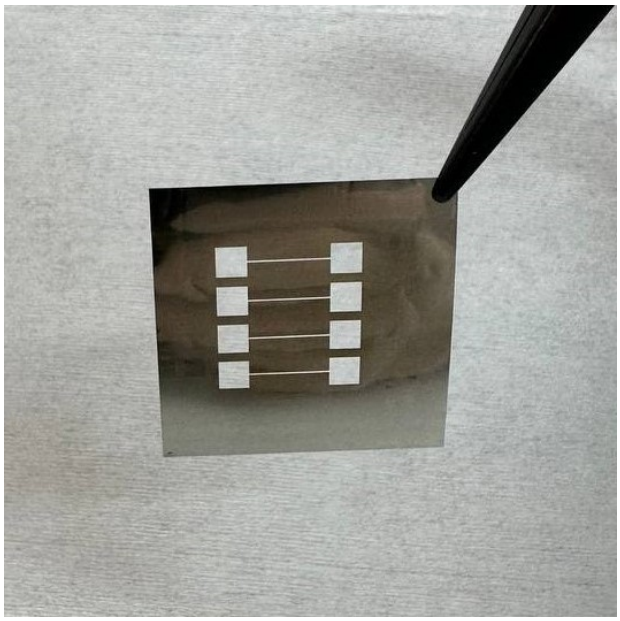


Figure 4.3: Shadow mask for top microstrip design.

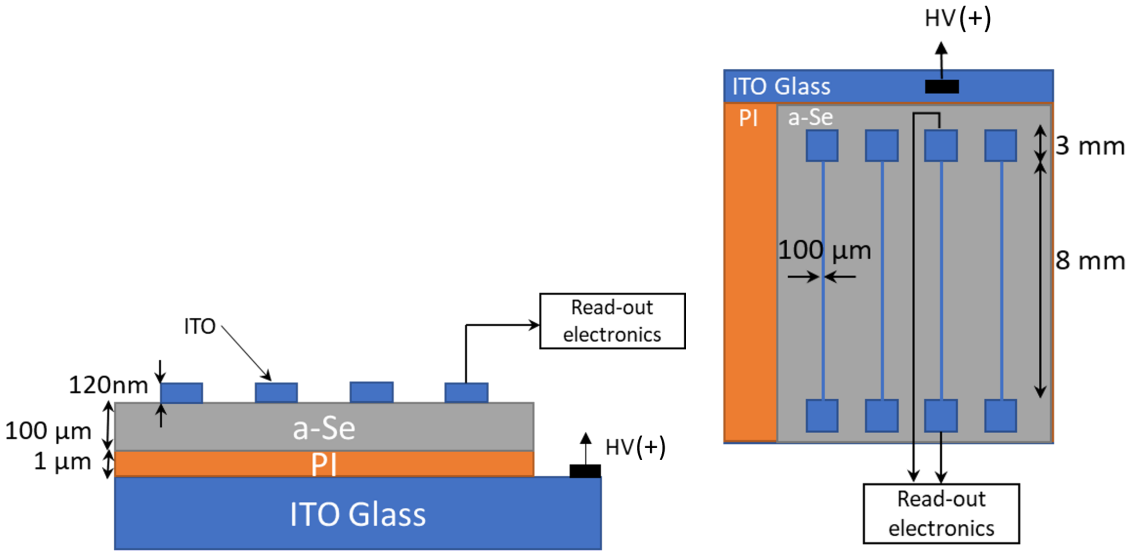
4.4 Top microstrip design

This design consists of a stabilized a-Se layer positioned between resistive top electrodes (ITO) and a polyimide (PI) hole-blocking layer to cover the bottom electrode (the ITO glass substrate). The 1 μm PI layer was spin-coated on the ITO glass substrate, then 100 μm a-Se containing 0.5% arsenic (As) and 8-ppm chlorine (Cl) was thermally evaporated on the device. A microstrip structure was used for the top electrodes as illustrated in Fig. 4.4. The microstrips are 100 μm wide, 120 nm thick, and 8 mm long with bonding pads at both ends (3 mm $\times$ 3 mm). These resistive ITO electrodes were deposited through an E-beam

evaporation process using the designed shadow mask in Fig. 4.3. The resistivity of the top electrodes was controllable by changing the thickness and width of the microstrips.

To implement the charge division method effectively, it is necessary to read out both ends of the microstrip and ensure that the microstrip resistance R_D is significantly higher than the amplifier input impedance, which typically falls within the range of 10Ω to $10^3\Omega$. The measured resistance of one electrode was approximately 205 kΩ (2.510 kΩ/square) significantly exceeding the amplifier's input impedance. The longitudinal resolution according to equation 4.2remains unaffected. Additionally, this resistance value is sufficiently low to maintain a short rise time, preventing any undesirable signal broadening. Consequently, the microstrip is well-suited for effectively dividing the induced charges resulting from impinged photons.

Moreover, to minimize noise, it is essential to keep the capacitor size small. The capacitance across the detector was measured using a CV analyzer with a series model, yielding a value of 8.35 pF at 1 MHz. These measurements closely agree with the capacitance calculated using the parallel plate capacitor formula, considering the geometric parameters for the area ($A = 18.8mm^2$), distance ($d = 0.1mm$), and relative permittivity ($k \approx 6$ for a-Se), resulting in a calculated capacitance of 9.98 pF. Consequently, the time constant of the detector microstrip is determined to be $1.71\mu s$, a value that is smaller than the charge collection time in the a-Se photoconductor (approximately $40\mu s$).



(a) (b)

Figure 4.4: Illustration of (a) side view of the detector structure, (b) top view of detector structure showing both ends of restive electrodes

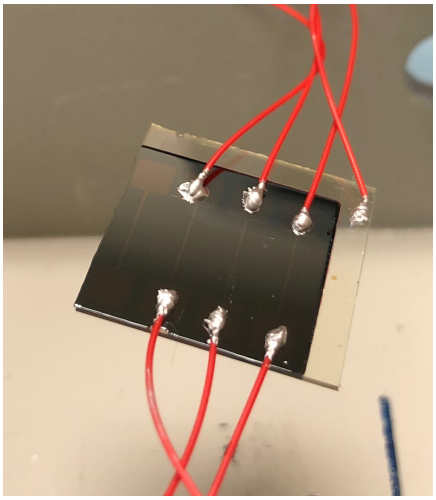
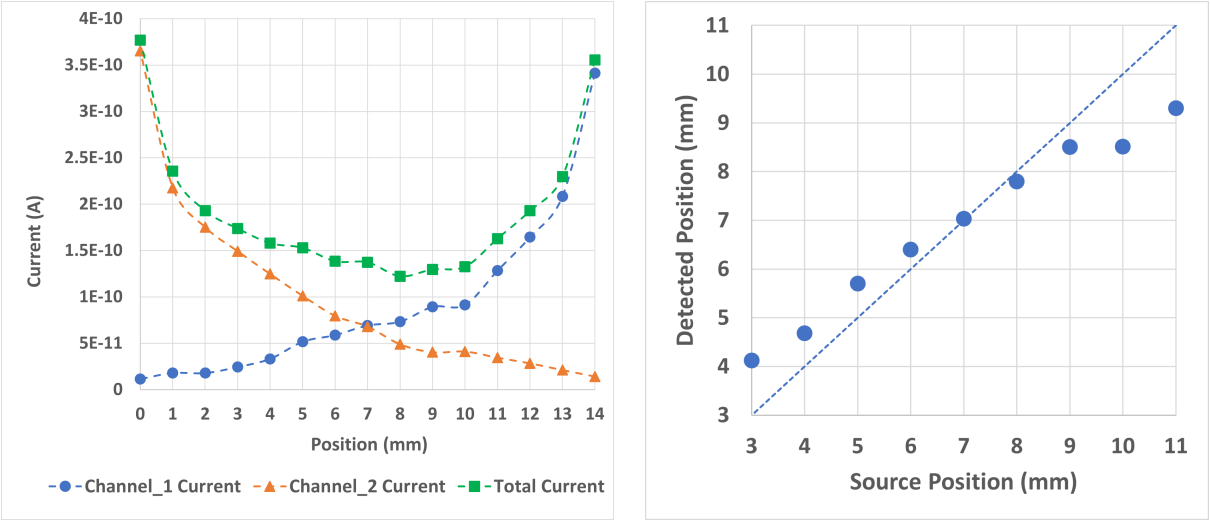


Figure 4.5: fabricated device with wires attached to bonding pads using silver paste.

4.4.1 Results

The dark current measurement for an individual electrode, under 6 V/μm and after one hour resting condition, resulted in 85 fA/mm^2 which is sufficiently low. The PI layer reduced the dark current by blocking hole injections from the positive electrode (the ITO glass here) [56]. However, after illuminating the detector, trapped charges and slow carriers cause a drift in the dark current. Therefore, another short dark current measurement was carried out between illuminations, and a dark correction was applied later to obtain the photocurrents.

The LED stage was swept over the detector from the beginning of one of the bonding pads of the electrode to the end of the other pad, which is 14 mm in total. As shown in Fig. 4.2 the total current near the pads (0 mm to 3 mm, and 11 mm to 14 mm) is increasing abruptly. This is because the pads cover a larger area of the detector compared to the microstrips. Moreover, the light absorbed in the middle is going through more broadening compared to the case where it is absorbed near the ends.



(a) (b)

Figure 4.6: (a) The photocurrents read from the two ends of a single electrode after dark current correction versus the position of the light source. (b) Detected position from the charge division equation along the electrode versus the actual position of the light source.

To retrieve the position from resistive electrodes, the charge division mechanism can be utilized such that the ratio of the current channel 1 to the total current multiplied by

the length of the microstrip provides us with the position of the light source relative to the current channel 2. Since the signals from the pad areas are not linear and are affected by a large active area beneath them, the position was calculated for microstrips between pads, which is illustrated in Fig. 4.10(b). Fig. 4.10(b) shows that the detected position by the read currents versus the real position of the light source is semi-linear with a good approximation. The results demonstrate the feasibility of detecting the position of a light source with a resolution of 1 mm. Although a slight non-linear behavior is noticeable in the findings, it can be effectively addressed using a calibration technique, such as a correction table, to accurately determine the precise position of the light source. Alternatively, a more effective approach involves modifying the detector's structure to position the microstrips at the bottom, leading to an enhanced spatial resolution and linearity. This structural adjustment reduces the detector capacitance since the pads are located outside the active area. Further exploration and analysis of this design are discussed in the following section.

4.5 Bottom microstrip design

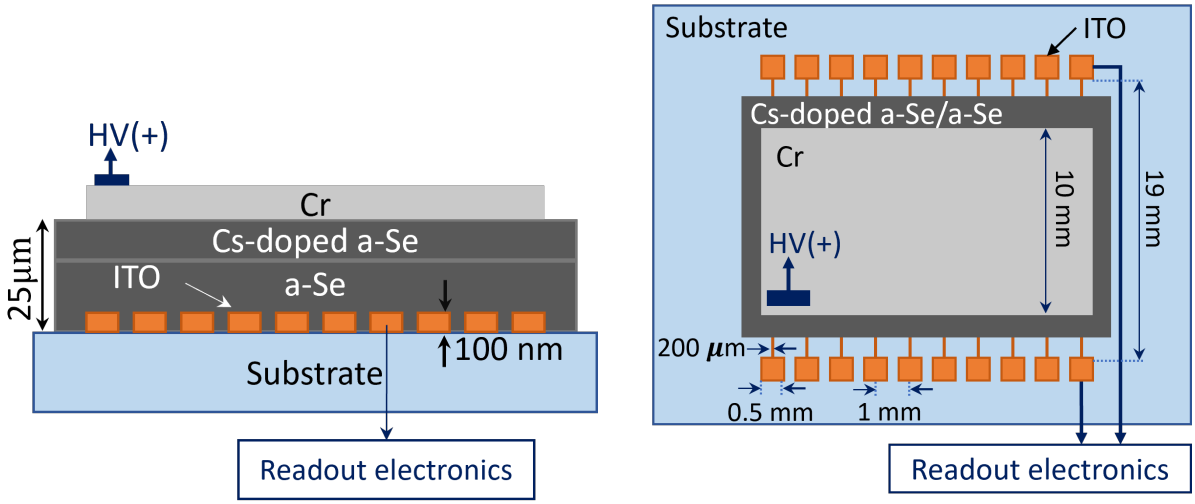


Figure 4.7: Illustration of the (a) side (b) top view of the detector structure.

Fabrication of the bottom microstrip design starts with defining the bottom electrode. To employ charge division readout, ITO was used as a resistive microstrip at the bottom of

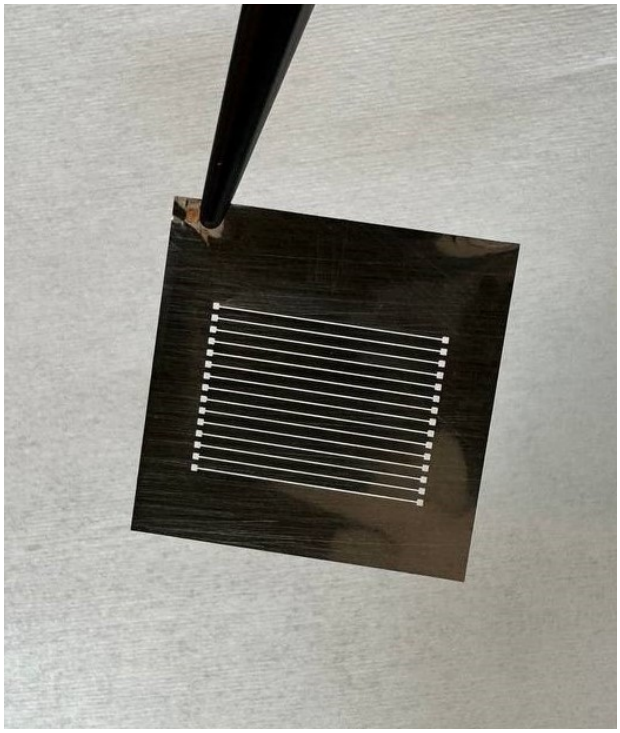


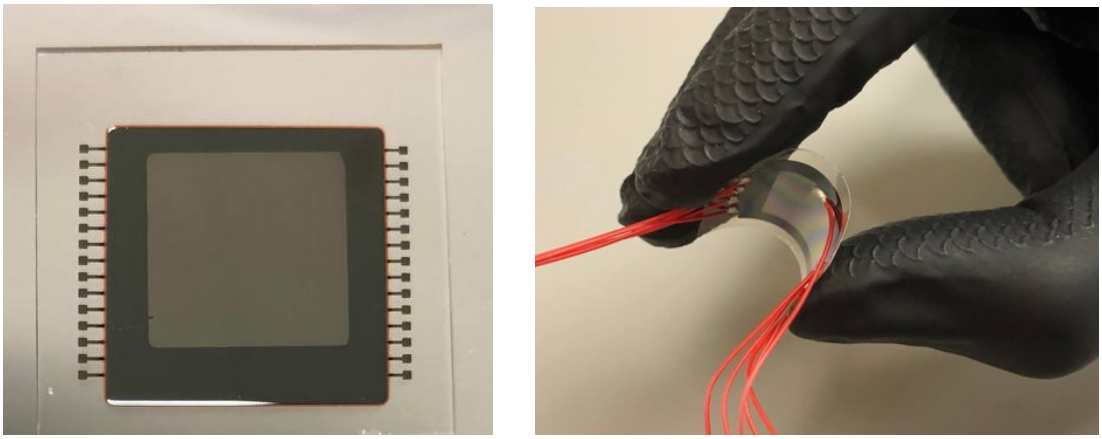
Figure 4.8: Shadow mask for bottom microstrip design.

the structure, and it was deposited on a glass substrate using a shadow mask shown in Fig. 4.8 through E-beam evaporation. The width, length, and thickness of the microstrips are 200 μm, 19 mm, and 100 nm, respectively. These dimensions were chosen to have an electrode with a resistance of approximately 242 $k\Omega$ (12.7 $k\Omega$/mm). Then, the stabilized a-Se containing 0.5% arsenic (As) and 8-ppm chlorine (Cl) was thermally evaporated on the bottom electrodes. Prior to depositing the top metal contact, the inclusion of a hole-blocking layer, such as polyimide (PI), becomes essential to minimize the dark current. Despite PI having demonstrated a substantial reduction in dark current in conventional a-Se detectors[56], it is not a suitable candidate for our proposed design. In our design, the hole-blocking layer should be used between a-Se and the top positive electrode. If PI is used as the hole-blocking layer, it requires high temperatures to be cured, which in turn crystallizes a-Se and changes its electrical properties. Thus, a 9μm Cs-doped and As-stabilized a-Se, instead of a PI layer, was thermally evaporated on the 16μm a-Se layer to lower the dark current. Cs doped a-Se is an n-type material with a substantial density of hole traps, which suppresses the dark current. Finally, a thin layer of chromium (Cr) was deposited for the top electrode through E-beam evaporation.

The capacitance across the detector was measured using a CV analyzer employing a series model, yielding a value of 3.06 pF at 1 MHz. These measurements closely align with the capacitance calculated using the capacitor formula, accounting for the geometric parameters of the area ($A = 9mm^2$), distance ($d = 0.025mm$), and relative permittivity ($k \approx 6$ for a-Se), resulting in a calculated capacitance of 4.25 pF.

It is noteworthy that, despite the reduced thickness of selenium in the current design, the capacitance is approximately half of the previous design. This observation indicates that the relocation of the readout pad from the active area significantly diminishes the capacitance. Based on the obtained measurements, the time constant of the detector microstrip is determined to be $0.74\mu s$, which again is much smaller than the charge collection time in the a-Se photoconductor

Two devices were fabricated with two different substrates: glass and polyethylene terephthalate (PET), which are shown in Fig. 4.9. There are many advantages in using a large-area flexible detector including its cost-effectiveness, robustness, and its ability to be fitted into curved structures to avoid detector tiling around the body and being utilized in mobile systems. Therefore, the focus of this work is on the characterization of a flexible detector, which will be presented in the following section.

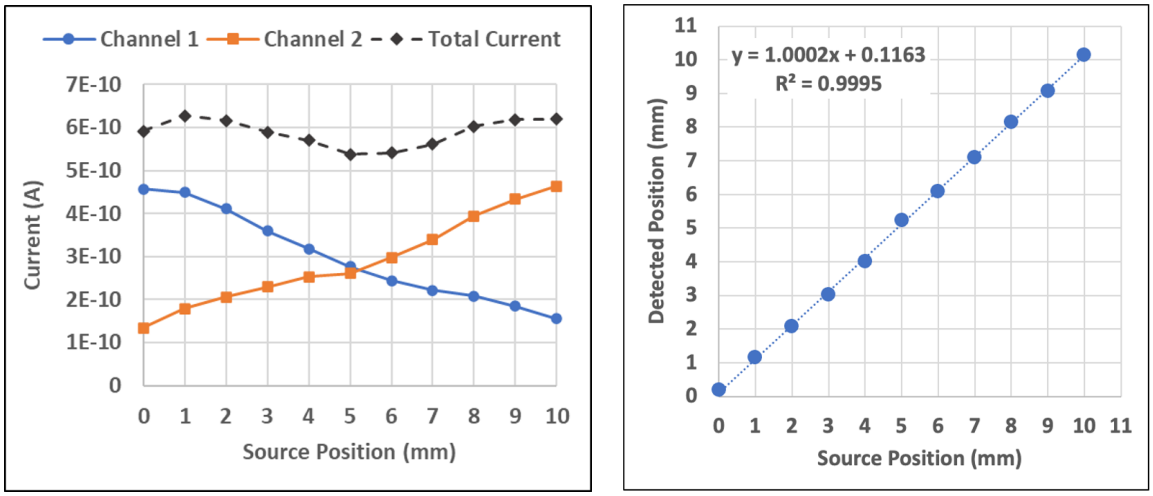


(a) (b)

Figure 4.9: Fabricated device on (a) glass (b) PET substrate.

4.5.1 Results

The measured total dark current after 2 hours rest was 20 pA/mm^2. In comparison to the top microstrip design, the dark current exhibited a higher level due to the less effective performance of the n-type a-Se in comparison to the PI hole-blocking layer. Consequently, a comprehensive exploration is required to identify an appropriate hole-blocking layer that can be employed over the a-Se surface, and this aspect will be discussed in detail in the upcoming chapter. For photocurrent measurement, the LED stage was swept over the detector with 1mm steps from the beginning of the active area shown in Fig. 4.2b. The active area here is the overlap of Cr thin film and the electrode. Before each photocurrent measurement, a dark measurement was done to update the dark current value, affected by radiation, and the mismatch current using equation 4.4. These values were used in the offset correction of read current from channels to extract the photocurrents ($I_{\mathrm{Ph1}}, and I_{\mathrm{Ph2}}$) according to equation 4.3 to 4.6. The total photocurrent and photocurrent of each channel are plotted in Fig. 4.2a. The total current fluctuates at the middle but stays within the same range for the whole length of the active area. This fluctuation at the middle is the result of signal broadening since most of the charges, generated at the middle, have to travel a longer distance in total. electrodes.



(a) (b)

Figure 4.10: (a) The photocurrents read from the two ends of a single electrode after dark current correction versus the position of the light source. (b) Detected position from the charge division equation along the electrode versus the physical location of the light source.

The relative position of incident light was calculated based on equation 4.7. Then, this relative position was normalized to have position $X = 0$ referenced to the beginning of the active area which is 10mm long. Fig. 4.2b shows that the detected position is linear with respect to the position of the light source. Thus, this structure has the potential for precise localization of absorbed photons and exhibits superior performance when compared to the top microstrip design.

4.6 Conclusion

This chapter was focused on investigating the dark current and photoresponse of charge division electrodes for a-Se detectors, and our findings confirm the feasibility of accurately detecting the position of a light source with a 1 mm resolution, typical in SPECT systems. To address the slight non-linear behavior observed in the original top microstrip design, a strategic relocation of the microstrips to the bottom was implemented. Furthermore, the bottom microstrip design was tested to assess the linearity of the position-sensing microstrip a-Se detector on a flexible substrate, and the results demonstrated a consistent spatial resolution of 1 mm across the entire active area, accompanied by a linear response. Therefore, his modification resulted in a significantly improved linearity in the position-sensing capabilities of the a-Se detector. The adoption of this approach not only simplifies the complexity of the readout circuit but also capitalizes on the benefits offered by mechanically flexible substrates, thereby opening up possibilities for realizing large-area curved multi-layer detectors, specially tailored for high-energy radiation imaging applications.

Chapter 5

Optimization of Hole Blocking Layer

5.1 Introduction

In the previous chapter, we extensively explored charge division readout techniques employed in a-Se detectors to reduce readout complexity for the multilayer detector design introduced in chapter 3. Our findings demonstrated its effectiveness in accurately locating the blue LED source, achieving a spatial resolution of 1 mm. However, when it comes to detecting individual photons for photon counting applications, we require a detector that has very little background noise and a high on/off current ratio. This is due to the extremely weak signal generated by a single photon. The resistive electrode itself introduces some amount of thermal noise into the system, therefore it is crucial to manage other sources of background signals, such as sensor dark current.

Reducing dark current is a significant factor in achieving accurate photon detection. As we consider the use of the bottom microstrip design, where the hole-blocking layer needs to be on top, we recognize the critical role of this layer's placement. A preliminary measurement (not shown) indicated that using Cs-doped selenium as a top hole blocking contact had limitations in controlling dark current and the detector was unable to effectively detect single photons. In response, this chapter[1] introduces a new hole-blocking layer to be used on the top surface of a-Se photoconductor. Using the proper top hole blocking layer not only helps the detection of photons in our design but also advances detector development in conventional X-ray imaging applications using direct conversion semiconductors.

[1]Parts of this chapter have been published in [72]

The demand for X-ray detectors with excellent temporal response and low-dose capabilities has become increasingly prominent with the emergence of dynamic mammography tomosynthesis. This innovative quasi-3D medical imaging technique has surpassed the capabilities of traditional 2D mammography. For many years, a-Se has stood out as a preferred option in this domain due to its well-established manufacturing process and its suitability for use in large-area applications. Its high spatial resolution is optimal for detecting small micro-calcifications, which are indicative of breast cancer, making it an ideal choice. [73]. Achieving high sensitivity in low-dose scenarios necessitates the increase of bias voltage across the selenium photoconductor, resulting in a higher dark current. These applications, namely our design with bottom microstrips and dynamic mammography tomosynthesis, inspired us to delve into the search for an appropriate hole-blocking contact.

The dark current observed in a-Se detectors is attributed to the injection of holes at the interface of the positive electrode [74, 75]. To tackle this problem, several investigations have explored different hole-blocking layers, among which Polyimide (PI) has exhibited superior capabilities compared to other materials [76]. However, the 350°C curing temperature of PI imposes a constraint that confines its application solely to the bottom hole-blocking layer in the a-Se structure since the curing temperature of PI exceeds the melting point of a-Se. In addition, for certain applications, such as those involving complementary metal-oxide-semiconductor (CMOS) or our design with resistive microstrips [71], the readout is located at the bottom of the structure, and employing PI as the hole-blocking layer mandates the placement of the positive electrode at the bottom. The bottom surface configuration causes the selenium detector to function in an electron mode and poor temporal performance due to a-Se's low electron mobility. For superior performance in hole-collecting mode, it becomes essential to position the positive electrode on the top surface of the a-Se photoconductor while incorporating a hole-blocking layer with a lower curing temperature.

Several alternative hole-blocking layers have been evaluated on the top surface of a-Se photoconducting layer, including ultrathin films of Cerium oxide (CeO2), colloidal quantum dots (QDs), and PTCBI [76, 77, 78]. CeO2 is an n-type material that can prevent hole injection by creating a potential barrier to holes, but deviations from stoichiometry make the fabrication process complex. Although high-temperature processes can overcome this issue, it makes CeO2 unsuitable for depositing onto a-Se. While QDs offer a low-temperature alternative to CeO2, they still suffer from fabrication complexity due to maintaining precise stoichiometry. On the other hand, PTCBI is a relatively low-cost organic alternative with simple solution-based deposition methods; however, it suffers from poor adhesion to the a-Se layer leading to reliability concerns.

In this chapter, we investigated the potential of SU-8, a widely available low-temperature

spin-coated organic material as a hole-blocking layer for selenium. SU-8 is commonly used as a photoresist in MEMS applications, and it can also remain in the structure as a carrier or encapsulation layer. In the past, SU-8 was used as an intra-layer in a multi-layer contact for solar cells to improve power conversion efficiency[79]. Since SU-8 can be cured at varying temperatures, it can be employed on the top surface of a-Se, and its spin-coating process offers a cost-effective and scalable approach for large-area X-ray detector fabrication. To assess SU-8 as a hole-blocking layer, a-Se detectors with the SU-8 hole-blocking layer on both sides of a-Se were fabricated in-house and characterized. Subsequently, a novel bilayer hole blocking contact, comprising SU-8 and Cs doped a-Se, was fabricated and characterized

5.2 Experimental Methods

The Keithley 6482 picoammeter was utilized to measure the dark current over a span of 20 minutes, maintaining a constant electric field until it reached a stable plateau. The values reported in this chapter are indicative of the average readings from this plateau phase. To ensure consistent outcomes, all samples were rested for two hours in the dark and short-circuited between different applied fields, enabling the release of trapped charge carriers. Following each dark current measurement, the photocurrent was recorded using the same setup with Keithley 6482 to quantify the current. Since a-Se is most sensitive to blue light, a 468 nm wavelength LED controlled by a function generator was utilized for this optical testing. The LED operated in a pulse mode, with a period of 21 seconds and 7 seconds during which it was active.

Pulsed X-rays were utilized to assess the temporal characteristics of the samples by quantifying ghosting and lag. Lag, known as persistent photoconductivity (PPC), denotes the residual signal in the X-ray detector post-exposure while ghosting, or priming, signifies changes in detector sensitivity due to prior X-ray exposure [56]. In order to mitigate the influence of trapped charges on the results, the samples were subjected to a resting period of over 12 hours in a dark, short-circuited condition prior to the experiment. Pulsed X-rays are commonly used in applications like mammography and fluoroscopy to minimize motion artifacts and reduce patient radiation exposure, typically operating at frame rates ranging from 1 to 30 frames per second, accompanied by a 50% duty cycle[80]. In this context, interrupting the exposure becomes essential for the measurement of lag and the assessment of potential sensitivity fluctuations. Notably, a longer rest time between pulses tends to result in a better temporal response.

The X-ray experimental setup employed the Varian G-1582TRI B-180H X-ray tube,

driven by the EMD Epsilon EPS45-80 X-ray generator. The X-ray source was configured to produce 10 pulses per second, with each pulse lasting for 50 milliseconds at 75 kV_p and 200 mA. The samples underwent a sequence of 20 exposures, each lasting for 1 second, with 60-second intervals for resetting between consecutive exposures. To achieve uniform absorption across the selenium material, a 5 mm thick aluminum sheet was utilized to harden the X-ray beam. Additionally, each exposure delivered to the detector, post-Al filtration, corresponded to a dose of 8.76 mGy measured by a Solidose 300 dosimeter. The detector side featuring the hole-blocking layer, positioned either at the top or bottom, was positively biased, while the opposite side was connected to a current amplifier (Keithley 427) to visualize the signal on an oscilloscope. This arrangement ensured consistent hole collection in the readout, maintaining optimal temporal performance throughout all measurements.

The detector's response (R) is determined by calculating the difference between the output current of the detector during X-ray exposure and the increased dark current due to an increase in charge injection. To simplify the comparison, assuming that the entire input dose is absorbed during the first exposure results in a 100% sensitivity (S) for that initial exposure. We can then establish the sensitivities for subsequent exposures. Additionally, the calculations for lag and ghosting can be outlined as follows [56, 81]:

$$R_n = \langle I_{\text{Ph}} \rangle_n - \langle I_{\text{Dark}} \rangle_n \tag{5.1}$$

$$\text{Assume} \quad S_1 = \frac{R_1}{D_{\text{input}}} * 100 = 100\% \quad \Rightarrow \quad R_1 = D_{\text{input}} \tag{5.2}$$

$$S_n = \frac{R_n}{D_{\text{input}}} = \frac{R_n}{R_1} \tag{5.3}$$

$$\text{Lag}_n = \frac{\langle I_{\text{Dark}} \rangle_n - I_{\text{Rest}n}}{R_n} \tag{5.4}$$

$$\text{Ghosting}_n = \frac{R_n}{R_1} \tag{5.5}$$

where n is the X-ray exposure number and I_{Rest}, $\langle I_{Dark} \rangle$, and $\langle I_{Ph} \rangle$ are shown in Fig. 5.4.

5.3 SU-8 hole-blocking layer

The SU-8 used in this chapter is SU-8 3000. SU-8 3000 which is an epoxy-based photoresist, excels in micromachining and microelectronic applications. It improves on its predecessors, offering enhanced adhesion and reduced coating stress. With excellent optical transmission above 360 nm, it is ideal for imaging vertical sidewalls in thick films. Best suited for permanent applications, it ensures long-lasting, precise microstructures.

Four different samples were fabricated to investigate the impact of SU-8 on the entire structure. In all four samples, the substrate was ITO on glass that underwent a cleaning process in an ultrasonication bath of acetone and isopropyl alcohol. The top electrode consisted of a 60 nm chromium (Cr) film followed by a 200 nm aluminum (Al) film deposited using an e-beam evaporation system. All four samples utilized a 16 μm a-Se layer that was thermally deposited from a stabilized selenium alloy containing 0.5% arsenic (As) and 8-ppm chlorine (Cl). One sample was used as a reference without any hole-blocking layer. The second sample had 1 μm spin-coated PI on the ITO film and was cured at 350°C. The remaining two samples had 0.5 μm SU-8 spin-coated film—one sample with the SU-8 layer on the bottom surface of the a-Se layer and one with the SU-8 layer on the top surface of the a-Se layer. The sample with the SU-8 at the bottom underwent a soft bake and a post-exposure bake at 95°C for 1 minute, followed by a hard bake at 150°C. The sample with the SU-8 at the top was not hard-baked and the soft bake and post-exposure bake for this sample were conducted at 55°C for 30 minutes to minimize the impact of temperature on a-Se.

5.3.1 Results

Dark current results are presented in Fig. 5.1. All samples had the same active area, and the current is presented as normalized by the device's active area. Electric fields reported were estimated by only taking into account the thickness of a-Se. At 40 V/μm, the dark current for SU-8 devices remains consistently below 1 pA/mm^2 thus demonstrating the performance of the SU-8 hole-blocking layer in suppressing the hole injection at the positive electrode interface.

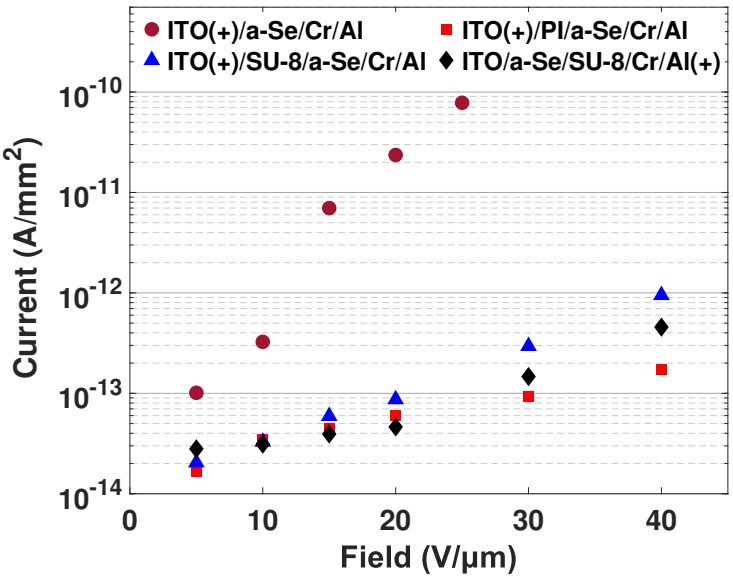


Figure 5.1: Dark current density of the a-Se detectors including reference device and those integrating PI and SU-8 hole-blocking layers as a function of electric fields. The reported values are the mean of the plateau achieved after maintaining a constant electric field for 20 minutes.

The photoresponse of the devices with and without a blocking layer for a light intensity of 110 $\mu W/cm^2$ is shown in Fig. 5.2. The photocurrent data is challenging to use in directly comparing devices biased from the top with those biased from the bottom. This is because irradiation consistently occurs from the ITO side (bottom), with immediate absorption upon entering the a-Se bulk. Consequently, the device with the positive electrode at the bottom experiences shorter electron travel distances and fewer instances of entrapment during the charge transport. Conversely, the device with the positive electrode at the top entails electrons traveling the entire distance upward and across the whole thickness of selenium, leading to signal entrapment. Since the device design is based on bipolar charge sensing, the electron pathway impacts the overall collected signal and results in a diminished signal level for devices featuring a positive electrode at the top.

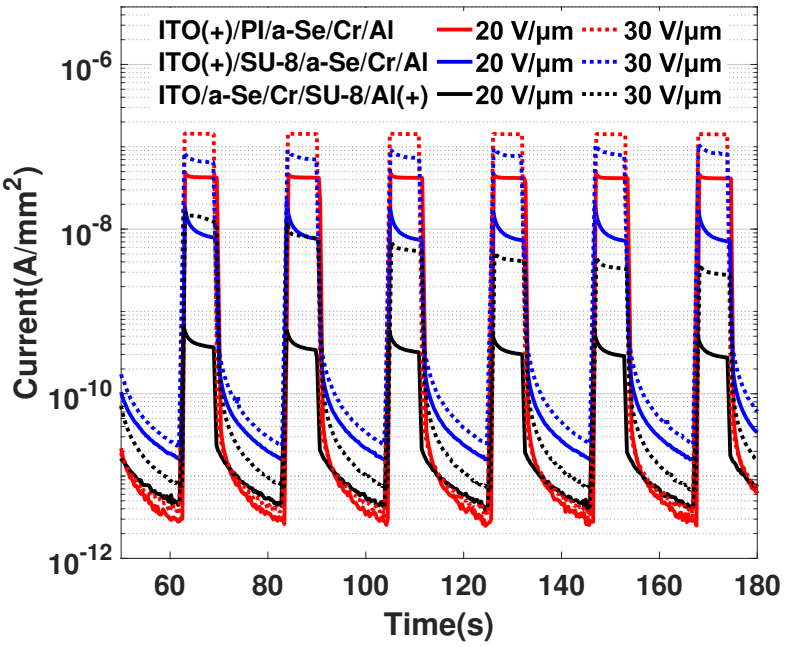


Figure 5.2: Photoresponse of a-Se detectors with PI and SU-8 hole-blocking layers to a blue LED with intensity of 110 $\mu W/cm^2$.

As illustrated in Fig. 5.2, structures featuring SU-8 on different sides of a-Se layer exhibit different signal levels. The discrepancy cannot simply be attributed to the voltage drop across SU-8, rather, it is likely related to charge transport and electron entrapment. It is noteworthy that the divergence in signal between the PI device and the SU-8 device indicates additional charge accumulation across the SU-8 layer. This was confirmed by the reduction in the signal gap between these two devices as voltage increases, implying that higher voltage mitigates charge buildup and increases charge detrapping.

To ensure an impartial assessment of device performance, X-ray measurements were conducted using a hardened X-ray beam to ensure consistency in measurements while the absorption of X-rays in the relatively thin blocking layers at the bottom side of the device was ignored. Again, all samples were irradiated from the ITO glass side as shown in Fig. 5.3 for one of the fabricated samples.

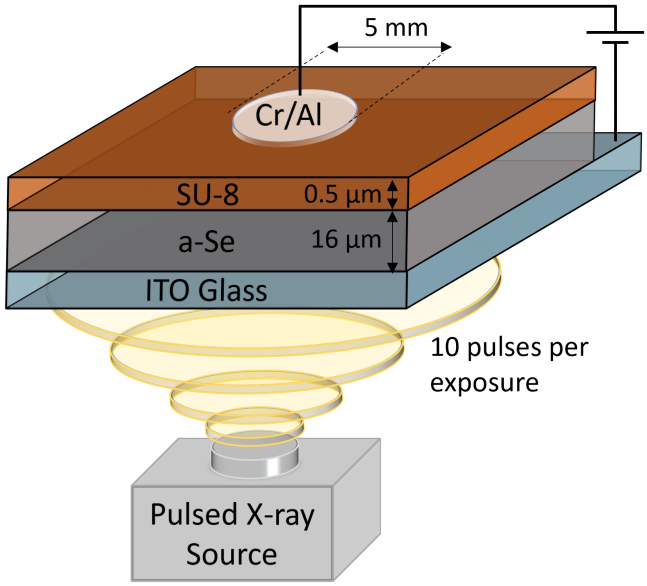


Figure 5.3: a-Se sample with SU-8 hole-blocking layer at the top exposed to pulsed X-ray to measure sensitivity and lag.

Fig. 5.4 represents the X-ray response of three devices that had hole-blocking layers, biased at 20 V/μm for the first and last exposure. The results indicate that the device with SU-8 at the top exhibited almost same signal level as the device with SU-8 at the bottom in the first exposure, while the device with PI exhibited lower signal levels compared to either SU-8 configuration. The last exposure also shows that the signal level of the PI device converges to match that of the device with SU-8 at the bottom. These differences and signal drops may be due to challenges in precisely aligning the device during illumination, different trap profiles at the interface, and a higher voltage drop across PI.

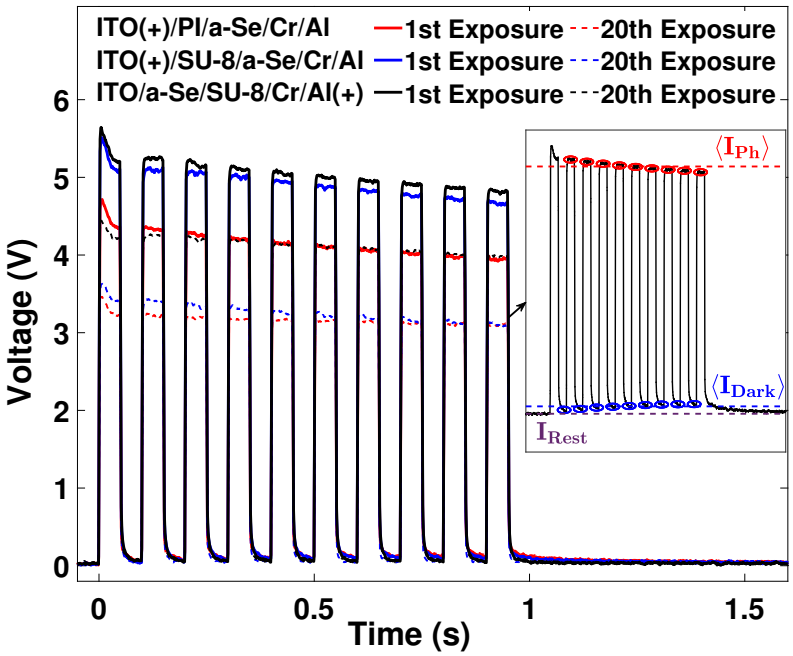
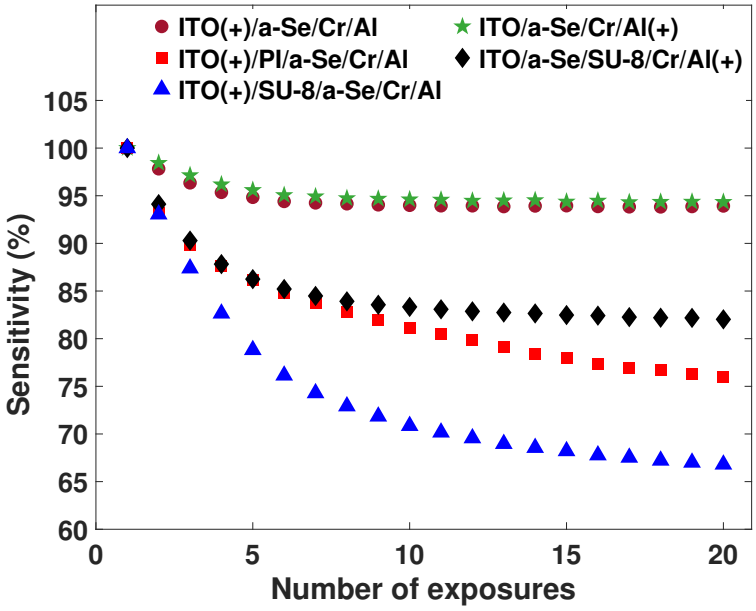


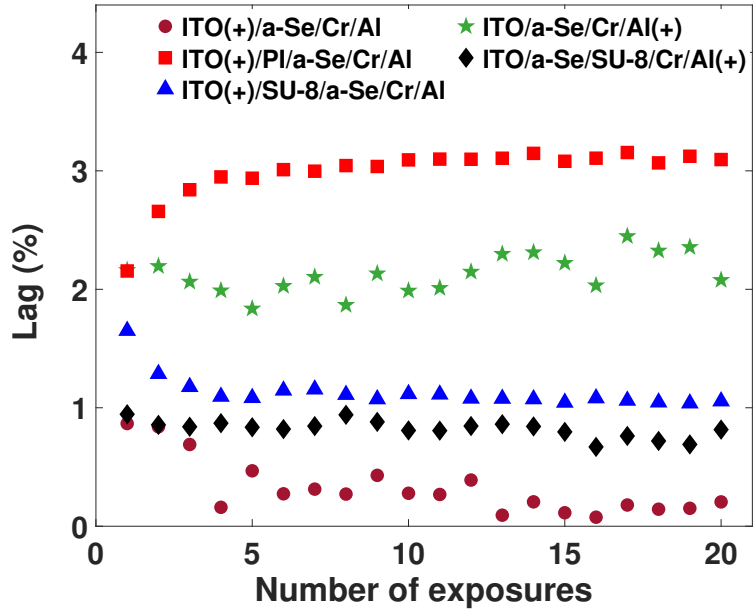
Figure 5.4: X-ray response of a-Se detectors with PI and SU-8 hole-blocking layers to first and last exposure with measured values shown on the right.

We investigated the lag and sensitivity performance of the reference device (i.e. lacking a hole-blocking layer) in two different configurations, both operating in hole-collecting mode. One configuration had the positive electrode positioned at the top, while the other had it at the bottom. Analysis of the lag and sensitivity curves in Fig. 5.5 reveals that altering the position of the positive electrode had minimal effects on the sensitivity of the reference device, suggesting that sensitivity variations in other devices are primarily caused by the presence of hole-blocking layers. However, in terms of lag, we observed that the configuration with the positive polarity at the top exhibited higher lag in the reference device. The top SU-8 device exhibited the best temporal response among the three samples (with hole-blocking layers), with an 18% loss in sensitivity from its maximum value and $< 1\%$ lag compared to a 24% drop and $\approx$3.1%lag for the PI device. The results indicate that using SU-8 in the top configuration provides lower lag than even the reference device. This might occur because SU-8 either reduces the quantity of shallow electron traps or enhances the speed of electron detrapping at the interface with a-Se, compared to the scenario where a-Se interfaces with Cr. The bottom SU-8 configuration has poorer temporal performance than top SU-8 devices, likely due to the SU-8/a-Se interface. Visual inspection by microscope indicated a-Se surface quality differences between top SU-8 and

bottom SU-8 configurations. The defects present in the bottom SU-8 interface with a-Se could potentially introduce deep electron traps, leading to decreased sensitivity. The next section presents a potential solution for addressing this interface concern.



(a)



(b)

Figure 5.5: (a) Sensitivity and (b) lag of a-Se detectors featuring PI and SU-8 hole-blocking layers biased at 20V/μm for 20 exposures, each with a dose of 8.76 mGy and intervals of 60 seconds. The positive electrode is indicated as "(+)".

5.4 Novel hole-blocking bilayer

To resolve the issue concerning the compatibility of interface between the bottom SU-8 and a-Se layer, we propose a solution involving the incorporation of n-type a-Se in between. The selection of n-type material is influenced by our previous utilization of Cs-doped a-Se, which was elaborated upon in the preceding chapter. To examine the effect of a hole-blocking bilayer structure, we investigated the insertion of Cs-doped a-Se between the top SU-8 layer and a-Se, as well as between the bottom SU-8 layer and a-Se. Six different samples were fabricated to investigate the impact of the hole-blocking bilayer on the entire structure.

In all six samples, the substrate employed was ITO on glass, which underwent a cleaning procedure using an ultrasonication bath containing acetone and isopropyl alcohol. The top electrode consisted of a 60 nm chromium (Cr) film followed by a 200 nm aluminum (Al) film deposited using an e-beam evaporation system. One sample was used as a reference without any hole-blocking layer. Two samples had 0.5 μm SU-8 spin-coated film on the ITO glass with one of them followed by 4μm Cs-doped a-Se thermally evaporated film. Another sample had 4μm Cs-doped a-Se on ITO glass. Then a 17 μm a-Se layer was thermally deposited on all six samples from a stabilized selenium alloy containing 0.5% arsenic (As) and 8-ppm chlorine (Cl). After a-Se deposition, the remaining two samples were used to deposit 4μm Cs-doped a-Se on the top surface of a-Se with one of them followed by a layer of SU-8.

The sample with the SU-8 at the bottom underwent a soft bake, followed by a post-exposure bake both at 95°C for 1 minute, and finally a hard bake at 150°C. The hard bake step was skipped for the sample with the SU-8 at the top and the soft bake and post-exposure bake for this sample occurred at 55°C for 30 minutes to minimize the impact of temperature on the a-Se layer.

5.4.1 Results

We replicated all the experiments outlined in the previous sections, starting with the dark current measurement. The method used to measure dark current stayed the same. The devices were placed in the dark for two hours and short-circuited. After that, high voltage was applied across the detector, and the dark current was measured over a 20-minute period to reach a plateau and the average of plateau value was calculated and reported. As illustrated in Figure 5.6, when examining devices with the positive electrode positioned at the bottom, the use of Cs-doped a-Se as the hole-blocking layer demonstrates

effectiveness in reducing the dark current. Following closely in performance is the SU-8 hole-blocking layer. Nevertheless, introducing a bilayer structure at the bottom electrode that includes both Cs-doped a-Se and SU-8 slightly raises the dark current in comparison to the individual hole-blocking layers.

On the contrary, for devices with a positive electrode placed at the top, relying solely on Cs-doped a-Se proves inadequate in suppressing dark current. To address this issue, incorporating SU-8 becomes essential. There is a slight increase in dark current for bilayer configuration when compared to just using the SU-8 hole-blocking layer (measured and shown in the previous section). However, adopting the bilayer configuration at the top electrode has benefits in terms of photoresponse that could help alleviate the marginal increase in dark current.

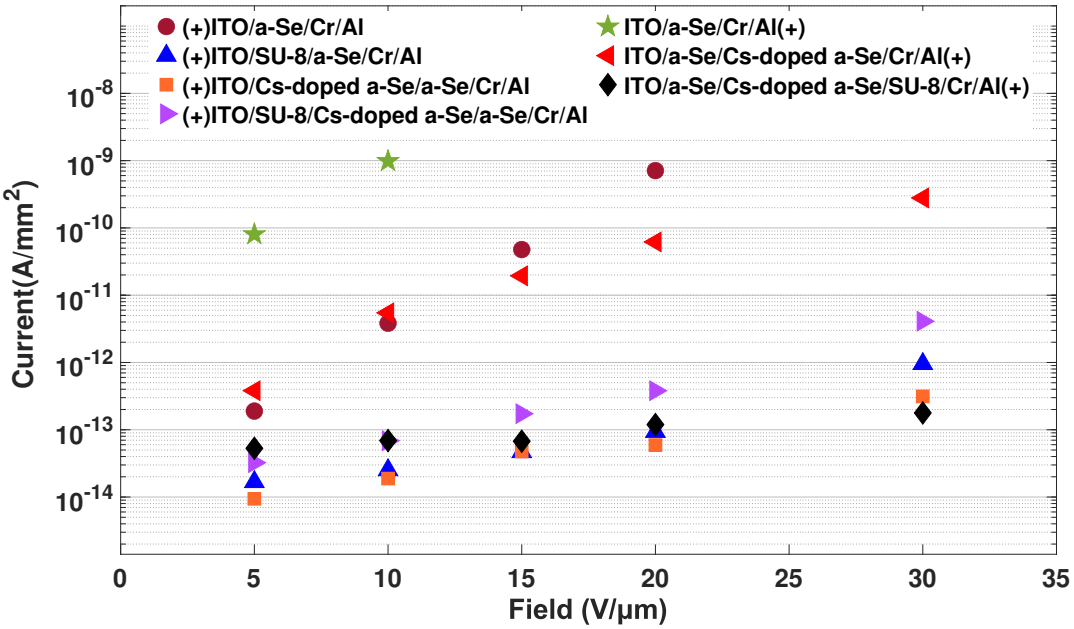


Figure 5.6: Dark current density of the a-Se detectors including those incorporating hole-blocking bilayer and single-layer configurations as a function of electric fields. The reported values are the mean of the plateau achieved after maintaining a constant electric field for 20 minutes.

A blue LED was utilized to measure photoresponse of the detectors under 20 $V/\mu m$ bias. As explained earlier, because blue light is completely absorbed near the bottom interface of a-Se where illumination occurs, a direct comparison between devices biased at

the top and those biased at the bottom is not feasible. The dotted line displayed in Fig. 5.2 is from a device discussed in the previous section. It is included here solely for the purpose of comparison, yet it should be noted that this particular device was fabricated separately. All other devices were produced in the same fabrication run. In devices biased at the bottom, the one with Cs-doped a-Se exhibits a higher signal level. Similarly, the bilayer configuration also demonstrates a comparable signal level, with the only distinction being the slightly elevated dark current. However, when compared to the SU-8 hole-blocking layer, it exhibits a slightly higher signal level and lower dark current. This indicates a potential improvement in detector performance when opting for the bilayer structure over the use of purely SU-8.

In devices biased at the top, the device equipped solely with Cs-doped a-Se displays a superior signal level compared to the other two configurations, albeit accompanied by a notably high dark current. The bilayer configuration exhibits a high initial signal level that decreases over time, yet it remains higher than the signal level observed in the device using only SU-8. Additionally, the dark current of the bilayer device is slightly more favorable than that of the SU-8 hole-blocking layer.

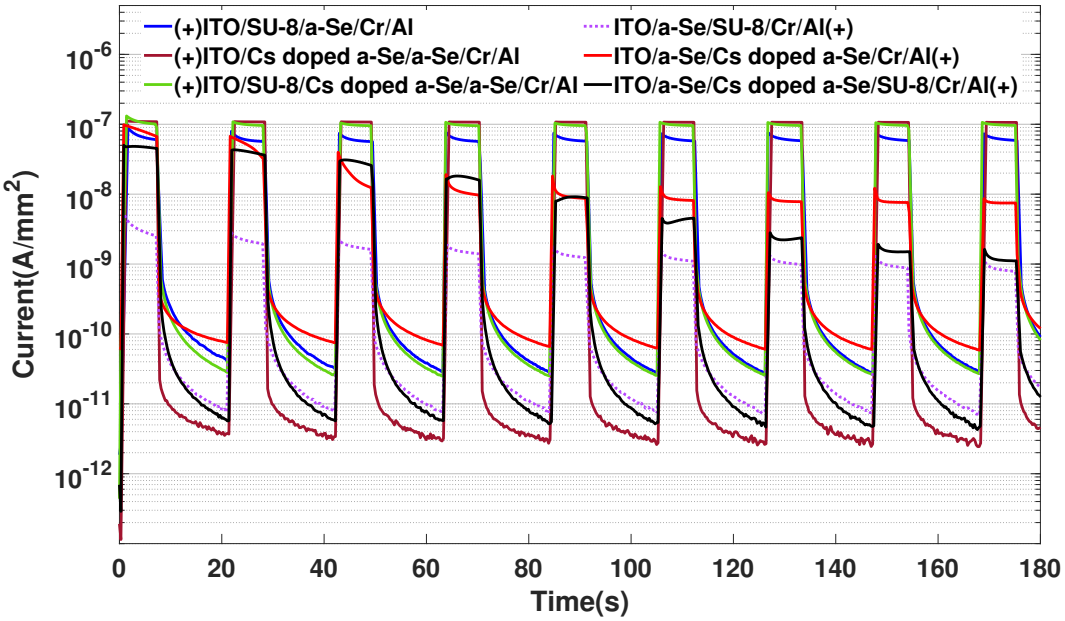


Figure 5.7: Photoresponse of a-Se detectors biased at $20V/\mu m$ to a blue LED with intensity of 110 $\mu W/cm^2$.

To enhance the sensitivity of the detector, we elevated the electric field to 30 $V/\mu m$, as illustrated in Fig. 5.8. As evident, the signal level for the bilayer device at the top increased to the extent that it became comparable to devices biased at the bottom. Notably, its signal level surpasses that of the other two devices with a positive electrode positioned at the top, all the while maintaining a low dark current similar to the SU-8 device. Therefore, employing the bilayer structure offers the dual advantage of achieving a high signal level like that of Cs-doped, while also benefiting from a low dark current similar to the SU-8 device. Regarding the bottom-biased devices, the bilayer configuration does not exhibit significant differences in photoresponse when compared to the SU-8-only setup. However, as we will show later, it does enhance the detector's sensitivity.

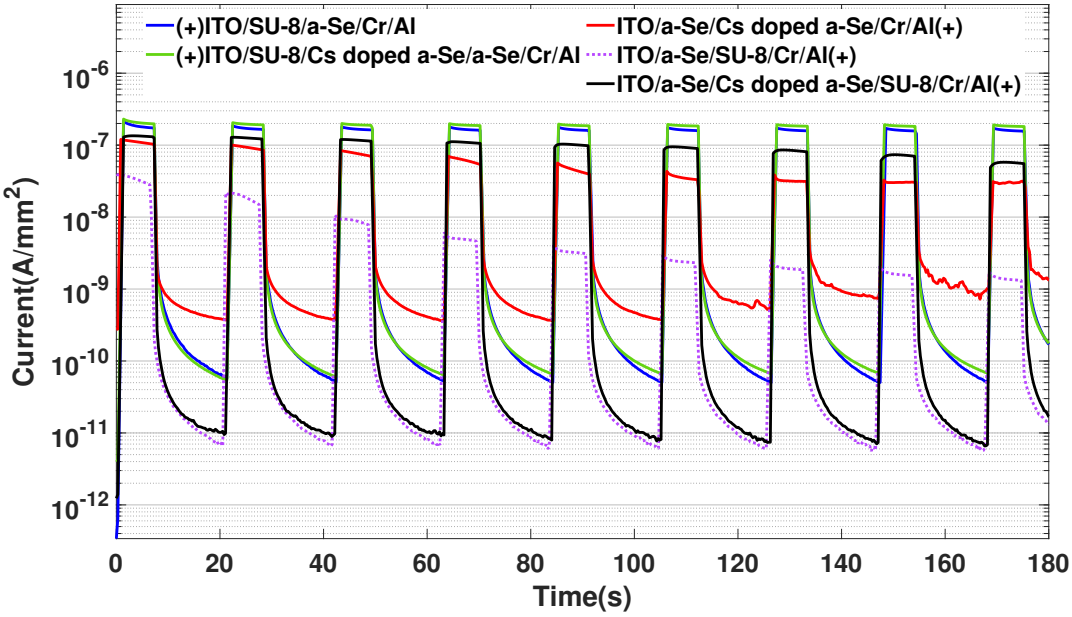


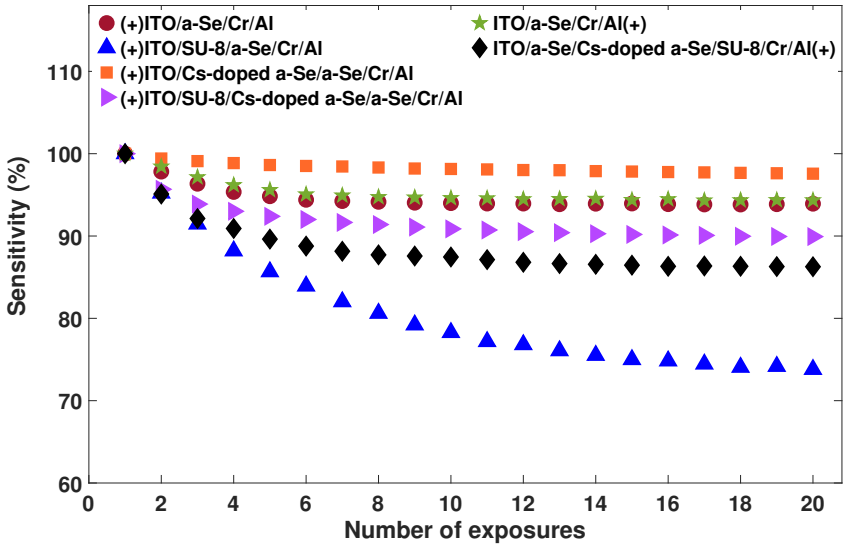
Figure 5.8: Photoresponse of a-Se detectors biased at $30V/\mu m$.

For the evaluation of temporal performance of the devices, a similar approach to the previous section was adopted and the results are illustrated in Fig. 5.9. We showcased the reference device in two distinct polarities, demonstrating that any observed deviations in sensitivity exclusively result from the incorporation of hole-blocking layers. However, it is important to note that the lag for this device with the bias applied at the top exhibits a higher value in comparison to when the bias is applied at the bottom. From the sensitivity graph for when the SU-8 is positioned at the bottom, a higher sensitivity drop is observed

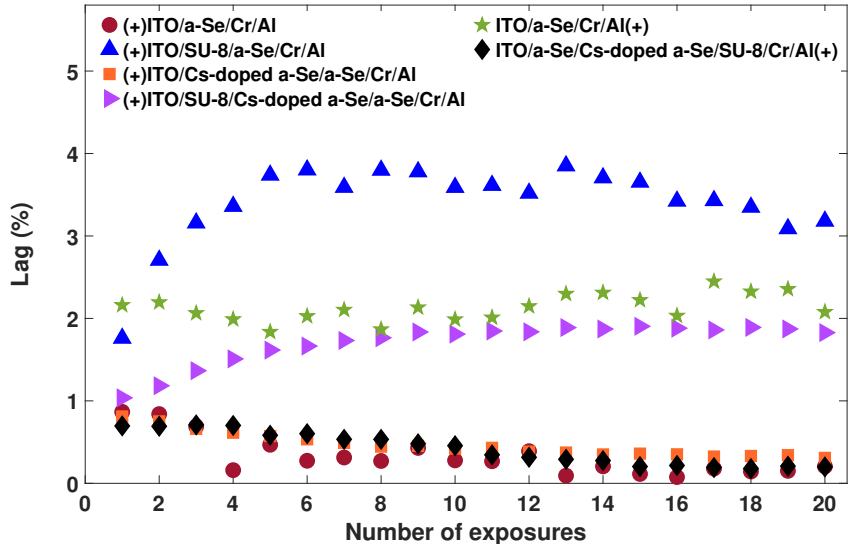
likely due to the poor interface with a-Se as seen in the previous section. However, introducing a Cs-doped layer in between enhances sensitivity significantly, by approximately 16.1%. This improvement in x-ray sensitivity is noteworthy. Moreover, the lag is reduced to less than 2% for the bilayer configuration. However, the Cs-doped layer alone at the bottom still outperforms the bilayer setup at the bottom.

One potential explanation for the results obtained for the bilayer at the bottom is that the presence of the SU-8 interface with a-Se at the bottom has introduced deep electron traps caused by defects. These traps likely contributed to the extensive decrease in sensitivity. The incorporation of Cs-doped a-Se, on the other hand, appears to mitigate this issue by filling these deep traps with excess electrons, thereby enhancing the signal level, as previously discussed. Another plausible reason is that since SU-8 and Cs-doped a-Se are hole-blocking layers, they have deep hole traps and by applying the bias these traps are filled. If so, the photogenerated electrons might go through charge recombination with these trapped charges but then this would not fully justify why the addition of Cs-doped is helping with the sensitivity.

So it is more probable that the first explanation is true. Furthermore, the inclusion of Cs-doped a-Se seems to marginally reduce the capacity of Cs-doped a-Se to reduce dark current. This could be due to electrons trapped in the introduced deep traps due to the surface defects undergoing recombination with the holes injected from the positive electrode. However, the integration of SU-8 plays a role in controlling the rise of dark current due to the barrier it forms. This barrier leads to a reduced number of holes reaching the interface of the Cs-doped a-Se layer. Alternatively, there is a possibility that SU-8 contributes to lowering the rate of recombination, as emphasized in a previous study [79]. In the case of positioning the bilayer at the top, the improvement in the sensitivity is likely due to the possibility that the excess electrons fill the electron traps at the a-Se interface causing the photogenerated electrons to reach the top electrode. In conclusion, it would appear the bilayer structure performs better because it combines the advantages of both Cs-doped a-Se and the SU-8 layer.



(a)



(b)

Figure 5.9: (a) Sensitivity and (b) lag of a-Se detectors including the hole-blocking bilayer, biased at 20V/μm for 20 exposures (8.76 mGy each) with 60-second intervals. The positive electrode indicated as "(+)".

For devices biased at the top, apart from the reference device, only the bilayer configu-

ration was tested. The device with Cs doping at the top experienced breakdown indicating inadequacy in suppressing the dark current. When comparing these results with the device in the previous section that utilized only SU-8, the bilayer demonstrates slightly superior sensitivity and lag performance. The lag drops below 0.5% after 7 exposures, which is a significant enhancement. Notably, in certain instances, the lag performance even surpasses that of the Cs-doped layer at the bottom. This progress is noteworthy since positively biased electrodes at the top of selenium devices typically result in devices that exhibit higher lag.

Among the samples featuring hole-blocking layers, the bilayer at the top displayed the most favorable lag performance, with a sensitivity decrease of 14% after 20 exposures (20R).

5.5 Time of flight measurement

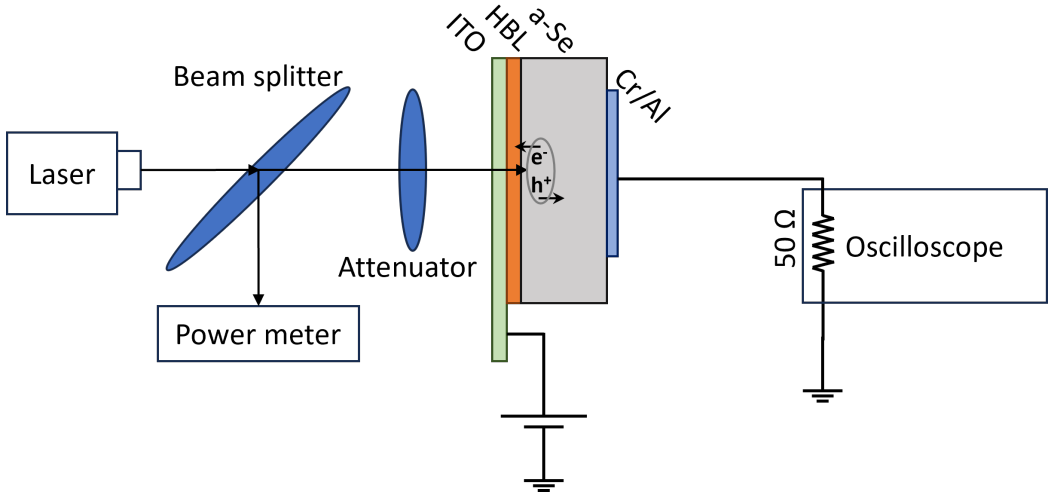


Figure 5.10: Time of flight experimental setup.

Time-of-flight (TOF) experiment is a method to explore the charge transport properties within highly resistive and disordered solids, such as a-Se. [82]. The experiment setup for TOF measurement is shown in Fig. 5.10. Here, a device containing a-Se is exposed to an 800 ps laser pulse (with wavelength of 337 nm) from the ITO side which is a transparent

electrode. This results in the creation of a confined charge plane. Owing to the non-dispersive behavior of carrier movement in a-Se [83, 84], the charge plane's width stays relatively constrained as it travels the thickness of a-Se under the influence of an electric field. This event is captured by an oscilloscope, which enables the evaluation of carrier mobility via the following equation:

$$\mu = \frac{L^2}{t_r.V}, \tag{5.6}$$

where L is the thickness of a-Se layer and t_r is the transit time measured from the detector response and V is the applied voltage.

The TOF technique was utilized to specifically investigate the charge transport characteristic within an a-Se device incorporating a hole-blocking contact. This measurement is essential to comprehend the effect of the hole-blocking layer on transient response. Additionally, the TOF method provides a means to estimate the voltage drop across the hole-blocking layer. For comparison, a device without the hole-blocking layer was also examined. However, conducting TOF measurements at high electric fields without the hole-blocking layer posed challenges due to substantial dark current and device breakdown. As a result, only a few measurements were carried out for the reference device.

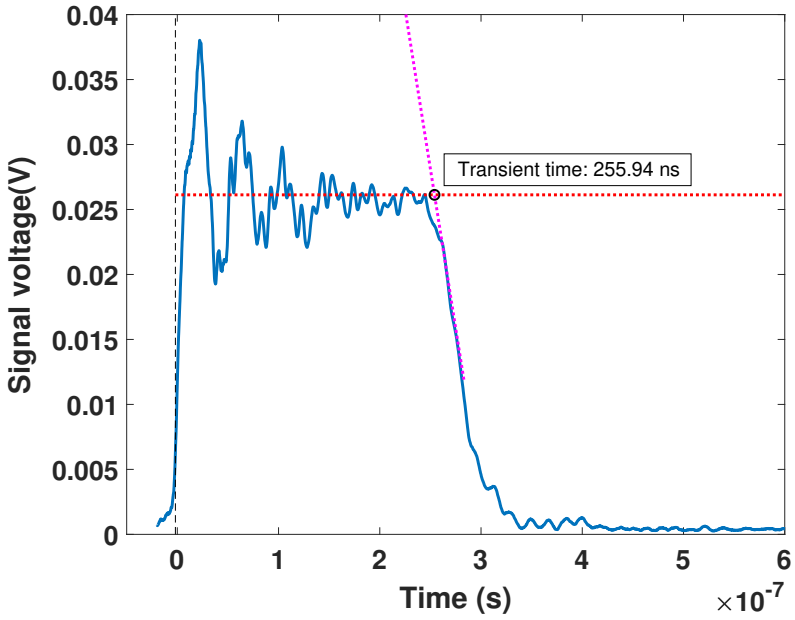
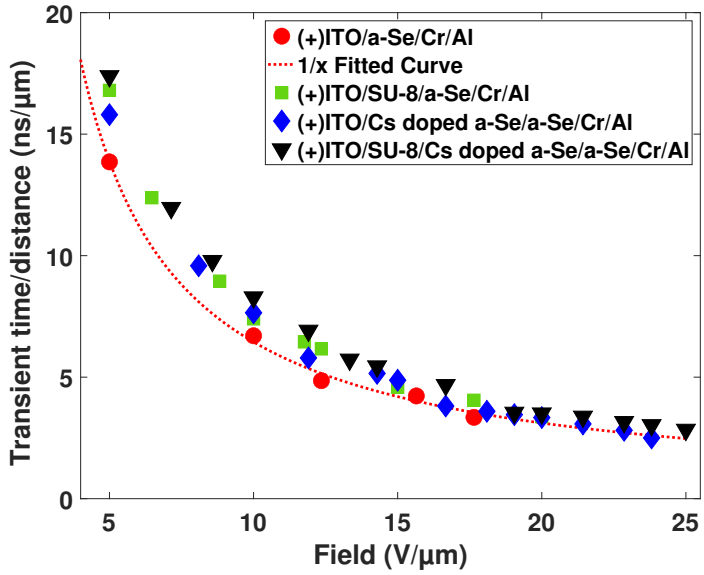


Figure 5.11: Behaviour of the detector utilizing hole-blocking bilayer at the bottom of the detector which is biased at 150 V ($\approx 7V/\mu m$) when exposed to a short laser pulse, with fitted lines utilized to approximate the transit time.

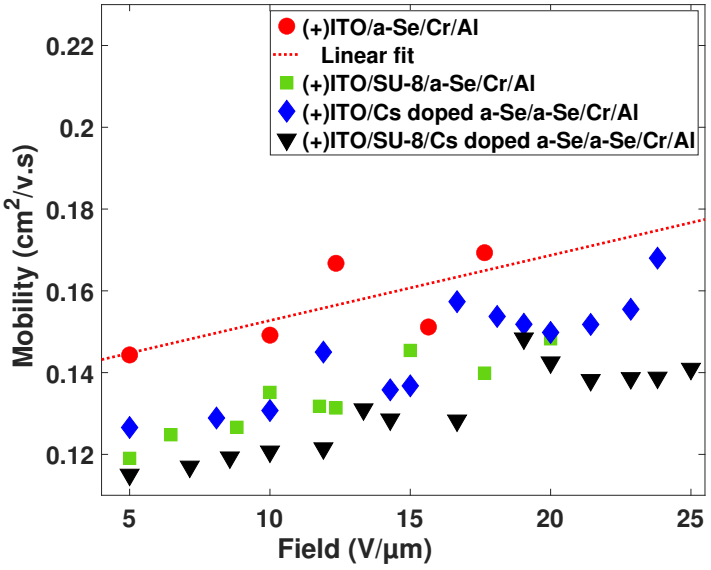
In this section, our main focus was on samples biased positively at the bottom. With the laser entering from the ITO side and being fully absorbed upon entering the selenium bulk, this configuration allowed us to track the entire journey of holes traveling the selenium thickness. This experiment enabled us to measure the time taken for holes to travel across the entire selenium thickness. Fig. 5.11 shows the detector response to a laser stimulation and the point considered as transit time is marked in the TOF graph which is obtained from the intersection of the plateau region and the line fitting the decay region. The TOF measurement shows oscillation which is due to the low input impedance of the oscilloscope, however, a careful fitting was done to obtain the correct transit time. This graph shows the signal for a device with SU-8 and Cs doped a-Se bilayer utilized at the bottom of the detector under 150 V biased voltage ($\approx 7V/\mu m$).

The transit time divided by the a-Se thickness (including doped a-Se) is illustrated in the Fig. 5.12(a). Subsequent mobility calculations, derived from transit time and electric field as shown in equation 5.6, yielded insightful results that are displayed in Fig. 5.12(b). Notably, the sample without a hole-blocking layer demonstrated the highest hole mobility among all of the samples and this is expected because there is no hole-blocking layer that

causes charge accumulation.



(a)

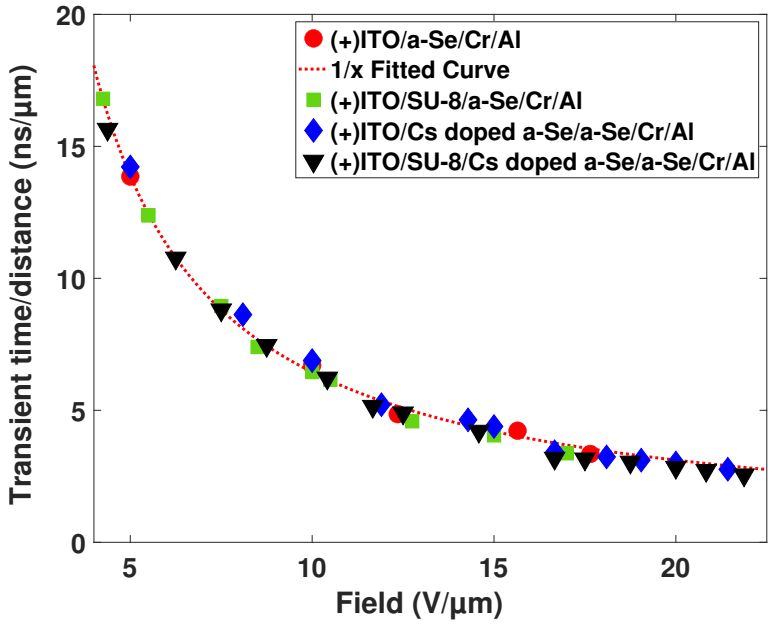


(b)

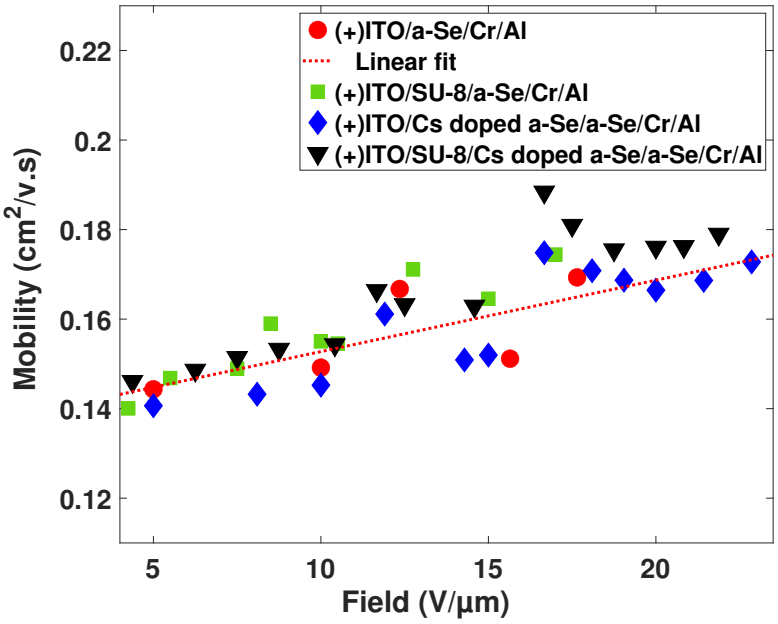
Figure 5.12: (a) Transit time divided by thickness plotted against the electric field, without accounting for the voltage drop across the hole-blocking layer. (b) Mobility is calculated based on the data derived from the graph in (a)

For estimating the voltage drop across the hole-blocking layer, we used the graph of transit time divided by distance vs. the electric field, which should follow 1/X curve [85]. This graph displays the fitted curve representing the data from the reference device, while other samples diverge from this expected behavior. Adjustments to the electric field are necessary to bring the other samples closer to the reference curve. However, when considering devices with Cs doping, it is important to account for the altered transit time due to Cs-doped n-type material. This doping reduces hole mobility, and the combined effect of Cs doping with the intrinsic material reduces effective hole mobility. Thus, transit time needs to be adjusted to align the curves with the reference device, particularly for devices with Cs doping.

The analysis of the fitted data reveals that in devices featuring an SU-8 hole-blocking layer, the voltage across the a-Se layer corresponds to 85% of the applied voltage. When the device incorporates a bilayer structure, the voltage across the a-Se layer accounts for 87.5% of the bias voltage. This difference arises from the inclusion of doped selenium within the voltage calculation for the a-Se layer, leading to a higher voltage allocation to selenium due to voltage division. Utilizing these numbers suggests that the resistivity of SU-8 is six times more than a-Se. For the devices incorporating Cs-doped selenium, either as standalone or within the bilayer arrangement, their transit times were adjusted by a factor of 0.9 to compensate for the reduced hole mobility. The outcomes of these adjustments are depicted in Fig.5.13, wherein all data points from the other devices closely follow the curve corresponding to the reference device. Furthermore, the computation of their hole mobility after these adjustments confirms their placement within a similar range to that of the reference device.



(a)



(b)

Figure 5.13: (a) Transit time divided by thickness plotted against the true electric field across selenium layer including the doped selenium (b) Mobility calculated based on the data derived from the graph in (a).

5.6 Application to dynamic imaging

To examine the lag and sensitivity in real-time, dynamic imaging, we explored fluoroscopy. Fluoroscopy is a key method for image-guided therapies. The invention of the active matrix flat panel detector has brought about great improvements, making fluoroscopy more sensitive to X-rays and showing clearer differences in the images, along with other positive changes such as improved dynamic range and less distortion of the image due to the old image intensifier technology. Transitioning to digital detectors marked a significant advancement, enabling us to save and manipulate the initial images using digital methods. This transformation altered how we assess image quality. However, specific guidelines for evaluating timing in fluoroscopy are not yet established. Fluoroscopy distinguishes itself from conventional X-ray images by presenting a sequence of images that are observed in real-time. This dynamic characteristic integrates time into the image creation process.

In many instances of fluoroscopy, there is internal movement within the body, and sometimes the clinician may shift position intraprocedure. While we can manage the doctor's movements, we lack control over bodily motions (e.g. the beating heart). This underscores the significance of investigating the system's performance in the presence of motion, which, in turn, contributes to enhancing patient care through these advanced imaging techniques. When objects move during imaging, there can be problems with how clear the images are. Digital detectors are faster and clearer than the older ones, but there are still some memory issues like lag and ghosting. These issues are part of how digital flat panel detectors work, and they can make the live images difficult to see during a procedure. In this section, we examine the fabricated devices' lag and sensitivity for fluoroscopy. To set up the same conditions as fluoroscopy we need to consider dose and frame rate. The fastest common frame rate is 30 frames per second and during normal fluoroscopy operations, the radiation dose rate ranges from 10 to 50 mGy per minute. This rate applies to continuous or 30 frames per second fluoroscopy. In high dose rate fluoroscopy, the skin of an average patient is exposed to radiation at a rate of 20 to 90 mGy per minute during continuous or 30 frames per second fluoroscopy. However, regulations set a maximum limit of 200 mGy per minute for high dose rate fluoroscopy to ensure safety.

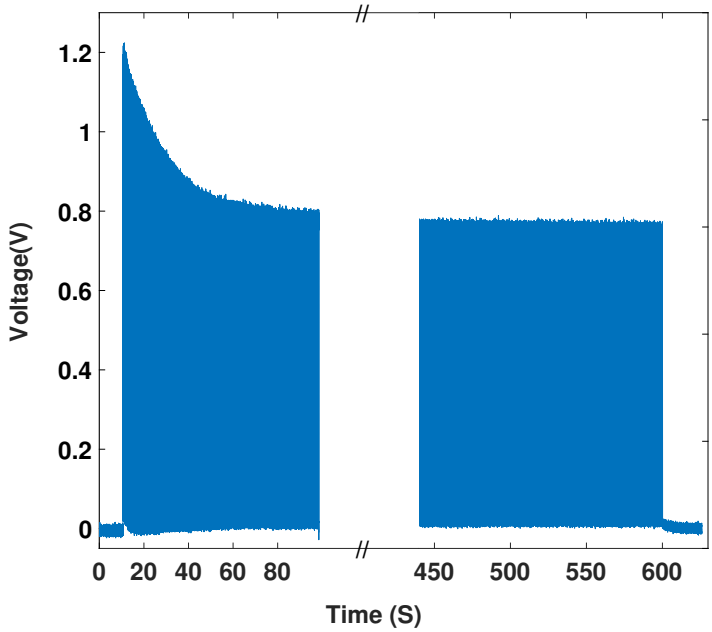


Figure 5.14: The response of the detector with hole-blocking bilayer configuration biased at $10V/\mu m$ in fluoroscopy mode operating at a frame rate of 30 frames per second.

For this study, we set the x-ray exposure to 120 mGy per minute to test the device under the extreme condition of high energy signals that degrade the sensitivity the most. The 30 frames per second exposure was used with a 10 ms X-ray ON time at 70 kv_p and 80 mA settings. The pulsed X-ray was ON for 10 minutes (1.2 Gy in total) and the beginning and end of the response were recorded and displayed in Fig. 5.14 for the device with bilayer at the top biased at 10 $V/\mu m$. As illustrated in this figure, after almost 90 seconds the signal reached a steady signal level and it held the signal level until the end of the 10 minutes. The flatness of signal level at the end is impressive and it suggests that soaking the detector with X-ray before measurement can resolve the initial sensitivity loss at the beginning reaching a very steady signal level. The lag was also measured based on the elevated dark current in the middle of the exposure minus the initial dark current divided by the signal level as shown in equation 5.4. The sensitivity drop and lag were measured to be 41% at the end of 10 minutes and 2% in the middle respectively.

To compare the bilayer's performance, a reference device with a PI hole blocking layer was also tested under the same condition and electric field and the results are shown in Fig. 5.15 with The sensitivity drop was measured to be 45.7% and the lag was 4%. The PI device shows sensitivity loss at the beginning but it lacks the flatness observed in the

bilayer at the top. It seems even at the end, the signal is still dropping. This effect was initially observed in the sensitivity graph in Fig 5.5 where the sensitivity was declining even after 20 exposures.

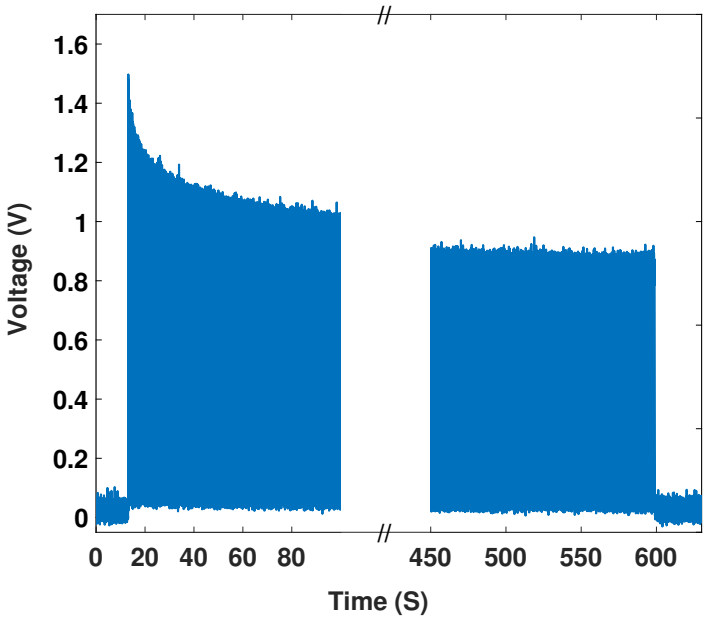
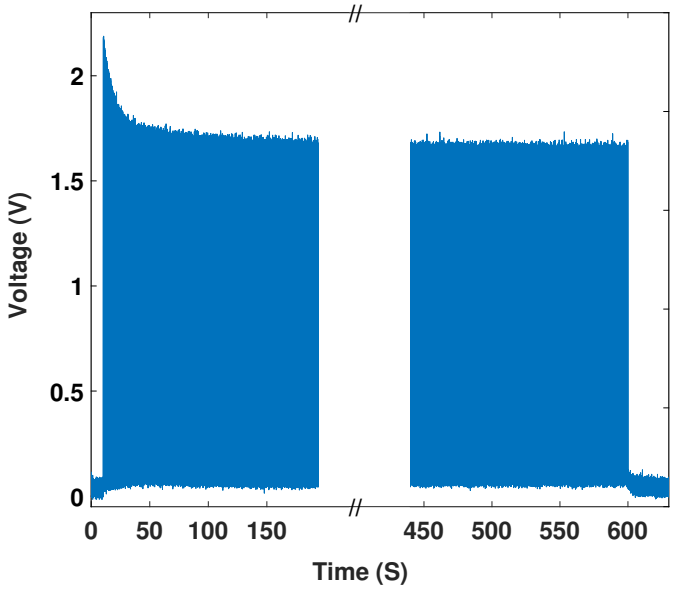
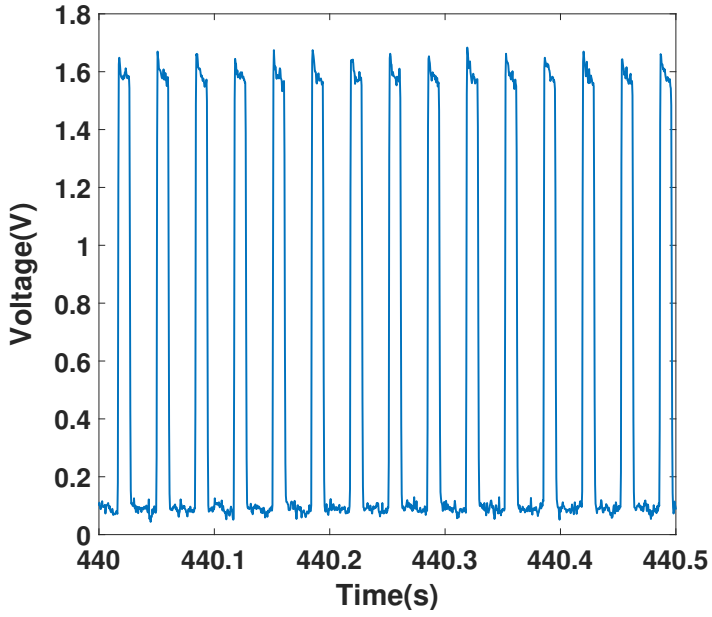


Figure 5.15: The response of the detector with PI hole-blocking layer biased at $10V/\mu m$ in fluoroscopy mode operating at a frame rate of 30 frames per second.

To explore the effect of increasing the field on the lag and sensitivity in fluoroscopy application we increased the field to 20 $V/\mu m$ for the bilayer configuration. Fig. 5.16 indicates that the sensitivity drop changed to 31% by the end of 10 minutes, showing 10% improvement compared to the device biased at $10V/\mu m$. The lag measured at the middle was 2.7% which shows a slight increase as expected. It is notable that the flatness in the signal level is still there and this is promising for fluoroscopy applications. To show the transient behavior of the detector in response to the pulsed X-ray, a zoomed region is displayed in Fig. 5.16(b) which demonstrates the fast transient response of the detector. The observed uniformity in the bilayer, as opposed to the PI layer, could stem from the fewer vacant deep electron traps present in SU-8 in comparison to PI. This is likely because the excess electrons from Cs-doped a-Se occupy a portion of these traps. Alternatively, it is possible that a greater number of deep traps are introduced at the PI interface under high dose exposure for 10 minutes.



(a)



(b)

Figure 5.16: a) The response of the detector with hole-blocking bilayer configuration biased at $20V/\mu m$ in fluoroscopy mode operating at a frame rate of 30 frames per second. b) Enlarged view of the detector's response.

5.7 Conclusion

Minimizing dark current plays a crucial role in achieving accurate photon detection. As we delve into the application of the bottom microstrip design, where the hole-blocking layer needs to be positioned on the top side, we acknowledge the significance of the placement of this layer. While organic polyimide (PI) layers have previously demonstrated excellent hole-blocking properties, enabling high voltage mode operation with selenium devices, their usage on the top surface of temperature-sensitive selenium as a hole-blocking layer has been limited due to their high baking and curing temperatures.

In this chapter, we have investigated the use of low-temperature SU-8 as a hole-blocking layer for selenium, along with a new bilayer configuration, incorporating SU-8 and Cs-doped a-Se. Our findings reveal that devices employing SU-8 as a hole-blocking layer, whether positioned at the top or bottom, maintain a dark current below 1 pA/mm^2, even when subjected to an increased electric field of 40 V/μm. Devices featuring the SU-8 hole-blocking layer on the top surface exhibit an 18% reduction in sensitivity after exposure to a cumulative X-ray dose of 0.175 Gray (Gy), while still maintaining lag or persistent photoconductivity below 1% at 20 V/μm. In comparison, devices produced in the same manufacturing cycle that utilize the previously reported PI hole-blocking layer on the bottom surface experience a 24.1% sensitivity decrease and lag of around 3.1%.

These outcomes indicate the feasibility of achieving higher-performance selenium detectors using SU-8 blocking layers, which could accelerate the commercial advancement of low-lag, high-gain selenium radiation detectors for dynamic medical imaging. To address compatibility concerns with the SU-8 layer at the bottom, we introduce the novel bilayer configuration. This bilayer configuration was assessed both at the top and bottom positions. Results demonstrate that when the bilayer is positioned on the top, it benefits from the advantages of both layers, showcasing the high signal level of Cs-doped a-Se while maintaining a low dark current similar to the SU-8 layer. Among the samples featuring hole-blocking layers, the bilayer at the top displayed the most favorable lag performance below 0.5 % after the 7th exposure, with a sensitivity decrease of 14% after 20 exposures (0.175 Gy). Implementing this bilayer configuration at the bottom enhances the sensitivity by 16.1% compared to the device with only SU-8 hole-blocking layer, indicating that Cs-doped a-Se effectively addresses interface challenges when using SU-8 at the bottom.

Chapter 6

Photon counting performance

6.1 Introduction

In previous chapters, we explored applications of high-energy radiation and the utilization of a-Se in a multilayer configuration to enhance radiation stopping power. We also characterized a new read-out method for reducing the complexity of this structure. The measurements conducted in the preceding chapters were all in energy integration mode, which involves signal accumulation over time and leads to a high signal level. However, in applications like SPECT and spectral CT imaging, the detection of each photon holds significance, prompting the use of the photon counting method to differentiate photons based on their energy levels. To accommodate these applications and characterize the detectors, pulse height spectra (PHS) measurement is necessary.

In this chapter, we prepared an experimental setup for PHS measurements and presented results obtained from a conventional detector as well as our microstrip detector design. As mentioned in the previous chapter, to achieve lower noise and background signal in photon counting mode, we introduced a novel hole-blocking bilayer. Consequently, the microstrip detector, featuring a charge division readout with the hole-blocking bilayer, underwent testing in the PHS setup, and the results are presented.

6.2 Single pixel design

To ensure the proper functioning of the setup and its calibration to display accurate energy levels for different gamma sources such as ^{241}Am and ^{57}Co, we initially employed a con-

ventional a-Se detector with a single pixel. This pixel had an active area of 1 mm^2, chosen to minimize capacitance, reduce noise, and lower the dark current. The substrate used was ITO on glass, which underwent a cleaning process in an ultrasonication bath containing acetone and isopropyl alcohol. Following this, a 1 μm thick PI layer was spin-coated onto the ITO glass and cured at 350°C. The sample utilized an 80 μm a-Se layer to provide higher stopping power. This layer was thermally deposited from a stabilized selenium alloy containing 0.5% arsenic (As) and 8 ppm chlorine (Cl). The top electrode consisted of a 60 nm chromium (Cr) film deposited using an e-beam evaporation system.

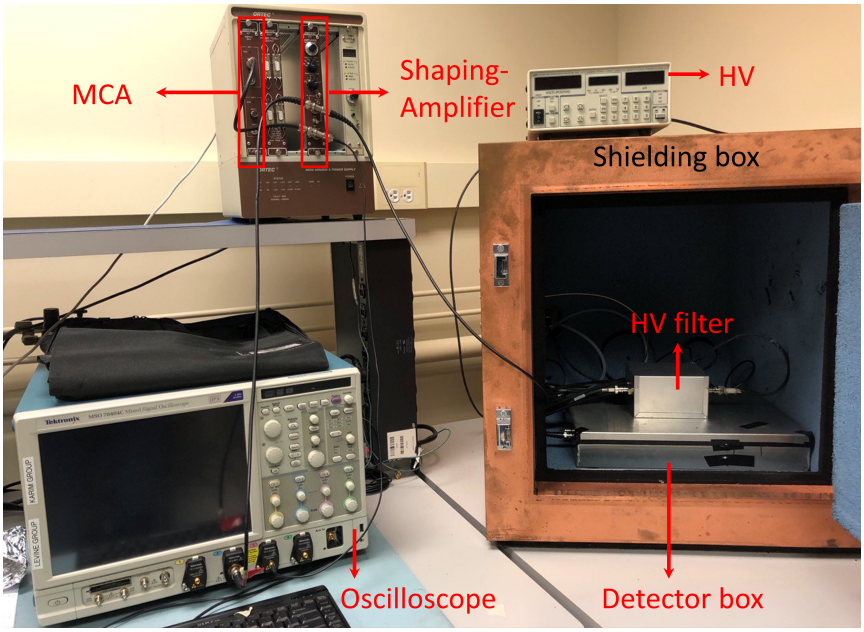
6.2.1 CoolFet experimental setup

The photon counting setup to obtain PHS consisted of several components, including the detector box, high voltage (HV) power supply, HV filter, preamplifier, shaping amplifier, multichannel analyzer (MCA), and oscilloscope. This setup is illustrated in Figure 6.1. The detector box is enclosed within a copper casing, acting as a Faraday cage to reduce electromagnetic interference and minimize ambient noise in the laboratory.

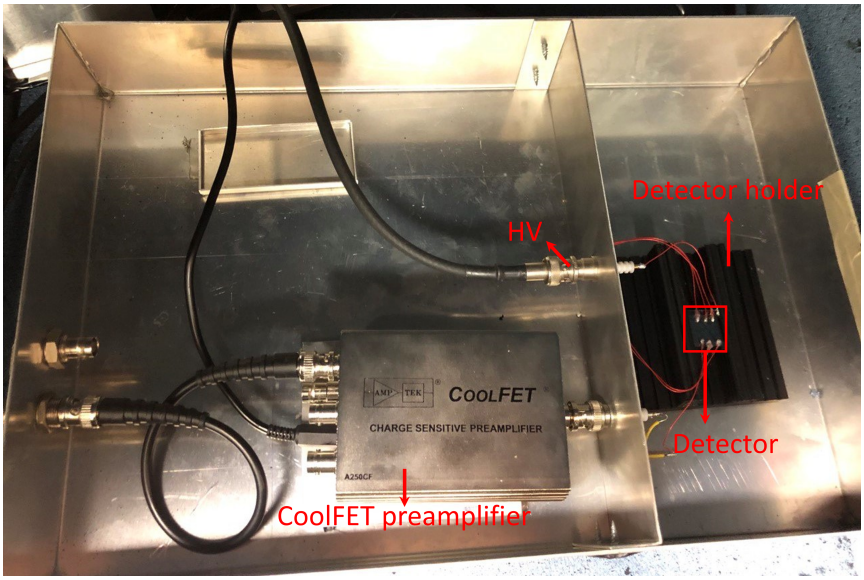
Within the detector box, was the detector itself along with the detector holder introduced in Chapter 3, the HV connection, and the CoolFET preamplifier. For this specific section, only one channel was required to measure the signal, allowing the utilization of the Amptek CoolFET preamplifier. The primary role of the preamplifier is to integrate the current pulses produced by absorbed photons. Variations in the signal caused by photon absorption in the detector are recorded as charges across the feedback capacitor, which subsequently dissipates through the feedback resistor. As a result, the output voltage of this preamplifier maintains a clear relationship with the generated charge from the capture of a single photon as follows:

$$V_{out} = -\frac{Q_{in}}{C_f}, \tag{6.1}$$

where Q_{in} is the charge generated by photon and C_f is the capacitor in the feedback loop. Moreover, the preamplifier functions as a buffer for the a-Se detector, effectively isolating it from the subsequent stages in the circuitry. To mitigate potential capacitive loading effects on the preamplifier's input stage, we placed the a-Se detector in close proximity to the preamplifier and used a short interconnecting cable.



(a)



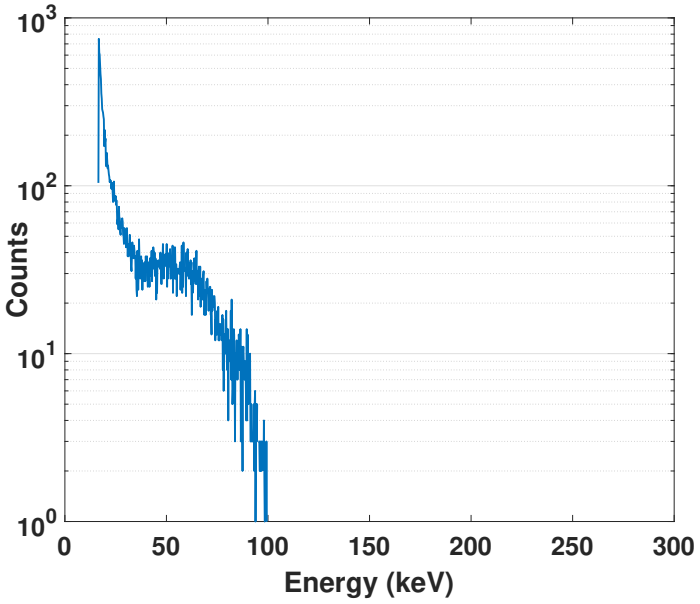
(b)

Figure 6.1: (a) Pulse-height spectroscopy experimental setup, (b) detector box including the detector and the CoolFET preamplifier.

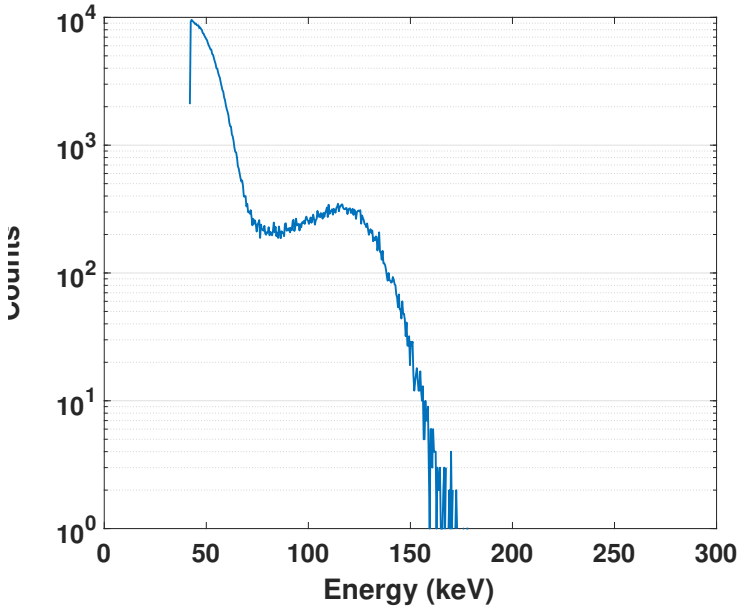
The signal from the preamplifier is directed to the shaping amplifier, a device responsible for shaping and amplifying the signal, as suggested by its name. Typically, the shaping circuit comprises two components: a differentiator to identify the signal's peak and an integrator to prolong the peak's duration and reduce high-frequency noise. In the case of the Ortec-570 model, the shaping time can be selected and the peaking time is 2.2 times of the shaping time. Given that the charge collection process in a-Se takes a few microseconds, a shaping time of 10 microseconds was chosen, the highest option available on the instrument which corresponds to peaking time of 22 μs. The gain was set to 750, and the resulting output was channeled to a computer via the MCA (Ortec-927). The role of the MCA is to convert the analog signal into a digital format and present it graphically, often as a pulse height spectrum (PHS). An oscilloscope was used to monitor the shaping amplifier and preamplifier outputs to record their response to a single photon.

6.2.2 Results

To start calibration, first, we tested the setup with the detector biased at 800 V (i.e. 10 $V/\mu m$) and without any gamma source. This was necessary to determine the noise profile and to set the lower bin above the noise threshold. Then we started with ^{241}Am and since our active area is small, we directly put the gamma source on the sample to get the most of the signal. The gamma source activity was higher compared to ^{57}Co, so only a few hours of data collection was enough to show the peak in the pulse height spectra as illustrated in Fig. 6.2(a). We labeled the peak as 59.9 keV and then changed the source to ^{57}Co source and repeated the experiment to set the lower bin threshold above the noise floor and obtain the peak in the PHS. However, the activity of the source and the stopping power of a-Se were low, so the measurement took 5 days to get a distinct peak and the result is displayed in Fig.6.2(b). We labeled this peak as 120 keV to finish the calibration process. There are more counts observed in lower bins compared to ^{241}Am which can be attributed to the higher scattering that happens at higher energies especially when the semiconductor material is unable to fully stop the photons.



(a)



(b)

Figure 6.2: Pulse height spectra of a conventional a-Se detector in response to (a) ^{241}Am gamma source, (b) ^{57}Co gamma source.

Next, we substituted the conventional detector with the new design introduced in previous chapters with resistive microstrips. The detector box shown in 6.1(b) shows the CoolFET setup with the design featuring the top resistive microstrips. Unfortunately, we were unable to detect any photons with this detector due to the excessive noise. Also, we needed to read both ends of the microstrip to locate the impinging photons and the CoolFET had only one channel. To address this concern, we replaced CoolFET with the CUBE CMOS preamlifier from XGLabs that has lower noise and we designed a printed circuit board (PCB) to hold multiple CUBEs to accommodate our dual-ended readout requirement.

6.3 Microstrip design

The microstrip design utilized glass as the substrate, which underwent a cleaning process in an ultrasonication bath containing acetone and isopropyl alcohol. To create the microstrip readout at the bottom of the structure, resistive ITO was deposited on the glass substrate using an e-beam evaporation and a shadow mask. A 64 μm thick layer of a-Se was then thermally deposited on the bottom electrodes. This deposition was performed using a stabilized selenium alloy containing 0.5% arsenic (As) and 8 ppm chlorine (Cl). Subsequently, a 12 μm thick layer of Cs-doped a-Se was thermally deposited onto the surface of the previously mentioned a-Se layer. This was followed by the spin-coating of an SU-8 layer to form a hole-blocking bilayer. Notably, the sample did not undergo a hard-baking process. For the soft bake and post-exposure bake of this sample, a temperature of 55°C was maintained for 30 minutes to minimize any potential impact on the properties of a-Se due to the temperature.

6.3.1 CUBE experimental setup

The experimental setup is similar to the configuration described in the preceding section, with some modifications related to the preamplifier and the detector box. Our experimental setup consists of two distinct enclosures: detector enclosure and setup enclosure. Most of the setup components, including the detector enclosure, bias board, stage, and collimator, were enclosed within a large metal box as illustrated in Fig. 6.3. This setup enclosure was grounded to minimize the noise and acted as a Faraday cage, shielding the components from external electromagnetic interference. Within the setup enclosure, several components were housed. The presence of a resistive microstrip with the proposed charge division method necessitates precise movement of a point-like radiation source across the electrode.

To achieve this, we introduced a collimator into the setup with a motorized stage. The collimator is constructed from 0.5 cm of lead and had a central aperture measuring 1 mm in diameter. Moreover, it featured a designed groove intended to secure the gamma source disk. This collimator was integrated with a servo motor from Thorlabs. The primary objective of the motorized collimator was to enable precise movement of the gamma source in the x and y directions with sub-millimeter resolution. This capability was crucial for accurately evaluating the spatial resolution performance of the system.

An 8-channel bias board from XGLab is utilized to drive the CUBEs mounted on the carrier board within the detector enclosure. To establish necessary electrical connections, a flat cable with a ferrite bead was used to connect the carrier board to the bias board. This configuration minimized unwanted noise during data acquisition and transmission. The rest of the setup components were outside the setup enclosure specifically, the HV filter, shaping amplifier, and MCA.

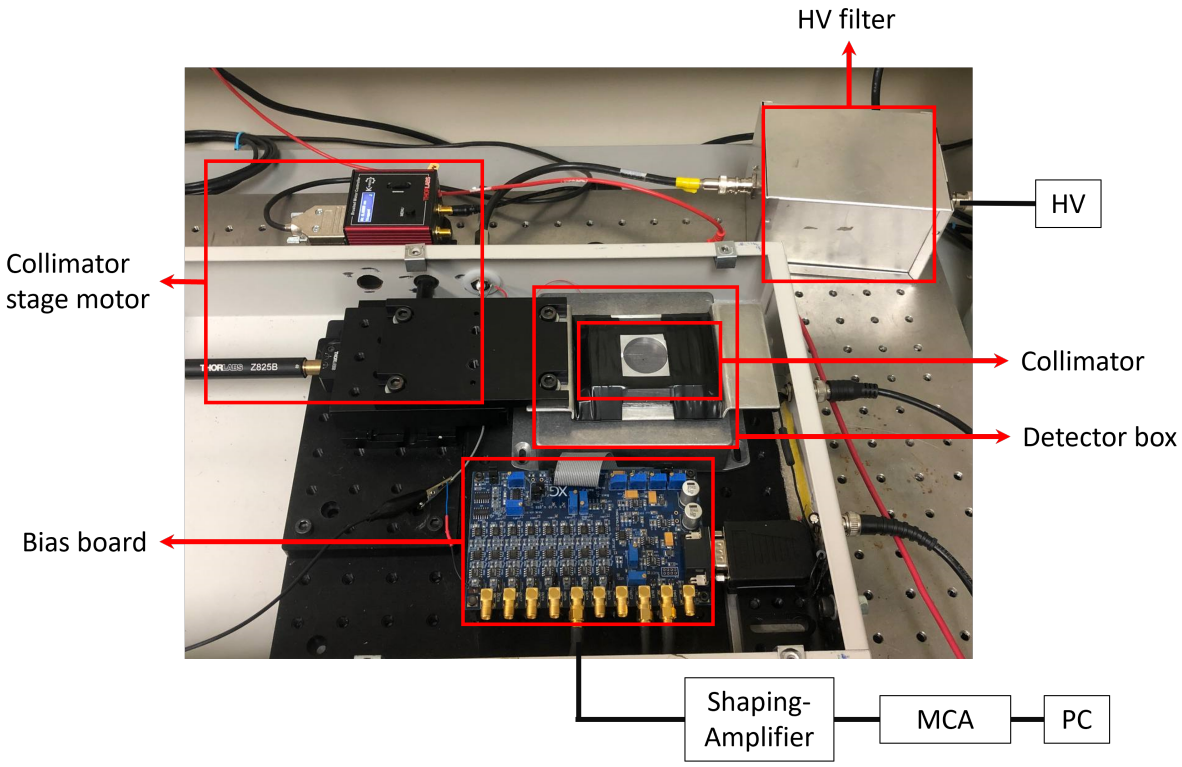


Figure 6.3: PHS setup utilizing CUBE preamplifier along with its bias board, collimator, and motorized stage

There is an aperture at the top surface of the detector enclosure to allow the photons to pass without any scattering. The detector enclosure as indicated in Fig. 6.4 included the detector itself, securely attached to the carrier board. Developing the design for the carrier board was a complex task, and numerous iterative processes were undertaken to optimize the layout and overcome potential issues caused by the reset line being in close proximity to the CUBE input. The primary objective revolved around ensuring the best functionality of the CUBE preamplifiers, initially without any detector connected.

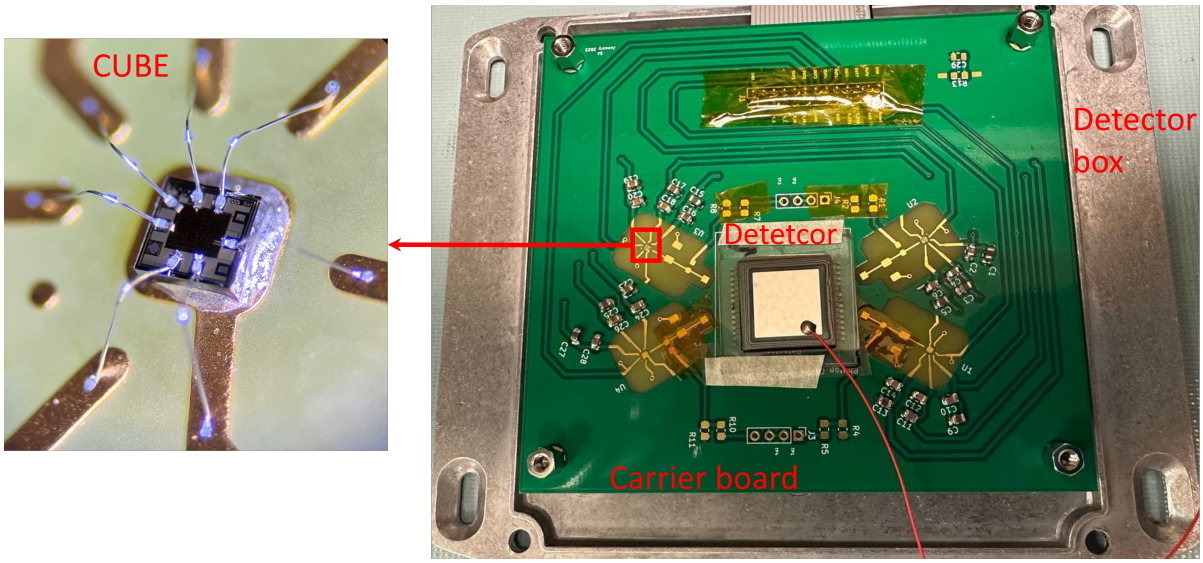


Figure 6.4: CUBE carrier board inside the detector box with a close-up view of CUBE bonding

Additionally, multiple carrier boards can be stacked on top of each other, enabling the capability to support multilayer detection, which is essential for high-energy applications. To optimize photon transmission through the carrier board, a rectangular cutout was integrated into the printed circuit board (PCB) design. This cutout acted as an aperture, facilitating the unhindered passage of photons with minimal attenuation. One carrier board can accommodate up to four CUBEs in total with two on each side of the detector to enable the dual-ended readout for two microstrips. For the proof of concept, we used two CUBEs to read out just one microstrip.

6.3.2 Results

It is expected that due to inherent leakage within the CUBE charge pre-amplifier, the output voltage shows a gradual ramp. During hole accumulation, the voltage ramp exhibits a downward trend, whereas electron accumulation leads to an upward ramp. There are two approaches for resetting the preamplifier: one involves selecting a threshold value, such that if any of the CUBEs reaches this threshold, a reset is generated. The alternative method employs a periodic reset, either internally or externally. In our setup, the CUBEs operate through a periodically synchronized external reset shared among all CUBEs on the board. This reset discharges all accumulated charges on the feedback capacitor and the signal level comes back to the initial set voltage.

We investigated the response of the CUBE setup in the absence of any detector. This step was taken to validate the accurate functionality of the CUBEs, an important step especially after the CUBEs being wire bonded to the board. As depicted in Figure 6.5, the response of the CUBEs without any associated detector shows a ramp response. Notably, a mismatch between the two CUBEs is observed. Specifically, one of the CUBEs demonstrates a more pronounced leakage and in the electron collection mode and the other one shows less leakage but in hole collecting mode.

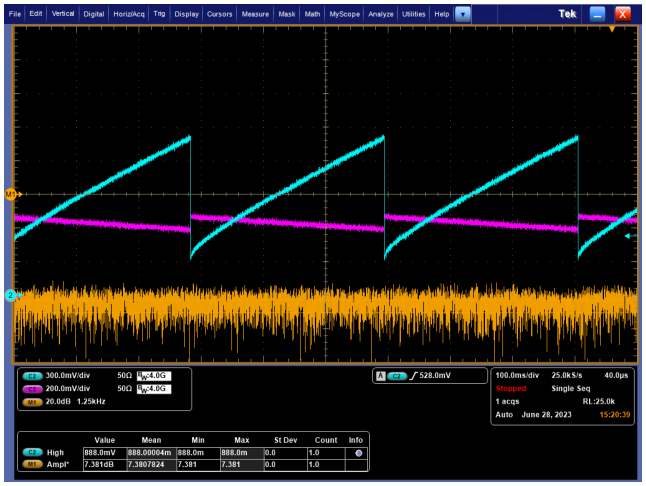
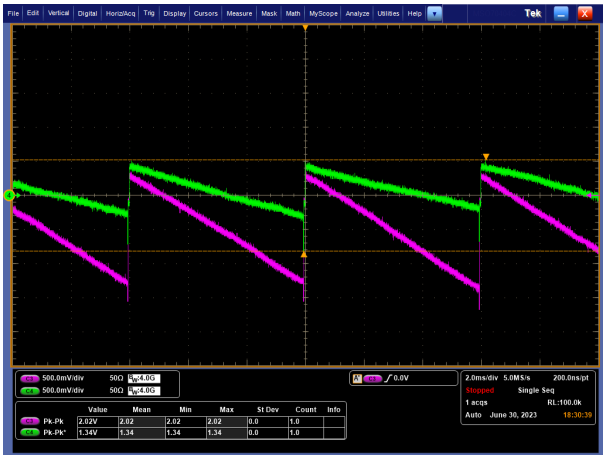


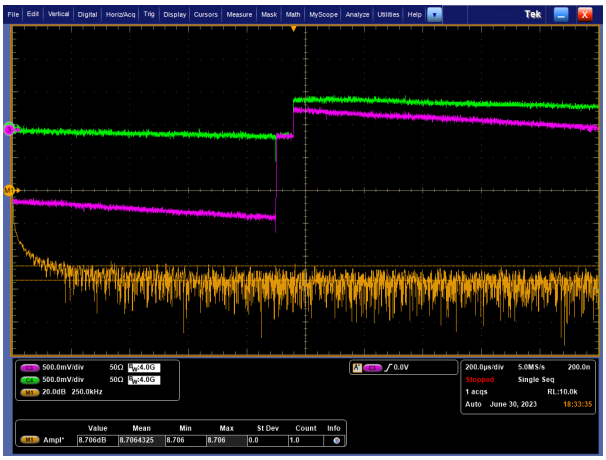
Figure 6.5: Signals from two ends of a single microstrip for the setup without any detector attached and showing the FFT of the signal, an indication of noise level.

Incorporating the detector and applying a high voltage introduced dark current into the system. The holes injected from the top electrode traveled toward the bottom microstrips

and went through charge division. Given the uniformity assumption of dark current across a single microstrip, it followed that half of the dark current passed through each CUBE in summation. As illustrated in Fig. 6.5, both CUBES were in the hole collection mode due to the presence of dark current. The CUBE displaying a lower signal level, indicated by the green color, corresponds to the CUBE with electron leakage as depicted in Figure 6.5 using the blue color. The FFT analysis of the signal clearly indicates that introducing the detector along with HV, contributes slightly to system noise.



(a)



(b)

Figure 6.6: (a) Signals from two ends of a single microstrip for the setup with detector biased at $10V/\mu m$ without any gamma source (b) zoomed-in on the reset section of the signal and showing the FFT of the signal.

Subsequently, we employed ^{241}Am to assess the capability of the detector with resistive microstrips for photon detection. A collimator was utilized to focus the signal onto a 1 mm^2 area. However, even after several hours, we were unable to detect any photons. Consequently, we removed the collimator to increase the number of photons and the likelihood of their absorption. Detected photons appear as jumps in the preamplifier's output and the signal would look like a staircase. This occurs due to the absence of a feedback resistor,

setting it apart from the decay characteristics observed in CoolFET systems. Figure 6.7 illustrates the photon detection achieved through the setup, showing a single channel or one end of the microstrip. In this figure, the blue signal represents the output of the shaping amplifier, which both amplifies and extends the jump in the CUBE's response.

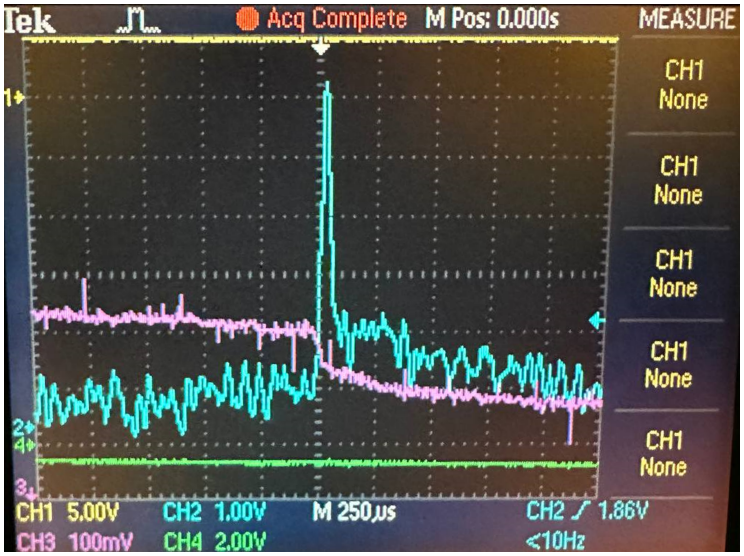


Figure 6.7: Capture of single photon using ^{241}Am source and CUBE setup. The green signal shows the output of one of the CUBEs and the blue signal is the output of shaping-amplifier.

Since we have removed the collimator, our expectation is to observe a consistent profile spanning from very low energies up to 59.9 keV. Following this point, a decline in the photon counts is anticipated. This behavior arises due to the potential absorption of photons near the opposite end, resulting in a notably reduced signal level at this particular microstrip end. As we assume uniform photon absorption across the microstrip, this variation leads to distinct charge divisions, consequently yielding signals of varying intensities. Fig. 6.8 demonstrates the PHS results from MCA for when the source is not present and when it is present and in Fig. 6.8(d) shows the corrected PHS signal by subtracting the dark PHS. The PHS results confirm our expectation and prove that this detector configuration is capable of detecting photons through charge division.

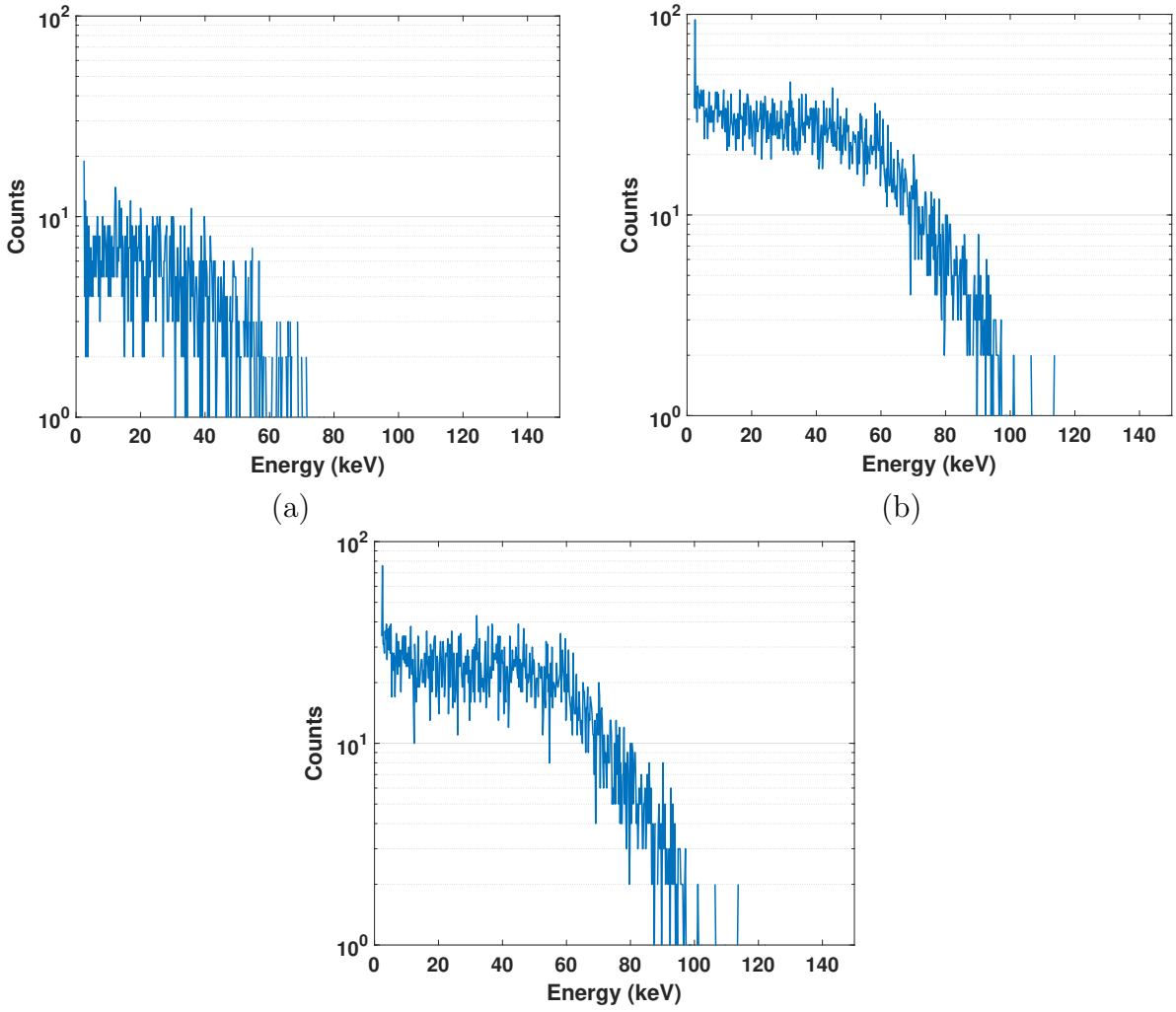


Figure 6.8: PHS results for (a) no ^{241}Am gamma source present to demonstrate the background noise (b) ^{241}Am gamma source is present and (C) the corrected data with the ^{241}Am gamma source present.

The subsequent phase involved the utilization of a dual-channel shaping amplifier to simultaneously display both channels. For the purpose of simultaneous signal shaping, amplification, analysis, and acquisition of Pulse Height Spectroscopy (PHS) results, the output of the bias board was linked to the XIA Pixie-Net multi-channel digital spectrom-

eter, which accommodates four channels.

Following the successful photon detection by the detector, an electrical arc occurred that impacted the setup. Due to the CUBEs being bare dies without ESD protection, they ceased functioning. Although another board was populated and subjected to testing, the newly integrated CUBEs exhibited substantial leakage. Furthermore, during the process of attaching the detector, these CUBEs incurred damage, preventing the replication of the observations made with the initial board. This particular phase of the experiment remains ongoing and forms a segment of our future research endeavors.

6.4 Conclusion

In this chapter, we prepared a photon counting setup utilizing the CoolFET preamplifier and conducted measurements on the conventional a-Se detector with two different gamma sources. The aim was to obtain PHS results and confirm the functionality of the setup. Subsequently, we investigated the response of the new design incorporating a resistive microstrip within the same setup. However, due to excessive noise, photon detection could not be achieved.

To overcome this problem, we substituted the CoolFET preamplifier with the CUBE preamplifier, recognized for its ultra-low noise features. Furthermore, we designed a PCB board to support multiple preamplifiers, facilitating the incorporation of the dual readout necessary for our design. Our experiment resulted in the successful capture of photons and the PHS was obtained for uniform gamma radiation over a single microstrip. Although the PHS setup was damaged, we had previously demonstrated charge division via optical source sweeping as seen in Chapter 4.

Chapter 7

Potential methods for improving temporal resolution

In Chapter 2, we identified two limitations associated with a-Se detectors: low radiation stopping power and poor temporal resolution. To address the stopping power issue, we proposed a solution involving a multilayer structure with a resistive microstrip readout mechanism to reduce the readout complexity. Furthermore, subsequent chapters delved into the introduction of a novel hole-blocking bilayer configuration, intended to enhance detector response for improved photon detection capabilities shown in the previous chapter. This chapter explores the second concern, low temporal resolution, and presents two distinct methods for a solution along their preliminary and simulation-based results.

Temporal resolution in amorphous semiconductors like selenium is adversely affected by the low mobility of electrons. Consequently, the enhancement of electron mobility must be achieved either through material structure modification or by reducing the impact of electron mobility on the detector response. The first approach discussed in this chapter involves substituting a-Se with crystalline selenium (c-Se) in the detection region. This approach utilizes higher carrier mobility of c-Se attributed to its crystalline structure. The second method involves employing unipolar charge sensing techniques such as Frisch grids into the detector's design, merging principles from drift detectors and resistive microstrips. This integration of unipolar charge sensing and reduction of capacitance can potentially result in the improvement of temporal resolution.

7.1 Crystalline selenium

The primary method for crystallizing amorphous selenium involves annealing the sample. Annealing can be achieved through either thermal heating or laser-induced heating. Given that the excimer laser at the G2N facility is intended for silicon and considering the risk of selenium material contaminating other devices, thermal heating was utilized to crystallize a-Se. To determine the temperature at which a-Se begins to transition into c-Se, its differential scanning calorimetry (DSC) is required. DSC demonstrates the difference in the amount of heat needed to raise the temperature of a sample compared to a reference, shown as a function of temperature. Notably, significant variations in heat capacity occur during phase transitions. Fig. 7.1 provides the DSC curve for the a-Se core within the optical fiber [12].

Among the notable temperatures, the values of T_g, T_x, and T_p are of significance, standing at 42°, 80°, and 92° correspondingly. T_g is the glass transition temperature, T_p is the peak temperature for crystallization and T_x signifies the initiation point of crystallization for a-Se. Considering that a-Se exists as an unstable glass, a mixture of a-Se and c-Se may be present in the vicinity of T_x. The data in Fig. 7.1(b) confirms the temperature at which the transition from a-Se to c-Se occurs. In the context of Raman spectroscopy, a-Se displays a peak around 250 cm^{-1} whereas c-Se's peak is positioned at approximately 230 cm^{-1} [86].

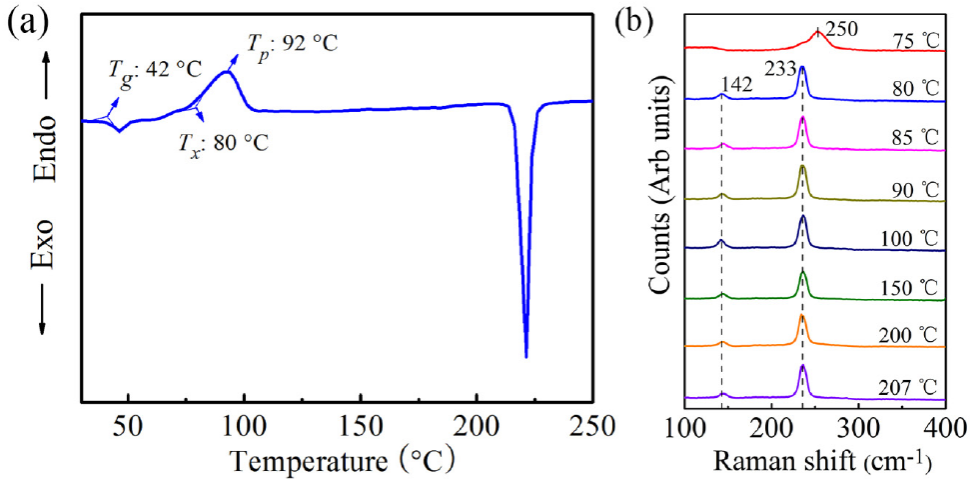


Figure 7.1: DSC curve of a-Se core [12].

As previously mentioned, a-Se initiates crystallization at temperatures exceeding 80°C.

However, at temperatures surpassing this threshold, the crystal's structure can exhibit variations in terms of grain size and boundaries. Numerous studies have investigated the crystallization of a-Se and its application as a photoconductor. The majority of these studies involve subjecting a-Se to air annealing at 200°C for a duration of one minute [87, 88, 89, 90, 91, 92]. The primary objective in this section is to consistently achieve crystallization of a-Se.

7.1.1 Setup

To crystallize a-Se, a setup is established to prevent contamination and health hazards at higher temperatures. This setup includes a main chamber with two openings: the lower one allows nitrogen gas to enter, while the upper one lets nitrogen and potential particles exit. The nitrogen used is of high purity, at 99.999%, and the system's output is connected to a fume hood. The hotplate is calibrated and programmed before the annealing process to ensure accurate result reporting and to prevent errors.



Figure 7.2: Crystallization setup used in thermal annealing

The initial step involves employing lower temperatures combined with extended duration. Notably, there exist studies involving the utilization of c-Se as an optical fiber,

wherein a temperature of 90°C was applied for a duration of 1 hour [12]. We experimented with this specific temperature and duration using a sample comprising a 1μm layer of a-Se deposited onto an ITO glass substrate. The ITO glass underwent a cleaning process involving acetone and isopropyl alcohol in an ultrasonic bath, and it was prepared for use in a dedicated thermal evaporation machine intended for a-Se deposition.

It is worth highlighting that the selenium pellet used in this procedure is different from the conventional ones employed for a-Se deposition. Typically, pellets utilized for a-Se deposition contain impurities like Arsenic (As) and Chlorine (Cl). The As helps in reducing the crystallization, enhancing the stability of a-Se, while Cl minimizes traps introduced by As. However, given our objective of inducing a-Se crystallization, the use of As impurities becomes counterproductive. Therefore, the pellets utilized here are of exceedingly high purity, reaching 99.9999% (metal basis) selenium.

7.1.2 Results

One of the challenges encountered while producing a c-Se film was delamination during the annealing process. To address this issue, Imura et al. employed an underlayer in their work [87, 88, 89, 90, 91, 92]. This underlayer not only serves to prevent delamination but also functions as a seed layer for crystallization, thereby offering a means to influence the characteristics of the resulting c-Se film. Experimenting with a selection of materials including PI, Parylene C, Al, and Au revealed that Au yielded superior outcomes in both minimizing delamination and ensuring uniform crystallization. The samples featuring Au as the underlayer are depicted in Fig. 7.3, wherein the left image represents the sample prior to annealing, while the right one shows the sample post-annealing. Notably, the initially deposited thin layer of a-Se presents a red color, which is expected to undergo a transformation to gray following the annealing process [90]. The results confirm the successful crystallization of a-Se.

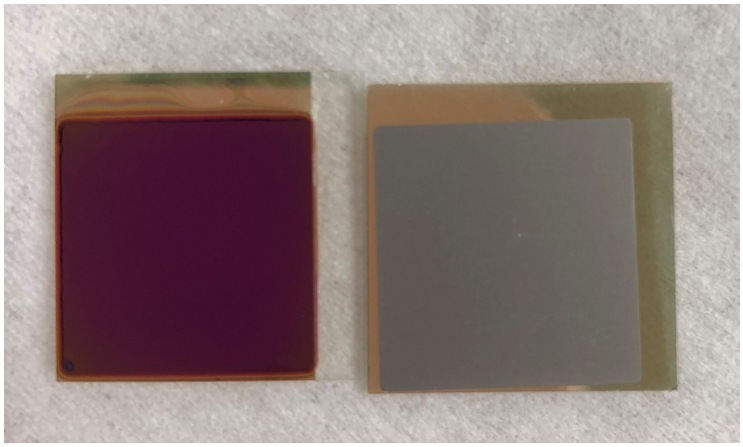
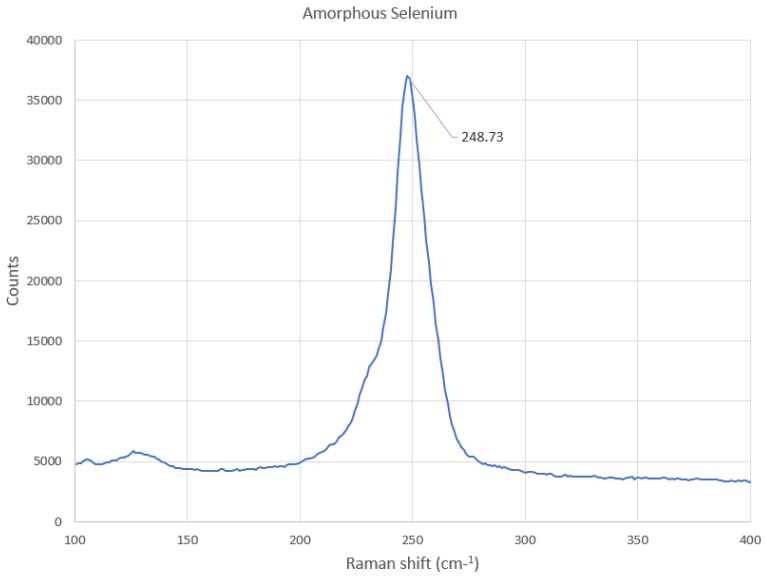
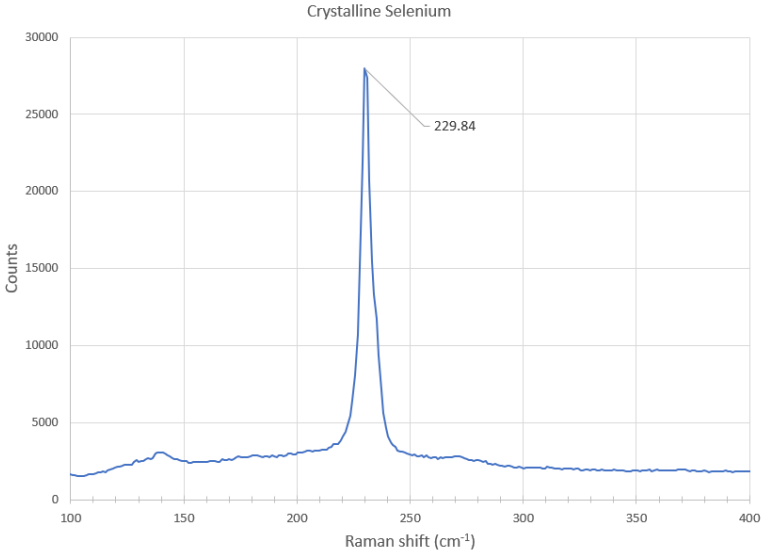


Figure 7.3: A. x250 zoom

In addition to the change in coloration, validation of the results is supported by SEM images and Raman experiments. As shown in Fig. 7.4a, the Raman spectra of a-Se indicate a dominant peak at 248.73 cm^{-1}, in close proximity to 250 cm^{-1}, confirming the amorphous nature of the sample. However, a slight broadening is noticeable around 230 cm^{-1}. This could be attributed to the inherent instability of a-Se; without As impurities, there exists a chance that a small portion of a-Se might undergo crystallization. Fig. 7.4b displays the Raman spectra of annealed a-Se, clearly illustrating the transition from its amorphous state. The peak has shifted to 229.884 cm^{-1}, closely resembling the 230 cm^{-1} mark which corresponds to the c-Se peak.



(a) Before annealing

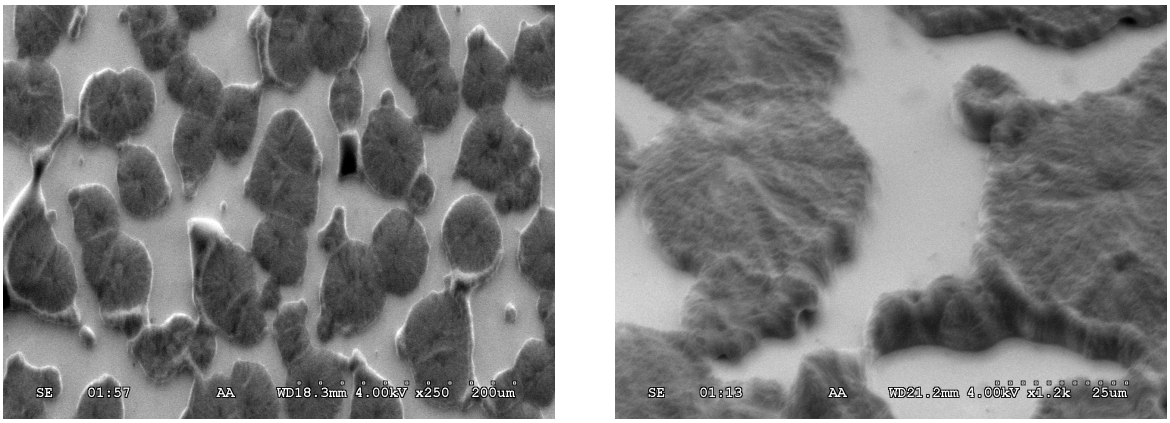


(b) After annealing

Figure 7.4: Raman spectroscopy for a-Se film before and after annealing

To investigate the changes occurring within a-Se, a SEM image was captured. In Fig. 7.5, numerous small islands can be observed, corresponding to c-Se regions. However,

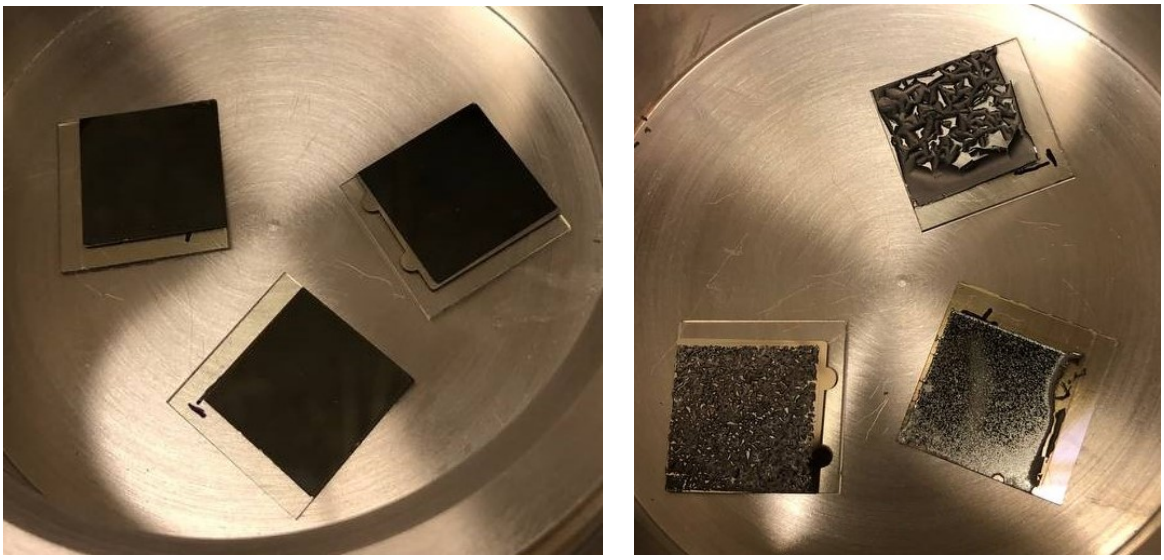
the uniformity of these islands is suboptimal, with gaps between them containing a-Se. For samples with a 1μm thickness, these gaps are primarily devoid of selenium, leading to the exposure of the underlying gold layer. To tackle the issue of exposed gold between islands, a 2μm layer of a-Se was employed. This led to improved uniformity while covering all the gold. Further efforts were focused on creating a thicker c-Se layer. However, when the thickness was increased to 12μm, only partial crystallization occurred.



(a) x250 magnification (b) x1.2k magnification

Figure 7.5: SEM image of c-Se showing the islands of crystallization

To achieve greater thicknesses of c-Se, one potential approach involves raising the temperature or extending the duration. Another concept worth considering is the sequential crystallization of 2μm layers, followed by deposition and crystallization. This would introduce additional complexity to the process. Additionally, another strategy is the use of Te as the underlayer. Our exploration focused on crystallization using a thin Te underlayer. After depositing a-Se, it underwent annealing at 180°C for 3 to 5 minutes. Unfortunately, a significant number of samples experienced delamination, as depicted in Fig. 7.6. However, more promising results were observed when working with flexible PET material. In this case, c-Se formed with satisfactory quality as illustrated in Fig. 7.7, indicating a potential method for applying c-Se on flexible substrates.



(a) (b)

Figure 7.6: a-Se samples with Te interlayer (a) before annealing and (b) after annealing.

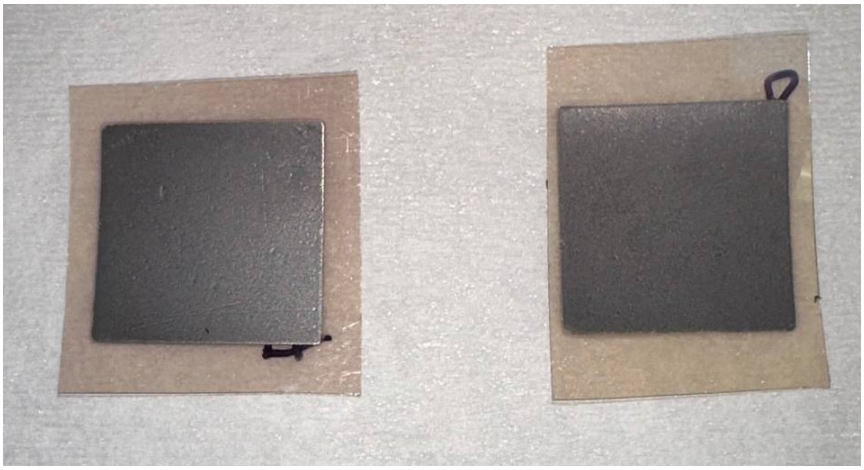


Figure 7.7: 12 μm c-Se samples on a flexible PET substrate

The characterization was continued with a 2µm-thick c-Se sample without Te, utilizing gold as both the electrode and underlayer. The main disadvantage of a crystalline photoconductor is the high dark current, which needs to be addressed by exploring different

blocking layers. Here, we encountered the difficulty of not having a PI layer underneath that is typically used to prevent crystallization. Consequently, a blocking layer was required on top. However, due to the PI curing temperature (350°) being beyond the melting point of a-Se, we were unable to use PI. Instead, Parylene C was applied to the top surface of a-Se, and dark current measurements were conducted.

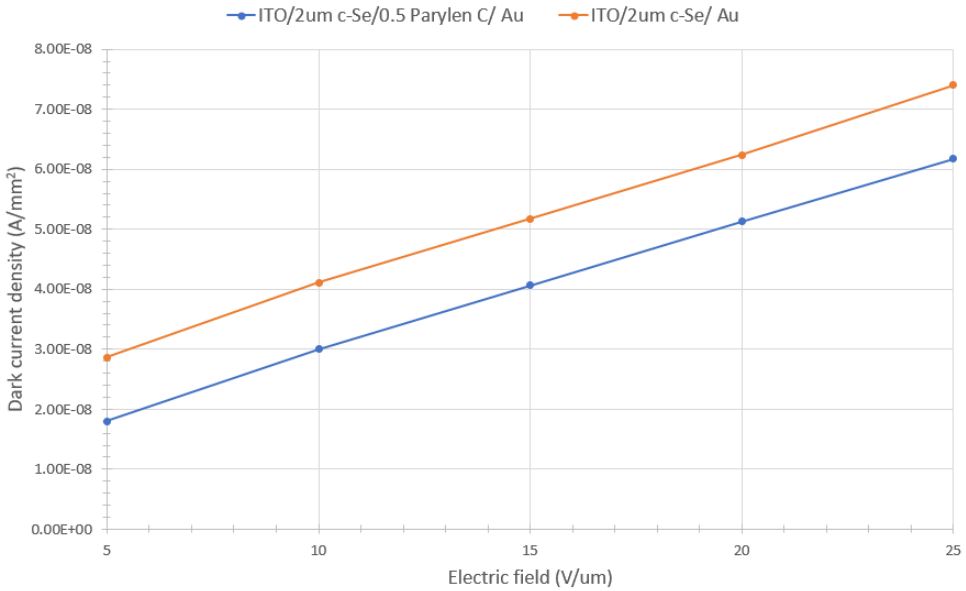


Figure 7.8: Dark current for two c-Se detectors one without hole blocking layer and one with 0.5μm Parylene c

Two samples were fabricated, both with ITO glass as the substrate and gold as the underlayer. Subsequently, a 2µm-thick layer of a-Se was deposited, and the devices underwent annealing at 90° for 1 hour to achieve approximately 2µm of c-Se. One of these devices lacked a hole-blocking layer, while the other incorporated Parylene C as a top hole-blocking layer to prevent charge injection from the top electrode.

Preliminary results, as depicted in Fig. 7.8, indicated that Parylene C exhibited behavior like a resistor, making it impractical for use as a hole-blocking layer in a-Se detectors. The main advantage of Parylene C was its deposition at room temperature. Another candidate could be SU-8 or the new hole-blocking bilayer configuration which was explored in earlier chapters. The continuation of this project, substituting a-Se with c-Se, has been left for future work with a focus on implementing a suitable hole-blocking layer (such as

SU-8) and conducting a comprehensive characterization of the devices to assess mobility, lag, and sensitivity.

7.2 Selenium-Based Drift Detector

In this section, we introduced a new detector structure, a selenium-based drift detector, that was proposed to enhance temporal resolution. To gain a more comprehensive understanding, it is essential to explore deeper into the topic of drift detectors. Semiconductor drift detectors were proposed in 1983 by Gatti and Rehak with the idea of having a semiconductor detector similar to gas chamber drift detectors for particle tracking.[93] Employing microstrip detectors for this application was complicated due to the large number of readout channels to achieve high spatial resolution. The first structure proposed for silicon drift detector (SDD) had only one readout channel, and the drifting field was created by applying a linear potential to strip arrays on both sides of the detector.[94]

In this 1D position-sensitive device, the location was determined by recording the drift time of carriers. Later, different structures were developed to realize 2D position sensitivity, such as segmentation of the readout electrode in microstrip drift detectors and segmentation of the back-plane electrode in cylindrical drift detectors.[94, 95] SDDs are mainly used to precisely resolve low-energy X-ray lines due to their high count rate and high energy resolution. The detection area in the SDD is significantly larger than the readout electrode, resulting in very low capacitance hence lower electronic noise. This allows for a shorter peaking time while maintaining high energy resolution to increase the photon count rate. However, silicon has a low detection efficiency for energies above 20 keV, so high Z materials were combined with drift detector structures to achieve high detection efficiency, high energy resolution, and high count rate. A simple drift strip detector was proposed for CZT in 1998 [96]. That structure comprises multiple cells with drift strips between collecting electrodes on one side and a planar electrode on the other. Kuvvetli proposed segmented planar electrodes orthogonal to the direction of strips to realize position sensitivity along the strips.[97]

Another candidate to overcome the detection efficiency of SDDs is amorphous selenium (a-Se) which is widely used in large-area flat panel detectors for X-ray imaging. This is attributed to the fact that a-Se has a high spatial resolution and a well-established, cost-effective fabrication process for large-area applications. However, it suffers from low electron mobility, which degrades charge collection efficiency, energy resolution, and count rate capacity. Different techniques were implemented to minimize the effect of low electron mobility, such as employing unipolar charge sensing by embedded Frisch grids.[98, 99]

As a simple alternative solution, we propose developing a drift detector structure for a-Se detectors. The drift detector can potentially reduce the sensitivity of the collecting electrodes to slower charge carriers by leveraging unipolar charge sensing; also, it increases the detection area ratio to the collecting electrode area and lowers the electronic noise. In order to achieve 3D position sensing in the proposed drift detector and reduce the electronics complexity, we employ a more straightforward readout circuit design based on the resistive charge division method. The resistive charge division method has been most commonly used for gaseous detectors, and in past decades it has been adopted in semiconductor detectors as well. In charge division readout, the charge induced by an absorbed photon is divided along the resistive layer or strip depending on the photon absorption location, and the charge is collected from both ends. Radeka, in 1974, was the first to report on the characteristics of charge division in resistive microstrips. [68]. In 2012, Bassignana fabricated a resistive silicon microstrip detector, and the results were promising for use in colliders [69]. In this work, we introduce novel structures for a-Se drift detector (ASDD) to achieve a uniform drifting field potential with 3D position sensing.

7.2.1 Materials and Methods

A 3D model was developed with the finite element method in COMSOL for structures discussed in this work. The electric field and potential were simulated for a cross-section of the detector. To investigate the feasibility of having a-Se drift detector and its advantages, first, we start with a conventional microstrip structure with the planar electrode on the other side, as shown in Fig. 7.9a. The microstrip pitch is chosen to be similar to the collecting microstrips in the drift detector. To compare its electric field in bulk with the drift structure, we considered a line orthogonal to the direction of the strips and in the middle of selenium along which to plot the electric field. As illustrated in Fig. 7.9b electric field between collecting electrodes reaches near zero resulting in loss of the spatial resolution unless we increase the number of strips.

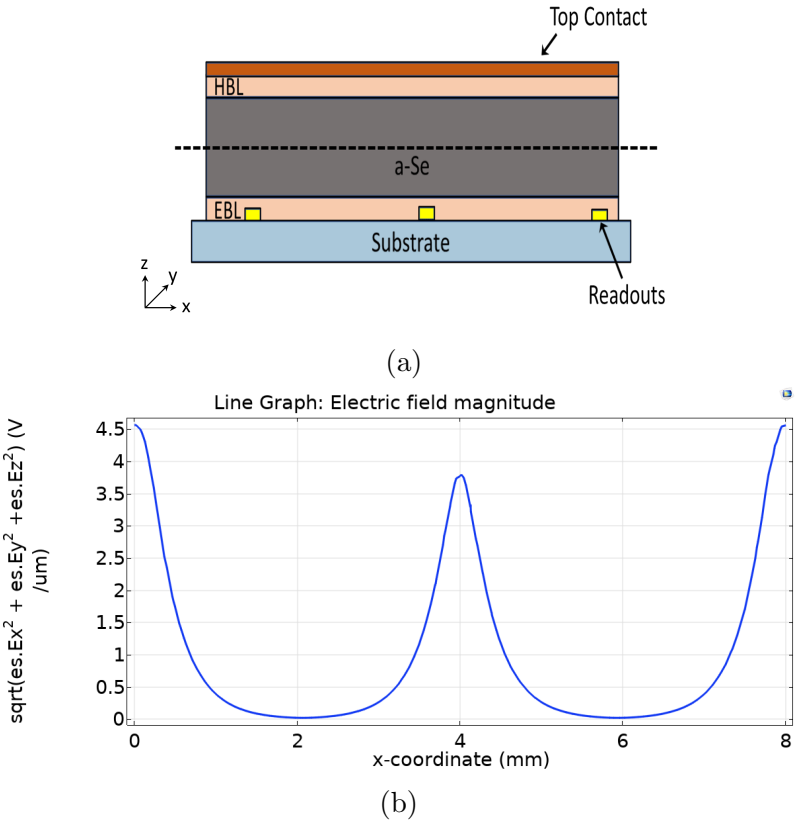


Figure 7.9: Illustration of (a) side view of a conventional micro strip detector with planar top contact, (b) Electric field magnitude along the detector width in the middle of a-Se and perpendicular to the direction of strips.

To increase the spatial resolution and energy resolution without increasing the number of collecting electrodes, we propose the drift detector structure demonstrated in Fig. 7.10. The readout microstrips are placed at the bottom of the detector with parallel drift strips on both sides of the detector (D_1 to D_n). The strips used on the top side and above the readout electrodes (noted as "B") are larger and have higher voltage values compared to the adjacent microstrips to shape the field toward the collecting electrodes. Photon detection and charge generation can occur in the vertical direction (face-on illumination) or the lateral direction (edge-on illumination), with the charge carriers drifting in the lateral direction. In order to obtain 3D position sensing, we propose implementing a charge division readout employing resistive collecting electrodes. The proof of concept for a-Se

position-sensitive microstrip detector employing the charge division technique is fabricated and discussed in this work. Utilizing resistive readout microstrips further reduces the number of readout channels and improves the energy resolution of a-Se detectors. Moreover, in face-on illumination geometry, by reducing the number of readout channels, stacking the a-Se drift detectors can be performed in a simpler manner, keeping it a cost-effective alternative for gamma photons detection applications, while in edge-on illumination, it can be a cost-effective alternative for small area detection applications that require low dose irradiation and higher detection efficiency.

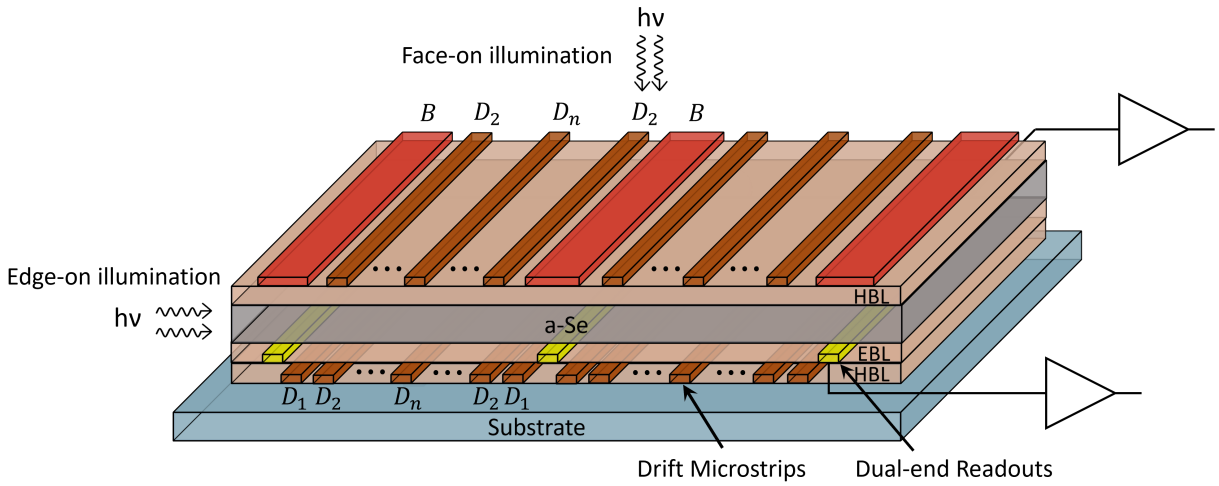


Figure 7.10: 3D view of the proposed structure for a-Se drift detector utilizing resistive collecting electrodes and dual end readout.

In charge division readout, both ends of the strip must be read simultaneously, and the ratio of the signals gives the location of impact along the strip direction. Also, the ratio between the collecting electrode and the strips on the other side of the detector gives information about the third coordinate of impact location. One readout is sufficient for all the top microstrips to get the triggering for drift time calculation and signal ratio to get the depth of interaction. Another possible design, simulated in this work, is to use one planar high-voltage top electrode instead of microstrips (Fig. 7.11).

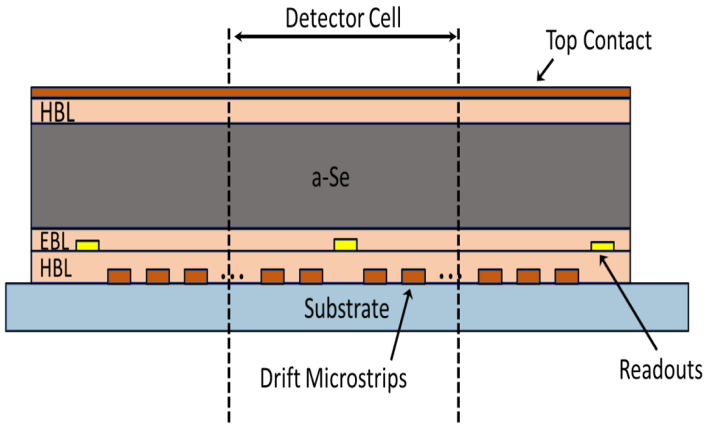


Figure 7.11: Side view of a-Se drift detector with high voltage planar top electrode

In silicon drift detectors, the field shaping is dependent on the voltage steps and controlled by depletion regions near rectifying contacts which are formed by different doping concentrations. These regions prevent the charge carriers from trapping near the drifting strips. On the other hand, in CZT detectors, there is no depletion region controlling the shape of the field, so the field shaping solely depends on the voltage steps. In CZT drift detectors, the drifting microstrips are not embedded in the structure and are coplanar with collecting microstrips. However, in this proposed a-Se drift detector, the drifting microstrips are embedded in the structure and are not in the same plane as the collecting microstrips. The embedded structure reduces the charge injection and trapping near the drift microstrips.

In the COMSOL model, an entire cell with a half cell on each side was simulated with microstrips at the top, as shown in Fig. 7.10. Thirteen drifting microstrips per cell were considered for the bottom of the detector, twelve of them having a matching parallel strip on the top of the detector with a 250 V reduction step in their values along the drift direction starting from 3500 V at the edge of a cell. Different numbers of microstrips can be used depending on the application and required spatial and energy resolutions. The geometry properties used in COMSOL are listed in Table 7.1.

Table 7.1: COMSOL Model - Geometry Parameters

Parameter	**Value**
Detector size	$8mm \times 8mm$
Detector cell size	$3.9mm \times 8mm$
Drift/collecting microstrip size	$100\mu m\times$ 8 mm
Top contact microstrip size	$200\mu m\times$ 8 mm
Gap between drift microstrips	$50\mu m$
a-Se thickness	$500\mu m$
Microstrip thickness	$100nm$
HBL thickness	$2\mu m$
EBL thickness	$1\mu m$
Substrate thickness	$40\mu m$

In this work, we simulated the electric field and potential distribution in an a-Se detector with a three readout microstrip structure. The focus is on the middle electrode (cell), and the two distal end electrodes were implemented to consider their effect on the field shaping of the middle cell.

7.2.2 Simulation results

The electric potential and field simulation results for the two proposed designs are shown in Fig. 7.12 and Fig. 7.13. The design with planar top contact creates an electric potential valley, so holes generated in bulk drift toward the collecting electrodes. However, in this design, further away from collecting electrodes, the probability of holes moving directly toward one of the microstrips and getting trapped is high according to the electric field lines (referred to as streamlines in COMSOL).

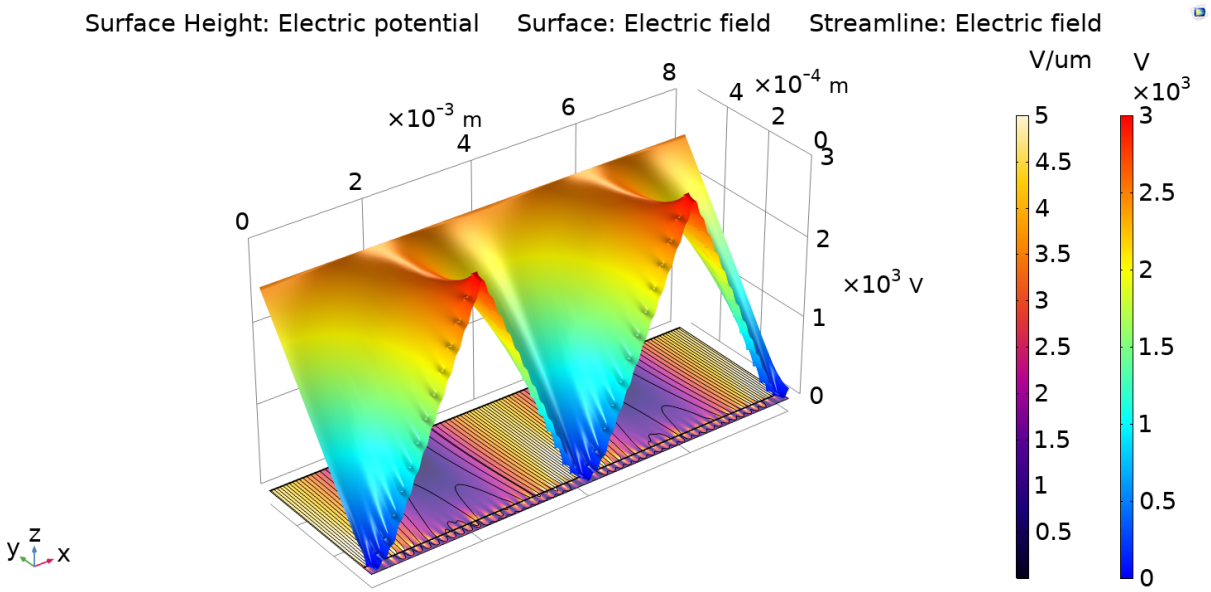


Figure 7.12: Electric field and potential for a cross section of the drift detector with planar top contact.

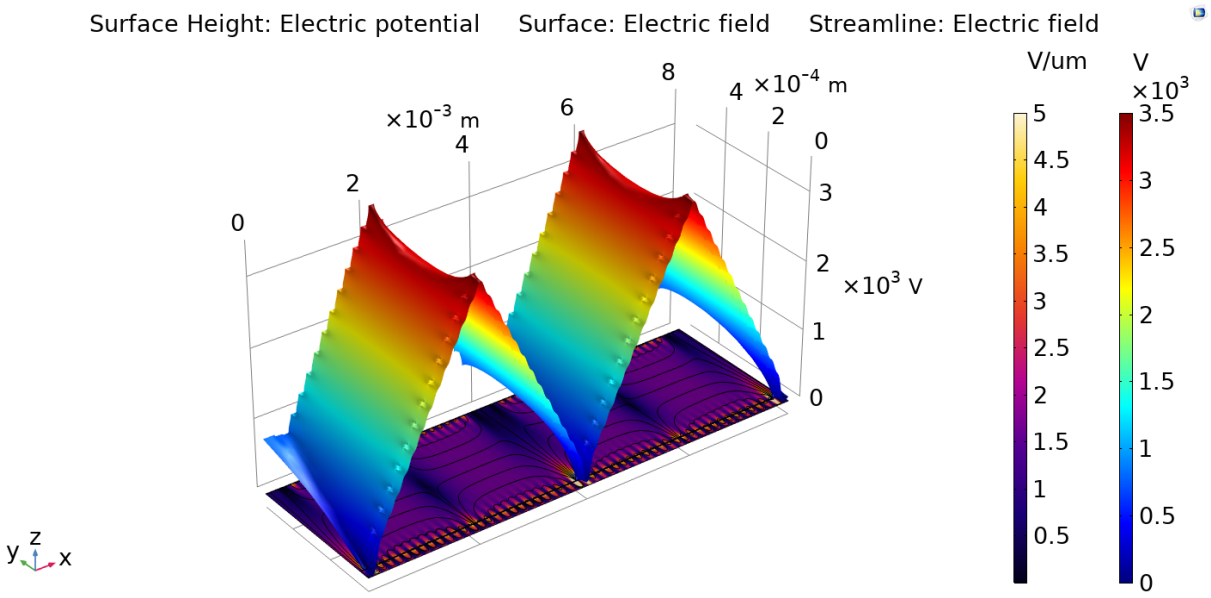


Figure 7.13: Electric field and potential for a cross section of the drift detector with parallel microstrips on both sides.

To overcome this issue, we place drift microstrips on both sides of the detector to drift holes smoothly toward the center of the detector cell. The top contact at the center of the cell, with a higher voltage than its neighbors, is responsible for drifting the holes toward the collecting electrode. Therefore, parallel microstrips on both sides and top contacts at the center of the detector cell help reduce the probability of charges being trapped between adjacent strips and ensure a uniform electric field in the drift area, as shown in Fig. 7.14.

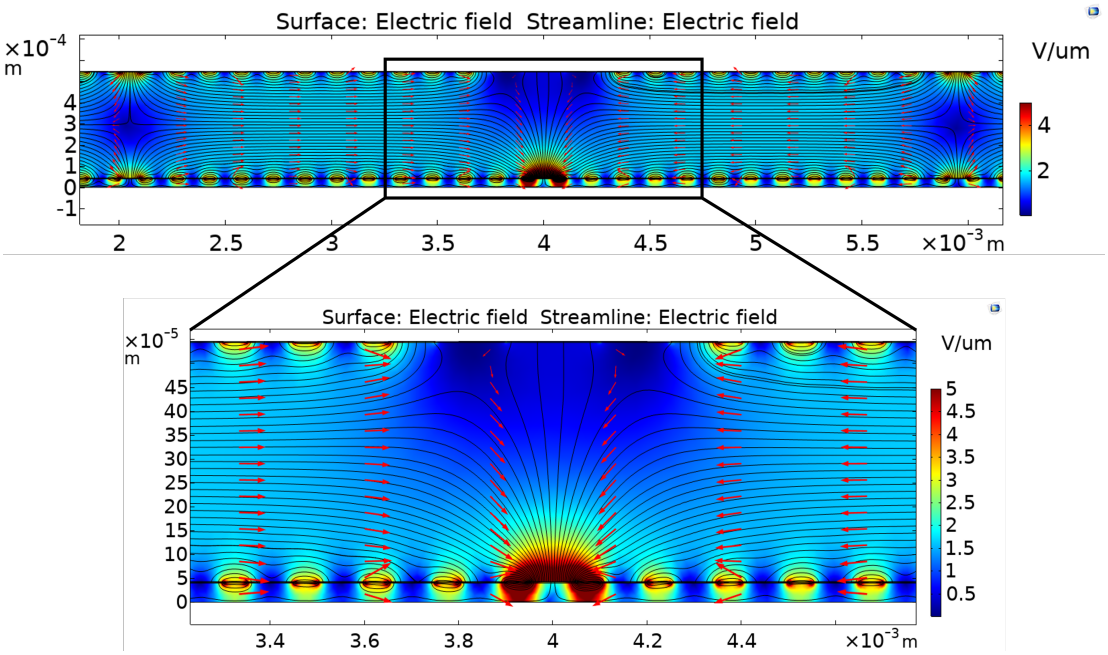


Figure 7.14: Electric field magnitude and direction inside the detector with top contact voltage of 700V.

A parametric simulation was carried on to choose a voltage value for the top contact microstrip – noted as "B" in Fig. 7.10– and the result is illustrated in Fig. 7.15. 800 V shows more uniform fields near the collecting electrode (Fig. 7.14). For voltages below 800 V, the field is not strong enough to drift all charges toward the collecting electrode. For voltages above 800 V, two electric field valleys are created near the middle of the detector thickness in Fig. 7.16 which increases the chance of charges being trapped in those areas.

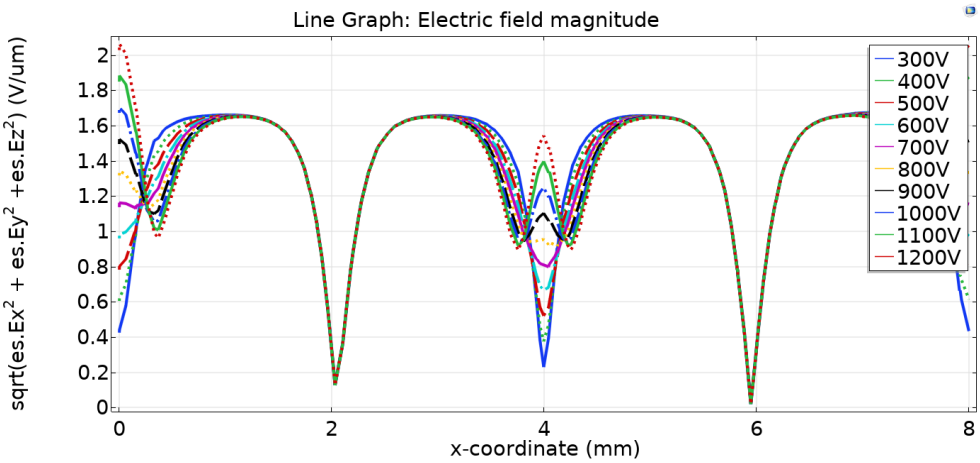
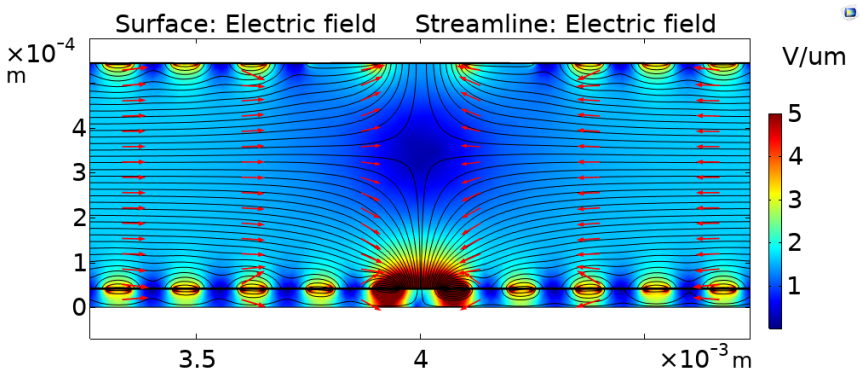
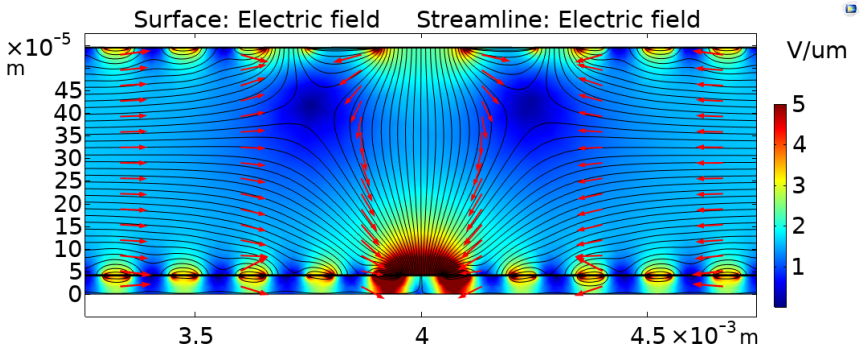


Figure 7.15: Electric field magnitude along the detector width in the middle of a-Se and perpendicular to the direction of strips for different values of top contacts



(a)



(b)

Figure 7.16: Electric field streamline for (a) $V_B = 400$ V (b) $V_B = 1200$ V.

This design with a uniform drift field ensures a high spatial resolution and also achieves unipolar charge sensing for carriers with higher mobility. Thus, it reduces the contribution of slow carriers on the signal resulting in higher temporal and energy resolution. The weighting potential is simulated to verify the unipolar charge sensitivity in Fig. 7.17. For a conventional planar electrode detector, the weighting potential is simply a linear function calculated based on the Shockely-Ramo theorem by assuming the potential of the anode is 1. Here, the potential of collecting electrodes was set to 1V, and other electrodes were grounded. The weighting potential distribution illustrated in Fig. 7.17 drops to zero in the vicinity of the collecting electrodes along the drift direction, verifying that no charge is induced on the collecting electrodes due to the movement of slow charge carriers.

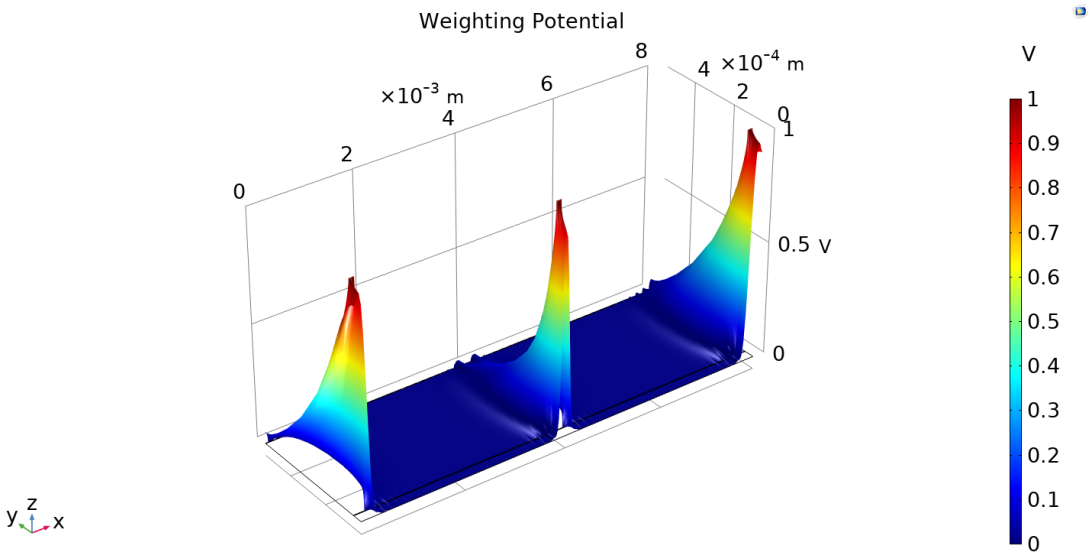


Figure 7.17: Illustration of weighting potential across the drift detector with collecting electrodes biased at 1V and other electrodes at zero.

7.3 Conclusion

In this chapter, we introduced two distinct approaches aimed at enhancing the temporal resolution of a-Se detectors, both supported by preliminary results and simulations. The first method involved the conversion of a-Se to c-Se using an Au intralayer, combined with a flexible substrate. The outcomes revealed elevated dark current, which resulted in exploring novel hole-blocking layer strategies.

In the second method, we presented the concept of a-Se drift detector in various configurations. In the proposed designs, we amalgamated the principles of resistive microstrips with drift detectors, strategically adjusting the simulated electric fields to ensure optimal field shaping. For the simulation, we considered thirteen drifting microstrips for each cell at the bottom of the detector, with twelve of these corresponding to parallel strips at the top of the detector. Notably, a reduction step of 250 V was implemented in their values along the drift direction. It is worth noting that the number of microstrips can be expanded based on the specific application requirements. Moreover, to enhance stopping power, materials with higher atomic numbers can be employed. This design appears quite promising and has the potential to extend to other amorphous or large-area semiconductors, including

organic materials.

Chapter 8

Conclusion and Future Work

8.1 Conclusion

Amorphous Selenium (a-Se) has demonstrated its suitability for X-ray imaging due to its cost-effective and well-established fabrication process, as well as its capability for large-area deposition. This study aimed to expand its utility to high-energy applications like Single Photon Emission Computed Tomography (SPECT), which operates within the energy range of 140 keV - 160 keV. The proposed strategy of employing a multilayer detector through detector stacking exhibited satisfactory detection efficiency without a significant compromise to spatial resolution, despite an increase in the number of layers. However, as the layer count increases, the complexity of reading out each detector layer also increases.

The implementation of a charge division readout mechanism utilizing resistive microstrips is less complex compared to conventional pixel-based or microstrip methods. Our approach was able to effectively locate the LED source with a resolution of 1 mm, a requirement for precise SPECT imaging while maintaining high linearity. To enable photon-level detection, efforts were directed at mitigating dark current by incorporating a low-temperature hole-blocking layer on the top surface of a-Se. The SU-8 layer along with the innovative bilayer configuration for hole-blocking effectively suppressed dark current without significantly compromising detector sensitivity, as observed with the well-known PI hole-blocking layer. The newly introduced bilayer hole-blocking configuration at the top, demonstrated exceptional lag performance below 0.5%, establishing the feasibility of employing a-Se detectors in dynamic imaging applications such as dynamic mammography tomosynthesis and fluoroscopy.

The innovative detector design, featuring resistive microstrip technology and the integration of the new hole-blocking bilayer, was incorporated into a photon-counting setup. The Pulse Height Spectra (PHS) analysis demonstrated the detector's capability to detect photons, with the charge division readout distributing charges between the two ends of a microstrip. A more in-depth exploration was conducted to enhance temporal performance, leading to study of the conversion of a-Se to crystalline Selenium (c-Se) and the development of an a-Se drift detector. Successful conversion to c-Se was achieved when the intralayer consisted of gold, or when the substrate was PET with an intralayer of Tellurium (Te). Simulation results for the new a-Se drift detector design indicated that precise voltage adjustments could shape the electric fields effectively, enabling unipolar charge sensing. In conclusion, these investigations demonstrate a-Se's potential for high-energy applications, provided existing limitations are systematically addressed.

8.2 Contributions

This study has provided contributions aimed at overcoming the limitations of a-Se for its utilization in high-energy radiation imaging applications. These contributions are summarized below:

- Examined the multilayer detector stack through simulations to assess the impact of layer count on MTF and DE.
- Developed two resistive microstrip structures, located at the top and bottom, to enable charge division readout.
- Successfully demonstrated the viability of charge division readout and analyzed the accuracy of LED source localization.
- Investigated the potential of employing a low-temperature organic hole-blocking layer on top of a-Se.
- Explored a hole-blocking layer suitable for seamless integration with CMOS or TFT processes in hole collecting mode, aiming for optimal performance.
- Compared the performance of the novel SU-8 hole-blocking layer with the well-established PI layer.
- Fabricated a hole-blocking layer comprised of Cs-doped a-Se and SU-8 and evaluated its characteristics.

- Quantified lag and ghosting across various configurations of hole-blocking layers.
- Executed TOF measurements to ascertain voltage drops across different hole-blocking layer configurations.
- Assessed the detector's response to pulsed X-rays, particularly relevant for applications like fluoroscopy operating at 30 frames per second.
- Configured two photon-counting setups with distinct preamplifiers for experimental comparison.
- Validated the capability of charge division readout in a-Se detectors to effectively detect photons.
- Proposed two solutions to address temporal performance issues inherent to a-Se detectors.
- Successfully transformed a-Se into c-Se, this was accomplished either with a gold intralayer on a glass substrate or Te on a PET substrate.
- Introduced the innovative concept of a-Se drift detectors, which combine drift detection principles with a resistive microstrip design.
- Employed simulations to visualize the weighting potential in the a-Se drift detector, demonstrating the feasibility of unipolar charge sensing.

8.3 Future work

The photon-counting setup requires adjustments to safeguard CUBEs against potential damage. To address the challenge of low photon counts, a radioactive isotope disk with substantial activity can be employed in conjunction with collimation. Another viable approach involves partnering with a hospital to conduct experiments utilizing radiotracers commonly employed in SPECT. By incorporating these modifications into the setup, it becomes feasible to explore the charge division readout and investigate position detection linearity, thus validating the detector's suitability for SPECT applications. Following this, the design's versatility is underscored as the carrier board is designed to facilitate stacking, enabling the stacking of multiple PCB boards with detectors. This stacking not only enhances detection efficiency but also provides an empirical validation of simulation-derived results.

In addressing temporal resolution, chapter 7 offers valuable methods. By utilizing approaches that have yielded successful results with c-Se, there is an opportunity to explore various hole-blocking layers, particularly the innovative hole-blocking bilayer which can reduce the dark current of the c-Se detector. This investigation can be further supported by comprehensive assessments that involve measuring photoresponse and pulsed X-ray response. Concurrently, the a-Se drift detector is still in its early stages, requiring a step-by-step fabrication process followed by extensive evaluations. These evaluations will cover aspects like position linearity, time resolution, and energy resolution.

8.4 Publications

Patent

- S. Adnani and K. S. Karim, "Selenium Drift Detector", US provisional filed, patent pending.

Journal publications

- S. Adnani, A. Pil-Ali and K. S. Karim, "A Low-Temperature Processed Organic Hole-Blocking Contact Layer for Amorphous Selenium X-Ray Photoconductor," in IEEE Electron Device Letters, vol. 44, no. 9, pp. 1528-1530, Sept. 2023, doi: 10.1109/LED.2023.3296332.
- A. Pil-Ali, S. Adnani, C. C. Scott, and K. S. Karim, "Direct Conversion X-ray Detector with Micron-Scale Pixel Pitch for Edge-Illumination and Propagation-Based X-ray Phase-Contrast Imaging," Sensors, vol. 22, no. 15, p. 5890, Aug. 2022, doi: 10.3390/s22155890.
- A. Pil-Ali, S. Adnani and K. S. Karim "Self-aligned multi-layer X-ray absorption grating using large-area fabrication methods for X-ray phase-contrast imaging." Sci Rep 13, 2508. 2023, doi: 10.1038/s41598-023-29580-2

Conference publications

- S. Adnani, A. Pil-Ali, C. Con, and K. S. Karim. "Investigation of position linearity in position-sensitive microstrip amorphous selenium-based detector." In Medical

Imaging 2022: Physics of Medical Imaging, vol. 12031, pp. 125-129. SPIE, 2022.

- S. Adnani, A. Pil-Ali, C. Con and K. S. Karim, "A Position-Sensitive Microstrip Detector using Amorphous Selenium Photoconductor," 2021 IEEE Nuclear Science Symposium and Medical Imaging Conference (NSS/MIC), Piscataway, NJ, USA, 2021, pp. 1-3, doi: 10.1109/NSS/MIC44867.2021.9875623.

- S. Adnani, A. Pil-Ali, C. C. Scott and K. S. "Monte Carlo simulation of an amorphous selenium-based multi-layer photon-counting detector for SPECT applications." In Medical Imaging 2021: Physics of Medical Imaging, vol. 11595, pp. 306-312. SPIE, 2021.

- Pil-Ali, Abdollah, Serena Qinyun Z. Shi, Sahar Adnani, Peter B. Noël, and Karim S. Karim. "Multimodal single-shot x-ray phase-contrast imaging using a high-resolution micropillar-based grating." In Society of Photo-Optical Instrumentation Engineers (SPIE) Conference Series, vol. 12463, p. 1246309. 2023.

- A. Pil-Ali, S. Adnani, P. Gavirneni, S. Shin, B. Sadeghimakki, M. Poudineh, W. Wong, and K. S. Karim. "Self-aligned fabrication of high-aspect ratio high-resolution X-ray gratings." In Medical Imaging 2022: Physics of Medical Imaging, vol. 12031, pp. 903-907. SPIE, 2022.

- A. Pil-Ali, S. Adnani, C. C. Scott, and K. S. Karim, "Direct Conversion X-ray Detector with Micron-Scale Pixel Pitch for Edge-Illumination and Propagation-Based X-ray Phase-Contrast Imaging," Sensors, vol. 22, no. 15, p. 5890, Aug. 2022, doi: 10.3390/s22155890.

- A. Pil-Ali, S. Adnani, C. C. Scott, A. Olivo, and K. S. Karim. "Single-Exposure, Single-Mask, Edge-Illumination X-ray Phase-Contrast Imaging Using a 7.8-µm Pixel Pitch Direct Conversion X-ray Detector." In 2021 IEEE Nuclear Science Symposium and Medical Imaging Conference (NSS/MIC), pp. 1-3. IEEE, 2021.

- A. Pil-Ali, S. Adnani, C. C. Scott and K. S. Karim, "A 7.8-µm Pixel Pitch Direct Conversion X-ray Detector for High-Resolution Intraoral Tomosynthesis Application," 2021 IEEE Nuclear Science Symposium and Medical Imaging Conference (NSS/MIC), Piscataway, NJ, USA, 2021, pp. 1-3, doi: 10.1109/NSS/MIC44867.2021.9875819.

- A. Pil-Ali, S. Adnani, C. C. Scott, and K. S. Karim. "Challenges of employing a high resolution x-ray detector in a coded-aperture x-ray phase-contrast imaging system." In Medical Imaging 2021: Physics of Medical Imaging, vol. 11595, pp. 1225-1232. SPIE, 2021.

- A. Pil-Ali, S. Adnani, C. C. Scott, and K. S. Karim. "Evaluation of edge-illumination and propagation-based x-ray phase contrast imaging methods for high resolution imaging application." In Medical Imaging 2021: Physics of Medical Imaging, vol. 11595, pp. 441-452. SPIE, 2021.

- A. Pil-Ali, M. Soltani, S. Adnani, M. Kayaharman, M. Poudineh, B. Cui, and K. S. Karim. "Improving adhesion quality of SU-8 to gold thin film for absorption grating fabrication in X-ray phase-contrast imaging." In Medical Imaging 2022: Physics of Medical Imaging, vol. 12031, pp. 913-918. SPIE, 2022.

- A. Pil-Ali, M. Soltani, S. Adnani, B. Cui, and K. S. Karim. "A novel multi-layer grating structure for X-ray phase-contrast imaging." In Medical Imaging 2022: Physics of Medical Imaging, vol. 12031, pp. 898-902. SPIE, 2022.

- R. Khalili, A. Pil-Ali, S. Adnani and M. A. Karami, "Employing Total Ionizing Dose Effect in PN-Junction Photodetectors Implemented in Standard CMOS Technology for Dosimetry Application," 2021 IEEE Nuclear Science Symposium and Medical Imaging Conference (NSS/MIC), Piscataway, NJ, USA, 2021, pp. 1-3, doi: 10.1109/NSS/MIC44867.2021.9875917.

References

[1] G. B. Saha. *Basics of PET Imaging*. Springer International Publishing, 2016.

[2] Bud J Fogal. *Electronic transport properties of stabilized amorphous selenium x-ray photoconductors*. PhD thesis, University of Saskatchewan, 2005.

[3] Safa O. Kasap. *Doped and Stabilized Amorphous Selenium Single and Multilayer Photoconductive Layers for X -Ray Imaging Detector Applications*, chapter 18, pages 715–779. John Wiley Sons, Ltd, 2022.

[4] Safa Kasap, Cyril Koughia, Julia Berashevich, Robert Johanson, and Alla Reznik. Charge transport in pure and stabilized amorphous selenium: re-examination of the density of states distribution in the mobility gap and the role of defects. *Journal of Materials Science: Materials in Electronics*, 26:4644–4658, 2015.

[5] H. Naito, T. Iwai, M. Okuda, T. Matsuhita, and A. Sugimura. Computer simulation study of tail-state distribution in amorphous selenium. *Journal of Non-Crystalline Solids*, 114:112–114, 1989. Proceedings of the Thirteenth International Conference on Amorphous and Liquid Semiconductors.

[6] SO Kasap, Viswanath Aiyah, A Baillie, and AG Leiga. X-ray induced hole trapping in electroradiographic plates. *Journal of applied physics*, 69(10):7087–7096, 1991.

[7] M Abkowitz and JM Markovics. Evidence of equilibrium native defect populations in amorphous chalcogenides from analyses of xerographic spectra. *philosophical Magazine B*, 49(3):L31–L36, 1984.

[8] Derek Mortensen, George Belev, Kirill Koughia, Robert E Johanson, and SO Kasap. Thickness dependence of electron transport in pure a-se photoconductive films. *Canadian Journal of Physics*, 92(7/8):629–633, 2014.

[9] GP Ceasar, M Abkowitz, and J WP Lin. Photoacoustic and xerographic investigation of the gap-state structure of a- s e: Comparison with a- s i: H. *Physical Review B*, 29(4):2353, 1984.

[10] H-Z Song, GJ Adriaenssens, EV Emelianova, and VI Arkhipov. Distribution of gap states in amorphous selenium thin films. *Physical Review B*, 59(16):10607, 1999.

[11] JH Hubbell and SM Seltzer. X-ray mass attenuation coefficients: Nist standard reference database 126. *National Institute of Standards and Technology, Gaithersburg, Maryland, USA*, 2004.

[12] S. Peng, G. Tang, K. Huang, Q. Qian, D. Chen, Q. Zhang, and Z. Yang. Crystalline selenium core optical fibers with low optical loss. *Optical Materials Express*, 7(6):1647–1651, 2017.

[13] Joao Seco, Ben Clasie, and Mike Partridge. Review on the characteristics of radiation detectors for dosimetry and imaging. *Physics in Medicine & Biology*, 59(20):R303, 2014.

[14] Kjell Erlandsson and Tomas Ohlsson. Positron emission tomography. *Monte Carlo Calculations in Nuclear Medicine: Applications in Diagnostic Imaging*, page 69, 2012.

[15] Harrell G Chotas, James T Dobbins III, and Carl E Ravin. Principles of digital radiography with large-area, electronically readable detectors: a review of the basics. *Radiology*, 210(3):595–599, 1999.

[16] Stefan Gundacker and Arjan Heering. The silicon photomultiplier: fundamentals and applications of a modern solid-state photon detector. *Physics in Medicine & Biology*, 65(17):17TR01, 2020.

[17] D Renker and E Lorenz. Advances in solid state photon detectors. *Journal of Instrumentation*, 4(04):P04004, 2009.

[18] Aleksey E Bolotnikov, Giuseppe S Camarda, Gabriella A Carini, Gomez W Wright, Douglas Scott McGregor, Walter McNeil, and Ralph B James. New results from performance studies of frisch-grid cdznte detectors. In *Hard X-Ray and Gamma-Ray Detector Physics VI*, volume 5540, pages 33–45. SPIE, 2004.

[19] A. E. Bolotnikov, J. Butcher, G. S. Camarda, Y. Cui, G. De Geronimo, J. Fried, R. Gul, P. M. Fochuk, M. Hamade, A. Hossain, K. H. Kim, O. V. Kopach, M. Petryk, E. Vernon, G. Yang, and R. B. James. Array of virtual frisch-grid czt detectors with

common cathode readout for correcting charge signals and rejection of incomplete charge-collection events. *IEEE Transactions on Nuclear Science*, 59(4):1544–1551, 2012.

[20] P. N. Luke. Single-polarity charge sensing in ionization detectors using coplanar electrodes. *Applied Physics Letters*, 65(22):2884–2886, 1994.

[21] P. N. Luke. Unipolar Charge Sensing with Coplanar Electrodes—Application to Semiconductor Detectors. *IEEE Transactions on Nuclear Science*, 42(4):207–213, 1995.

[22] Denny L. Y. Lee. Selenium detector with a grid for selenium charge gain. *Progress in Biomedical Optics and Imaging - Proceedings of SPIE*, 5745, 04 2005.

[23] O. Frisch. British atomic energy report. 65:BR–49, 1944.

[24] W. Shockley. Currents to conductors induced by a moving point charge. *Journal of Applied Physics*, 9(1):635–636, 1938.

[25] S. Ramo. Currents induced by electron motion. *Proceedings of the IRE*, 27(9):584–585, Sept 1939.

[26] A. H. Goldan. Unipolar charge-sensing for evaporated large-area solid-state photoconductors for digital radiography. 2012.

[27] Safa Kasap, Joel B Frey, George Belev, Olivier Tousignant, Habib Mani, Luc Laperriere, Alla Reznik, and John A Rowlands. Amorphous selenium and its alloys from early xeroradiography to high resolution x-ray image detectors and ultrasensitive imaging tubes. *Physica status solidi (b)*, 246(8):1794–1805, 2009.

[28] SO Kasap, M Zahangir Kabir, and JA Rowlands. Recent advances in x-ray photoconductors for direct conversion x-ray image detectors. *Current Applied Physics*, 6(3):288–292, 2006.

[29] Satoshi Tokuda, Hiroyuki Kishihara, Susumu Adachi, and Toshiyuki Sato. Preparation and characterization of polycrystalline cdznte films for large-area, high-sensitivity x-ray detectors. *Journal of Materials Science: Materials in Electronics*, 15:1–8, 2004.

[30] KS Shah, RA Street, Y Dmitriyev, P Bennett, L Cirignano, M Klugerman, MR Squillante, and G Entine. X-ray imaging with pbi2-based a-si: H flat panel detectors. *Nuclear Instruments and Methods in Physics Research Section A: Accelerators, Spectrometers, Detectors and Associated Equipment*, 458(1-2):140–147, 2001.

[31] Hong Du, Larry E Antonuk, Youcef El-Mohri, Qihua Zhao, Zhong Su, Jin Yamamoto, and Yi Wang. Investigation of the signal behavior at diagnostic energies of prototype, direct detection, active matrix, flat-panel imagers incorporating polycrystalline hgi2. *Physics in Medicine & Biology*, 53(5):1325, 2008.

[32] RA Street, SE Ready, K Van Schuylenbergh, J Ho, JB Boyce, P Nylen, K Shah, L Melekhov, and H Hermon. Comparison of pbi 2 and hgi 2 for direct detection active matrix x-ray image sensors. *Journal of Applied Physics*, 91(5):3345–3355, 2002.

[33] M Schieber, H Hermon, A Zuck, A Vilensky, L Melekhov, R Shatunovsky, E Meerson, Y Saado, M Lukach, E Pinkhasy, et al. Thick films of x-ray polycrystalline mercuric iodide detectors. *Journal of Crystal Growth*, 225(2-4):118–123, 2001.

[34] Safa Kasap, Joel B Frey, George Belev, Olivier Tousignant, Habib Mani, Jonathan Greenspan, Luc Laperriere, Oleksandr Bubon, Alla Reznik, Giovanni DeCrescenzo, et al. Amorphous and polycrystalline photoconductors for direct conversion flat panel x-ray image sensors. *Sensors*, 11:5112–5157, 2011.

[35] AH Goldan and W Zhao. A field-shaping multi-well avalanche detector for direct conversion amorphous selenium. *Medical physics*, 40(1):010702, 2013.

[36] Amir H Goldan, John A Rowlands, Ming Lu, and Wei Zhao. Nanopattern multi-well avalanche selenium detector with picosecond time resolution. In *2014 IEEE Nuclear Science Symposium and Medical Imaging Conference (NSS/MIC)*, pages 1–3. IEEE, 2014.

[37] Ahmet Camlica, Denny L Lee, and Karim S Karim. Increased temporal resolution of amorphous selenium detector using preferential charge sensing approach. In *Medical Imaging 2018: Physics of Medical Imaging*, volume 10573, pages 1509–1518. SPIE, 2018.

[38] R. N. Cahn, B. Cederström, M. Danielsson, A. Hall, M. Lundqvist, and D. Nygren. Detective quantum efficiency dependence on x-ray energy weighting in mammography. *Medical Physics*, 26(12):2680–2683, 1999.

[39] N.F. Mott. Electrons in disordered structures. *Advances in Physics*, 16(61):49–144, 1967.

[40] M. H. Cohen, H. Fritzsche, and S. R. Ovshinsky. Simple band model for amorphous semiconducting alloys. *Phys. Rev. Lett.*, 22:1065–1068, May 1969.

[41] J. M. Marshall and A. E. Owen. Drift mobility studies in vitreous arsenic triselenide. *The Philosophical Magazine: A Journal of Theoretical Experimental and Applied Physics*, 24(192):1281–1305, 1971.

[42] M. Abkowitz. Density of states in a-se from combined analysis of xerographic potentials and transient transport data. *Philosophical Magazine Letters*, 58(1):53–57, 1988.

[43] Karim S Karim, Arokia Nathan, and John Alan Rowlands. Amorphous silicon active pixel sensor readout circuit for digital imaging. *IEEE transactions on electron devices*, 50(1):200–208, 2003.

[44] CD Arvanitis, SE Bohndiek, G Royle, A Blue, HX Liang, A Clark, M Prydderch, R Turchetta, and R Speller. Empirical electro-optical and x-ray performance evaluation of cmos active pixels sensor for low dose, high resolution x-ray medical imaging. *Medical Physics*, 34(12):4612–4625, 2007.

[45] RN Cahn, B Cederström, Mats Danielsson, A Hall, M Lundqvist, and D Nygren. Detective quantum efficiency dependence on x-ray energy weighting in mammography. *Medical Physics*, 26(12):2680–2683, 1999.

[46] H Krüger, J Fink, E Kraft, N Wermes, P Fischer, I Peric, C Herrmann, M Overdick, and W Rütten. Cix: a detector for spectrally enhanced x-ray imaging by simultaneous counting and integrating. In *Medical Imaging 2008: Physics of Medical Imaging*, volume 6913, pages 245–256. SPIE, 2008.

[47] George Belev and Safa O Kasap. Amorphous selenium as an x-ray photoconductor. *Journal of non-crystalline solids*, 345:484–488, 2004.

[48] G. Belev and S. O. Kasap. Reduction of the dark current in stabilized a-Se based X-ray detectors. *Journal of Non-Crystalline Solids*, 352(9-20 SPEC. ISS.):1616–1620, 2006.

[49] S. Abbaszadeh, N. Allec, S. Ghanbarzadeh, U. Shafique, and K. S. Karim. Investigation of hole-blocking contacts for high-conversion-gain amorphous selenium detectors for x-ray imaging. *IEEE Transactions on Electron Devices*, 59(9):2403–2409, Sept 2012.

[50] Bo Zhao and Wei Zhao. Temporal performance of amorphous selenium mammography detectors. *Medical physics*, 32(1):128–136, 2005.

[51] Noor Mail, Peter O'Brien, and Geordi Pang. Lag correction model and ghosting analysis for an indirect-conversion flat-panel imager. *Journal of applied clinical medical physics*, 8(3):137–146, 2007.

[52] Tali Sharir, Simona Ben-Haim, Konstantine Merzon, Vitali Prochorov, Dalia Dickman, Shlomo Ben-Haim, and Daniel S. Berman. High-Speed Myocardial Perfusion Imaging. Initial Clinical Comparison With Conventional Dual Detector Anger Camera Imaging. *JACC: Cardiovascular Imaging*, 1(2):156–163, 2008.

[53] Zhenlei Lyu, Shi Wang, Haipeng Wang, Hui Liu, Li Cheng, Zhaoxia Wu, Zuoxiang He, Yaqiang Liu, and Tianyu Ma. Design and Initial Performance Evaluation of a Large-Animal Dynamic SPECT/CT Imaging System. *2018 IEEE Nuclear Science Symposium and Medical Imaging Conference, NSS/MIC 2018 - Proceedings*, pages 1–3, 2018.

[54] Piotr J. Slomka, Tinsu Pan, Daniel S. Berman, and Guido Germano. Advances in SPECT and PET Hardware. *Progress in Cardiovascular Diseases*, 57(6):566–578, 2015.

[55] Sahar Adnani, Abdollah Pil-Ali, Christopher C. Scott, and Karim S. Karim. Monte Carlo simulation of an amorphous selenium-based multi-layer photon-counting detector for SPECT applications. 1159515(May):39, 2021.

[56] Shiva Abbaszadeh, Christopher C. Scott, Oleksandr Bubon, Alla Reznik, and Karim S. Karim. Enhanced Detection Efficiency of Direct Conversion X-ray Detector Using Polyimide as Hole-Blocking Layer. *Scientific Reports*, 3(1):3360, 2013.

[57] Karl Stierstorfer, Martin Hupfer, and Niko Köster. Erratum: Modeling the DQE(f) of photon-counting detectors: impact of the pixel sensitivity profile (2019 Phys. Med. Biol . 64 105008) . *Physics in Medicine & Biology*, 64(12):129601, 2019.

[58] Christopher C. Scott, Shiva Abbaszadeh, Sina Ghanbarzadeh, Gary Allan, Michael Farrier, Ian A. Cunningham, and Karim S. Karim. Amorphous selenium direct detection CMOS digital x-ray imager with 25 micron pixel pitch. *Medical Imaging 2014: Physics of Medical Imaging*, 9033(March 2014):90331G, 2014.

[59] Scott Dow, Adrian Howansky, Anthony R. Lubinsky, and Wei Zhao. Evaluation of a hybrid direct–indirect active matrix flat-panel imager using Monte Carlo simulation. *Journal of Medical Imaging*, 7(03):1, 2020.

[60] J. M. Boone. Determination of the presampled MTF in computed tomography. *Medical Physics*, 28(3):356–360, 2001.

[61] T. Michel, G. Anton, M. Böhnel, J. Durst, M. Firsching, A. Korn, B. Kreisler, A. Loehr, F. Nachtrab, D. Niederlöhner, F. Sukowski, and P. Takoukam Talla. A fundamental method to determine the signal-to-noise ratio (snr) and detective quantum efficiency (dqe) for a photon counting pixel detector. *Nuclear Instruments and Methods in Physics Research Section A: Accelerators, Spectrometers, Detectors and Associated Equipment*, 568(2):799–802, 2006.

[62] Y. Yin, S. Komarov, H. Wu, T. Y. Song, Q. Li, A. Garson, K. Lee, G. Simburger, P. Dowkontt, H. Krawczynski, and Yuan Ch. Tai. Characterization of highly pixelated CZT detectors for sub-millimeter PET imaging. *IEEE Nuclear Science Symposium Conference Record*, pages 2411–2414, 2009.

[63] S. Abbaszadeh, G. Chinn, and C. S. Levin. Positioning true coincidences that undergo inter-and intra-crystal scatter for a sub-mm resolution cadmium zinc telluride-based PET system. *Physics in Medicine and Biology*, 63(2), 2018.

[64] D. Vernekohl, S. Abbaszadeh, Y. Gu, and C. S. Levin. Robust Detector Calibration for a Novel PET System Based on Cross-Strip CZT Detectors. *IEEE Transactions on Radiation and Plasma Medical Sciences*, 7311(c):1–1, 2018.

[65] L. S. Barabash, E Belcarz, Yu B Gurov, E I Maltsev, L P Meszaros, Yu P Petukhov, A G Pimenov, and V G Sandukovsky. Semiconductor microstrip detector with a resistive layer, March 1990.

[66] Rodrigo Martins, Guilherme Lavareda, Elvira Fortunato, Fernando Soares, Luis Fernandes, and Luis Alberto Almeida Ferreira. Linear thin-film position-sensitive detector (LTFPSD) for 3D measurements. In Morley M. Blouke, editor, *Charge-Coupled Devices and Solid State Optical Sensors V*, volume 2415, pages 148 – 158. International Society for Optics and Photonics, SPIE, 1995.

[67] Rodrigo Martins and Elvira Fortunato. *Thin Film Position Sensitive Detectors: From 1D to 3D Applications*, pages 342–403. Springer Berlin Heidelberg, Germany, 2000.

[68] V. Radeka. Signal, noise and resolution in position-sensitive detectors. *IEEE Transactions on Nuclear Science*, 21(1):51–64, 1974.

[69] D. Bassignana, M. Fernandez, R. Jaramillo, M. Lozano, F. J. Munoz, G. Pellegrini, D. Quirion, and I. Vila. First investigation of a novel 2D position-sensitive semiconductor detector concept. *Journal of Instrumentation*, 7(2), 2012.

[70] Sahar Adnani, Abdollah Pil-Ali, Celal Con, and Karim S. Karim. A Position-Sensitive Microstrip Detector using Amorphous Selenium Photoconductor. In *2021 IEEE Nuclear Science Symposium and Medical Imaging Conference (NSS/MIC)*, pages 1–3, October 2021. ISSN: 2577-0829.

[71] Sahar Adnani, Abdollah Pil-Ali, Celal Con, and Karim S. Karim. Investigation of position linearity in position-sensitive microstrip amorphous selenium-based detector. In Wei Zhao and Lifeng Yu, editors, *Medical Imaging 2022: Physics of Medical Imaging*, volume 12031, page 120310M. International Society for Optics and Photonics, SPIE, 2022.

[72] Sahar Adnani, Abdollah Pil-Ali, and Karim S. Karim. A low-temperature processed organic hole-blocking contact layer for amorphous selenium x-ray photoconductor. *IEEE Electron Device Letters*, 44(9):1528–1530, 2023.

[73] Ioannis Sechopoulos. A review of breast tomosynthesis. part i. the image acquisition process. *Medical Physics*, 40(1):014301, 2013.

[74] SA Mahmood, MZ Kabir, O Tousignant, H Mani, J Greenspan, and P Botka. Dark current in multilayer amorphous selenium x-ray imaging detectors. *Applied Physics Letters*, 92(22), 2008.

[75] Joel B. Frey, George Belev, Olivier Tousignant, Habib Mani, Luc Laperriere, and Safa O. Kasap. Dark current in multilayer stabilized amorphous selenium based photoconductive x-ray detectors. *Journal of Applied Physics*, 112(1):014502, 07 2012.

[76] Shiva Abbaszadeh, Nicholas Allec, Sina Ghanbarzadeh, Umar Shafique, and Karim S. Karim. Investigation of hole-blocking contacts for high-conversion-gain amorphous selenium detectors for x-ray imaging. *IEEE Transactions on Electron Devices*, 59(9):2403–2409, 2012.

[77] Haripriya Kannan, Jann Stavro, Atreyo Mukherjee, Sébastien Léveillé, Kim Kisslinger, Lizhu Guan, Wei Zhao, Ayaskanta Sahu, and Amir H. Goldan. Ultralow dark currents in avalanche amorphous selenium photodetectors using solution-processed quantum dot blocking layer. *ACS Photonics*, 7(6):1367–1374, 2020.

[78] Kenji Kikuchi, Yuji Ohkawa, Kazunori Miyakawa, Tomoki Matsubara, Kenkichi Tanioka, Misao Kubota, and Norifumi Egami. Hole-blocking mechanism in high-gain avalanche rushing amorphous photoconductor (harp) film. *physica status solidi c*, 8(9):2800–2803, 2011.

[79] Christina Pang, Vijila Chellappan, Jong Hyuk Yim, Mein Jin Tan, Glen Tai Wei Goh, Soonil Lee, Jie Zhang, and John de Mello. Enhanced performance using an su-8 dielectric interlayer in a bulk heterojunction organic solar cell. *ACS Applied Materials & Interfaces*, 7(9):5219–5225, 2015. PMID: 25658649.

[80] Antonio Sarno, Giovanni Mettivier, and Paolo Russo. Dedicated breast computed tomography: Basic aspects. *Medical Physics*, 42(6Part1):2786–2804, 2015.

[81] Oleksandr Grynko, Tristen Thibault, Emma Pineau, and Alla Reznik. Engineering of a blocking layer structure for low-lag operation of the a-pbo-based x-ray detector. *IEEE Transactions on Electron Devices*, 68(5):2335–2341, 2021.

[82] S O Kasap and C Juhasz. Time-of-flight drift mobility measurements on chlorine-doped amorphous selenium films. *Journal of Physics D: Applied Physics*, 18(4):703, apr 1985.

[83] Harvey Scher and Elliott W. Montroll. Anomalous transit-time dispersion in amorphous solids. *Phys. Rev. B*, 12:2455–2477, Sep 1975.

[84] G Pfister. Hopping transport in a molecularly doped organic polymer. *Physical Review B*, 16(8):3676, 1977.

[85] Kaitlin Hellier, Akyl Swaby, Jennifer Ott, and Shiva Abbaszadeh. Performance evaluation of an amorphous selenium photodetector at high fields for application integration. *IEEE Sensors Journal*, 2023.

[86] K. Yang, Q. Cui, Y. Hou, B. Liu, Q. Zhou, J. Hu, H. K. Mao, and G. Zou. Pressure-induced crystallization and phase transformation of amorphous selenium: Raman spectroscopy and x-ray diffraction studies. *Journal of Physics Condensed Matter*, 19(42), 2007.

[87] S. Imura, K. Kikuchi, K. Miyakawa, H. Ohtake, M. Kubota, T. Okino, Y. Hirose, Y. Kato, and N. Teranishi. High-sensitivity image sensors overlaid with thin-film gallium oxide/crystalline selenium heterojunction photodiodes. *IEEE Transactions on Electron Devices*, 63(1):86–91, 2016.

[88] S. Imura, K. Kikuchi, K. Miyakawa, and M. Kubota. Optical properties of photoconductor using crystalline selenium. *Canadian Journal of Physics*, 92(7/8):645–647, 2014.

[89] S. Imura, K. Kikuchi, K. Miyakawa, H. Ohtake, M. Kubota, T. Okino, Y. Hirose, Y. Kato, and N. Teranishi. Stacked image sensor using chlorine-doped crystalline selenium photoconversion layer composed of size-controlled polycrystalline particles. *Technical Digest - International Electron Devices Meeting, IEDM*, 2016-February:30.7.1–30.7.4, 2015.

[90] S. Imura, K. Kikuchi, K. Miyakawa, H. Ohtake, M. Kubota, T. Nakada, T. Okino, Y. Hirose, Y. Kato, and N. Teranishi. High sensitivity image sensor overlaid with thin-film crystalline-selenium-based heterojunction photodiode. *Technical Digest - International Electron Devices Meeting, IEDM*, 2015-February(February):4.3.1–4.3.4, 2015.

[91] S. Imura, K. Kikuchi, K. Miyakawa, H. Ohtake, and M. Kubota. Low-voltage-operation avalanche photodiode based on n-gallium oxide/p-crystalline selenium heterojunction. *Applied Physics Letters*, 104(24):1–5, 2014.

[92] S. Imura, K. Mineo, K. Miyakawa, M. Namba, H. Ohtake, and M. Kubota. High-efficiency and low dark current crystalline selenium-based heterojunction photodiode with a high-quality tellurium nucleation layer. *Proceedings of IEEE Sensors*, 2017-December:1–3, 2017.

[93] Emilio Gatti and Pavel Rehak. Semiconductor drift chamber — An application of a novel charge transport scheme. *Nuclear Instruments and Methods in Physics Research*, 225(3):608–614, September 1984.

[94] Pavel Rehak, Jack Walton, Emillo Gatti, Antonio Longoni, Marco Sanpietro, Josef Kemmer, Hans Dietl, Peter Holl, Robert Klanner, Gerhard Lutz, Andrew Wylie, and Hubert Becker. Progress in semiconductor drift detectors. *Nuclear Instruments and Methods in Physics Research Section A: Accelerators, Spectrometers, Detectors and Associated Equipment*, 248(2):367–378, August 1986.

[95] E.A. Hijzen, E.M. Schooneveld, C.W.E. van Eijk, R.W. Hollander, P.M. Sarro, and A. van den Bogaard. A novel silicon drift detector with two dimensional drift time measurement. *Nuclear Instruments and Methods in Physics Research Section A: Accelerators, Spectrometers, Detectors and Associated Equipment*, 348(2-3):470–474, September 1994.

[96] M. A. J. van Pamelen and C. Budtz-Jørgensen. CdZnTe drift detector with correction for hole trapping. *Nuclear Instruments and Methods in Physics Research Section A: Accelerators, Spectrometers, Detectors and Associated Equipment*, 411(1):197–200, July 1998.

[97] I. Kuvvetli, C. Budtz-Jørgensen, E. Caroli, and N. Auricchio. CZT drift strip detectors for high energy astrophysics. *Nuclear Instruments and Methods in Physics Research Section A: Accelerators, Spectrometers, Detectors and Associated Equipment*, 624(2):486–491, December 2010.

[98] Ahmet Camlica, Denny Lee, Hyunsuk Jang, Salman M. Arnab, Yuan Fang, M. Z. Kabir, and Karim S. Karim. Performance of amorphous selenium-based unipolar charge sensing detector for photon counting x-ray imaging. In *Medical Imaging 2020: Physics of Medical Imaging*, volume 11312, pages 107–114. SPIE, March 2020.

[99] Andy LaBella, Jann Stavro, Sebastien Léveillé, Wei Zhao, and Amir H. Goldan. Picosecond Time Resolution with Avalanche Amorphous Selenium. *ACS Photonics*, 6(6):1338–1344, June 2019.